# First Principles Studies of Materials for Energy Applications

A Thesis

Submitted to the
Jawaharlal Nehru Centre for Advanced Scientific Research, Bengaluru
for the Degree of DOCTOR OF PHILOSOPHY

by

**Debdipto Acharya**

JAWAHARLAL NEHRU CENTRE FOR ADVANCED SCIENTIFIC RESEARCH, BENGALURU,INDIA.

JUNE 2020

*To My Family*

# DECLARATION

I hereby declare that the matter embodied in the thesis entitled "**First Principles Studies of Materials for Energy Applications**" is the result of investigations carried out by me at the Theoretical Science Unit, Jawaharlal Nehru Centre for Advanced Scientific Research, Bangalore, India under the supervision of Prof. Shobhana Narasimhan and that it has not been submitted elsewhere for the award of any degree or diploma.

In keeping with the general practice in reporting scientific observations, due acknowledgement has been made whenever the work described is based on the findings of other investigators. Any omission that might have occurred by oversight or error of judgement is regretted.

Debdipto Acharya

# CERTIFICATE

I hereby certify that the matter embodied in this thesis entitled "**First Principles Studies of Materials for Energy Applications**" has been carried out by Mr. Debdipto Acharya at the Theoretical Science Unit, Jawaharlal Nehru Centre for Advanced Scientific Research, Bangalore, India under my supervision and that it has not been submitted elsewhere for the award of any degree or diploma.

Prof. Shobhana Narasimhan
(Research Supervisor)

# Acknowledgements

First and foremost, I would like to thank my Ph.D. supervisor Prof. Shobhana Narasimhan for her guidance, inspiration and encouragement throughout my Ph.D. tenure. She helped me in understanding the basics and analyzing the results obtained. It would have been impossible for me to complete my projects and thesis without her constant support, guidance and motivation. She gave me chances to travel to other countries to attend important conferences. Her collaborations made it possible for me to learn different techniques that I have employed in my research work. She was there whenever I needed valuable guidance from her. Most importantly, she created a wonderful research atmosphere in the lab which propelled the research work during my Ph.D.

I would like to thank my experimental and theoretical collaborators: Prof. Ranjani Viswanatha, Prof. Ganapathy Ayappa, Prof. Ashok Ganguli, Prof. Brandon C. Wood, Pradeep, Rajasekaran, Saptarshi, Kasinath, Kanchan, Nisha, Somesh and Saikat.

I thank my course instructors Prof. U. V. Waghmare, Prof. Subir K. Das, Prof. Swapan K. Pati, and Prof. Balasubramanian. I want to thank all the faculty members from TSU. I want to acknowledge the present and past chair persons of TSU. I am thankful to Dr. Ari. P. Seitsonen, Prof. M. Weinert, Prof. T. Saha. Dasgupta, Prof. U. V. Waghmare for the useful scientific discussions I had with them, at different times during the course of my Ph.D.

I acknowledge the financial help from the TUE-CMS and JNCASR for supporting my research.

I thank everyone in the Academic Section, especially Dr. Princy and Sukanya ma'am. I would like to thank Mr. Jayachandra, Ms. Jayamangala, Mr. Joydeep Deb, and all others in the Administrative Section for their help with all the administrative procedures. I thank Dr. Archana and all the Dhanvantari staff for the medical assistance they provided. I am thankful to the CCMS staff Vijay, Anand, Anoop, and Suresh for their help and support with computing facilities. I want to thank all the library staff and the hostel staff.

I thank all my past and present labmates: Mighfar, Madhura, Nisha, Kanchan, Sananda, Vasudevan, Bulumoni, Debarati, Rajdeep, Sukanya, Rajiv, Devina, Somesh, Saikat, Sourav, Nandana, Arpan, and Abhishek for providing a lively and pleasant environment in the lab. I want to thank Sourav, Devina, Brandon and Nisha, especially for helping me in thesis writing.

I thank my past and present colleagues, especially Dibyajyoti, Koushik, Arkamita, Shubhajit, Soumalya, Pawan, Sudeep and Monoj, for the wonderful time we had together which made the time I spent in JNCASR, more enjoyable.

My respectful gratitude to Prof. C. N. R. Rao for providing excellent research facilities and scientific environment in the institute.

Finally, I thank my parents and my sister for their love, constant support, and motivation, which made it possible to finish my Ph.D.

# Synopsis

In this thesis, I have designed materials computationally, tuning their electronic, structural, dynamical and adsorption properties with specific applications in mind. The techniques I have used are *ab-initio* density functional theory and *ab-initio* molecular dynamics.

In Chapter 1, I provide a brief introduction to the problems studied. I have followed the approach of 'rational design' of materials, to tune their properties for energy applications. I have exploited and tuned the polar discontinuity at interfaces between two materials to increase the adsorption strength of polar molecules; this could have applications in thermal energy storage (Chapter 3). I have tried to understand the structural and dynamical properties of electrolyte material to make it suitable for use in fuel cells (Chapter 4). I have used doping to tune the adsorption strength of hydrogen in a family of materials, so as to tailor them for enhanced hydrogen production (Chapter 5). In Chapter 6 and Chapter 7, I have tuned the electronic property of perovskite materials by doping for enhanced energy efficient photoluminescence. Except for Chapter 3 and Chapter 4, all the works presented in thesis have been in collaboration with experimental groups, and have been motivated by their experimental results. While it can be seen that the systems and phenomena studied in this thesis are diverse, the above projects have in common a research philosophy motivated by the rational design of materials for energy applications.

In Chapter 2, I discuss the computational techniques and theoretical formalism used in the thesis: *ab-initio* density functional theory used for Chapters 3-7, the DFT-D2 technique to include dispersion interactions used in Chapters 3, 4 and 7, 'fully relativistic' calculations to include spin-orbit interactions used in Chapter 6 and 7, density functional perturbation theory (DFPT) used to calculate zero-point energy in Chapter 5 and phonon spectra in Chapter 7, and Car-Parrinello molecular dynamics used to study structural and dynamical properties in Chapter 4.

In Chapter 3, I study the adsorption of methanol on graphene, boron nitride, striped armchair interfaces and striped zigzag interfaces, mixed BCN and triangular graphene islands in a boron-nitride matrix. I have shown that although the striped zigzag interface is most energetically configuration, the formation of small C triangular island inside a BN matrix is also quite energetically favored. Such triangular islands have a large charge localized along their perimeter, resulting in a high adsorption energy for polar molecules such as methanol. An enhanced adsorption energy of 65% for methanol, compared to adsorption over graphene, is achieved on triangular islands. One can interpret these results in terms of various kinds of van der Waals interactions, and show that this increase in binding does indeed arise primarily from an increase in Keesom interactions between the permanent dipole on methanol and the permanent charges present along the C-BN interfaces.

In Chapter 4, I study the energetics, structural and dynamical property of water on a graphene oxide substrate. This study is motivated by the suggestion that graphene oxide can be used in proton exchange membrane fuel cells, and the experimental observation that the proton conductivity increases significantly as the water content (relative humidity) is increased. I have looked at the binding and static geometries of water on graphene oxide using density functional theory calculations, and the time-averaged structural and dynamical properties of this system by using ab initio molecular dynamics. I use a model of graphene oxide consisting of domains of functionalized graphene (periodic graphene oxide) that form interfaces with domains of bare graphene. Starting geometries are obtained from the results of classical molecular dynamics simulations, where it is found that water bridges are formed, that connect two hydrophilic regions on the surface by spanning a hydrophobic bare graphene area. I find that as the coverage of water molecules on graphene oxide increases, the average coordination number and average number of hydrogen bonds per water molecule increases. Also with increasing content of water, the diffusion coefficient of the water molecule increases and the oriental relaxation time decreases.

In Chapter 5, I study the enhanced HER activity on $Mo_2C$-$Mo_2N$ composite systems. Our experimental collaborators have shown this composite system shows higher HER activity than bare $Mo_2C$ and $Mo_2N$. I have calculated free energy diagram to explain why the doped system shows better activity than the undoped systems and my calculation also explains the experimental fact that N-rich doped sample shows better activity than the C-rich sample. I also obtain the interesting result that the incorporation of van der Waals interaction is essential to explain the structural stability of $Mo_2C$ and $Mo_2N$ in their orthorhombic and tetragonal form.

In Chapter 6, I investigate the origin of the unusual band-gap change in Sn-doped perovskite nanocrystals: with Sn doping, the band gap in nanocrystals increases, whereas in bulk materials it decreases. I have determined that the effect of Sn doping is primarily a change in the lattice parameter of the system. I find that the effect of van der Waals interactions and spin-orbit coupling are extremely important to understand the observed trends in band gap. Effect of strain changes the valence band and effect of spin-orbit changes the conduction band. This two phenomena together can explain the unusual band-gap changes in Sn doped perovskite nanocrystals.

In Chapter 7, I investigate the reason for delayed emission in Mn doped perovskite nanocrystals which have been observed by our experimental collaborators. I find that the spin-orbit coupling effect is important for the system studied (Mn-doped $CsPbBr_3$), being responsible for moving the conduction band edge down, as a result of which the Mn levels lie buried deep within the conduction band. I have shown that Mn atoms have a significant amount of vibrational and electronic coupling with Pb atoms. This vibrational coupling and electron-phonon coupling is the reason of delayed fluoroscence observed for Mn doped perovskite samples.

In Chapter 8, the conclusions of each chapter are summarized and possible directions for future work are discussed.

# List of Publications

1. "Harvesting Delayed Fluroscence in Perovskite Nanocrystals using Spin Forbidden Mn d states", Pradeep K. R, Debdipto Acharya, Priyanka Jain, Kushagra Gahlot, Anur Yadav, Andrea Camelini, Margherita Zavelani-Rossi, Giulio Cerullo, Chandrabhas Narayan, Shobhana Narasimhan and Ranjani Viswanatha, under revision in ACS Energy Letters.

2. "Leveraging Polar Discontinuities at Interfaces For Enhanced Binding of Adsorbates: Methanol on C-BN and BCN", Debdipto Acharya, Kanchan Ulman and Shobhana Narasimhan (preprint available)

3. "Structural and dynamical properties of $H_2O$ on Graphene Oxide", Debdipto Acharya, Rajasekaran M, Shobhana Narasimhan and K. Ganapathy Ayappa (manuscript under preparation)

4. "Origins of anomalous band gap change in Sn doped $CsPbBr_3$ nanocrystals", Debdipto Acharya, Pradeep K. R, Shobhana Narasimhan and Ranjani Viswanatha (manuscript under preparation)

5. "Enhanced hydrogen evolution reactivity on $Mo_2C$-$Mo_2N$ composites", Kasinath Ojha, Debdipto Acharya, Nisha Menon, Sourav Mondal, Shobhana Narasimhan, Preeti Dagar and Ashok K Ganguli (manuscript under preparation)

# List of Symbols and Abbreviations

| | |
|---|---|
| $\mathbf{P}$ | Bulk Polarization |
| $\mathbf{n}$ | Normal vector |
| $\epsilon_d$ | $d$-band center |
| $\lambda_{\text{bound}}$ | Bound charge density |
| $\lambda_{\text{free}}$ | Free charge density |
| $\rho$ | Charge density |
| $\tau$ | Dipole orientational relaxation time |
| $C^{\alpha}$ | Dipole orientational correlation function |
| $D$ | Diffusion coefficient |
| $E_D$ | Debye contribution to adsorption energy |
| $E_f$ | Fermi Energy |
| $E_g$ | Band Gap |
| $E_K$ | Keesom contribution to adsorption energy |
| $E_L$ | London contribution to adsorption energy |

| | |
|---|---|
| $E_{\mathrm{ads}}$ | Adsorption Energy |
| $G$ | Gibbs Free Energy |
| $g(r)$ | Radial distribution function |
| $g_d(\epsilon)$ | $d$-band density of states |
| $P$ | Pressure |
| $Q$ | Charge |
| $S$ | Entropy |
| $V$ | Volume |
| $\mu^{\overrightarrow{\mathrm{perm}}}$ | Permanent dipole moment of methanol molecule |
| 1D | One-dimensional |
| 2D | Two-dimensional |
| 3D | Three-dimensional |
| AIMD | *ab initio* Molecular Dynamics |
| BFGS | Broyden-Fletcher-Goldfarb-Shanno |
| BLYP | Becke-Lee-Yang-Parr |
| BOMD | Born-Oppenheimer Molecular Dynamics |
| BZ | Brillouin Zone |
| CBM | Conduction Band Minimum |
| CPMD | Car-Parrinello Molecular Dynamics |
| DFPT | Density Functional Perturbation Theory |

| | |
|---|---|
| DFT | Density Functional Theory |
| GGA | Generalized Gradient Approximation |
| GGA | Local Density Approximation |
| HER | Hydrogen Evolution Reaction |
| KS | Kohn Sham |
| LED | Light Emitting Diode |
| MSD | Mean Square Displacement |
| NBO | Natural Bond Orbital |
| OER | Oxygen Evolution Reaction |
| PBE | Perdew, Burke and Ernzerhof |
| PDOS | Projected Density of States |
| PEM | Proton Exchange Membrane |
| PGO | Periodic Graphene Oxide |
| PLQY | Photoluminescence Quantum Yield |
| QD | Quantum Dots |
| SOC | Spin-Orbit Coupling |
| STM | Scanning Tunneling Microscopy |
| STS | Scanning Tunneling Spectroscopy |
| TADF | Thermally Assisted Delayed Fluorescence |
| TEM | Transmission Electron Microscopy |

| | |
|---|---|
| VADF | Vibrationally Assisted Delayed Fluorescence |
| VBM | Valence Band Maximum |
| XRD | X-ray diffraction |
| ZGO | Zigzag Graphene Oxide |
| ZPE | Zero Point Energy |

# Contents

**Acknowledgements** **v**

**Synopsis** **vii**

**List of Publications** **xi**

**List of Symbols and Abbreviations** **xiii**

**1 Introduction** **3**

1.1 **Rational Design of Materials for Energy Applications** . . . . . . . . 3

**2 Methods and Formalism** **15**

2.1 **The Many-Body Problem** . . . . . . . . . . . . . . . . . . . . . . . . 15

2.1.1 Born-Oppenheimer or Adiabatic Approximation . . . . . . . . . 16

2.1.2 Density Functional Theory . . . . . . . . . . . . . . . . . . . . . 17

2.1.3 Exchange-correlation Functionals . . . . . . . . . . . . . . . . . 23

2.1.4 Basis Sets . . . . . . . . . . . . . . . . . . . . . . . . . . . . . . 24

2.1.5 Pseudopotential Approximation . . . . . . . . . . . . . . . . . . 25

2.1.6 k-point Sampling and Smearing . . . . . . . . . . . . . . . . . . 26

2.1.7 Dispersion Interactions: The DFT-D2 Method . . . . . . . . . . . 27

2.1.8 Spin-Polarized Density Functional Theory . . . . . . . . . . . . 28

2.2 **Calculation of Forces and Stresses** . . . . . . . . . . . . . . . . . . 29

2.3 **Wannier Functions and Model Hamiltonians** . . . . . . . . . . . . . 30
2.3.1 Projection method . . . . . . . . . . . . . . . . . . . . . . . . 31
2.3.2 Maximally localized Wannier functions . . . . . . . . . . . . . . . 32
2.4 **Phonon Calculations: Density Functional Perturbation Theory** . . 32
2.4.1 Lattice Dynamics from Electronic-Structure Theory . . . . . . . . 33
2.4.2 Linear Response . . . . . . . . . . . . . . . . . . . . . . . . . 34
2.5 **Electron-phonon coupling** . . . . . . . . . . . . . . . . . . . . 35
2.6 **First principles molecular dynamics** . . . . . . . . . . . . . . . 36
2.6.1 Verlet algorithm and Velocity Verlet algorithm . . . . . . . . . . 36
2.6.2 Born-Oppenheimer molecular dynamics . . . . . . . . . . . . . . 38
2.6.3 Car-Parrinello molecular dynamics . . . . . . . . . . . . . . . . 38

**3 Tuning the Binding of Methanol on C-BN and BCN Systems 45**
3.1 **Introduction** . . . . . . . . . . . . . . . . . . . . . . . . . . . 45
3.2 **Systems under study** . . . . . . . . . . . . . . . . . . . . . . . 49
3.3 **Computational Details** . . . . . . . . . . . . . . . . . . . . . . 51
3.4 **Results** . . . . . . . . . . . . . . . . . . . . . . . . . . . . . 52
3.4.1 Benchmarks . . . . . . . . . . . . . . . . . . . . . . . . . . . 52
3.4.2 Interface formation energies . . . . . . . . . . . . . . . . . . . 53
3.4.3 Polar Discontinuity and Lines of Charge . . . . . . . . . . . . . 56
3.4.4 Adsorption of Methanol . . . . . . . . . . . . . . . . . . . . . 60
3.5 **Analysis and Discussion** . . . . . . . . . . . . . . . . . . . . . 63
3.6 **Conclusions** . . . . . . . . . . . . . . . . . . . . . . . . . . . 70

**4 Structural and Dynamical Properties of $H_2O$ on Graphene Oxide 77**
4.1 **Introduction** . . . . . . . . . . . . . . . . . . . . . . . . . . . 77
4.2 **Systems under study** . . . . . . . . . . . . . . . . . . . . . . . 80
4.3 **Computational Details** . . . . . . . . . . . . . . . . . . . . . . 81
4.4 **Results** . . . . . . . . . . . . . . . . . . . . . . . . . . . . . 83

4.4.1 Energetics of water on graphene and graphene oxide: statics . . 83
4.4.2 Hydrophobic and hydrophilic properties of graphene and graphene oxide substrates . . . . . . . . . . . . . . . . . . . . . . . . . 86
4.4.3 Structural and dynamical properties of water on graphene oxide 87
4.5 **Conclusions** . . . . . . . . . . . . . . . . . . . . . . . . . . . . 99

**5 Enhanced hydrogen evolution reactivity on $Mo_2C$-$Mo_2N$ composites 105**
5.1 **Introduction** . . . . . . . . . . . . . . . . . . . . . . . . . . . . 105
5.2 **Experimental background** . . . . . . . . . . . . . . . . . . . . 108
5.3 **Systems under study** . . . . . . . . . . . . . . . . . . . . . . . 108
5.4 **Computational Details** . . . . . . . . . . . . . . . . . . . . . . 110
5.5 **Results** . . . . . . . . . . . . . . . . . . . . . . . . . . . . . . . 112
5.5.1 Structure and energetics of pristine bulk $Mo_2C$ and $Mo_2N$ . . . . 112
5.5.2 Structure and energetics of bulk $Mo_2C_{1-x}N_x$ systems . . . . . . . 113
5.5.3 Structural stability of different $Mo_2C$ and $Mo_2N$ surfaces . . . . . 115
5.5.4 Adsorption of H on $Mo_2C_{1-x}N_x$ surfaces . . . . . . . . . . . . . . 117
5.5.5 Combining theory and experiment: Optimum value of $x$ leads to high HER activity . . . . . . . . . . . . . . . . . . . . . . . . . . 120
5.6 **Conclusions** . . . . . . . . . . . . . . . . . . . . . . . . . . . . 122

**6 Anomalous change in band gap in Sn-doped $CsPbBr_3$ nanocrystals 131**
6.1 **Introduction** . . . . . . . . . . . . . . . . . . . . . . . . . . . . 131
6.2 **Experimental background** . . . . . . . . . . . . . . . . . . . . 133
6.3 **Computational Details** . . . . . . . . . . . . . . . . . . . . . . 134
6.4 **Results** . . . . . . . . . . . . . . . . . . . . . . . . . . . . . . . 135
6.4.1 Lattice parameter and band-gap of cubic $CsPbBr_3$ . . . . . . . . . 135
6.4.2 Band-gap change with lattice parameter of cubic $CsPbBr_3$ . . . . 136
6.4.3 Movement of valence and conduction band with lattice parameter 137

6.4.4 Why the SOC band-gap changes non-monotonically with lattice parameter . . . . . . 138
6.4.5 Sn-doping of $CsPbBr_3$ . . . . . . 141
6.5 **Conclusions** . . . . . . 143

**7 Insights from DFT into delayed emission in Mn-doped perovskite nanocrystals 151**

7.1 **Introduction** . . . . . . 151
7.2 **Experimental Results** . . . . . . 152
7.3 **Systems under study** . . . . . . 154
7.4 **Computational Details** . . . . . . 155
7.5 **Results and Discussion** . . . . . . 155
7.5.1 Lattice parameter and electronic structure of $CsPbBr_3$ and $CsPbCl_3$ 155
7.5.2 Electronic structure of Mn-doped $CsPbBr_3$ . . . . . . 157
7.5.3 Shift in the position of Mn level in the conduction band upon inclusion of spin-orbit coupling . . . . . . 158
7.5.4 Comparison of vibrational coupling between Mn-doped $CsPbBr_3$ and Mn doped $CsPbCl_3$ . . . . . . 159
7.5.5 Electron-phonon coupling in Mn-doped $CsPbBr_3$ . . . . . . 161
7.6 **Conclusions** . . . . . . 162

**8 Conclusions and Outlook 167**

# List of Figures

2.1 Flow chart demonstrating the self-consistency loop used to iteratively solve the Kohn-Sham equations . . . . . . . . . . . . . . . . . . . . . . . . 22

3.1 Polar discontinuity in a two dimensional honeycomb lattice composed of two domains with two different formal polarizations $\mathbf{P}_1$ and $\mathbf{P}_2$ results in a bound charge density at the interface. The figure is taken with permission from Ref. 12 ©(2015) Elsevier. . . . . . . . . . . . . . . . . . . . . . . . . 47

3.2 Top views of types of substrates considered for methanol adsorption: (a) graphene; (b) h-BN; (c) C-BN with an armchair interface; (d) C-BN with a zigzag interface; (e) mixed BCN; (f) triangular graphene island situated within BN matrix. Color scheme for atomic spheres: C (green), B (gray), N (blue). . . . . . . . . . . . . . . . . . . . . . . . . . . . . . . . . . . 50

3.3 Formation energy $E_f$ per atom as computed from DFT calculations for BCN systems with 1:1:1 ratios for B:C:N. $n$ is the number of B, C or N atoms in the primitive unit cell; for the striped structures, as $n$ increases, the separation between domain walls increases. Results are shown for stripes with armchair interfaces (black dots), stripes with zigzag interfaces (red squares), triangular graphene island within BN matrix (blue diamonds), and a mixed BCN structure (green dashed line). Note that a phase segregated structures of graphene and h-BN are favored over the formation of the mixed BCN structure, and striped domains of graphene and BN separated by zigzag interfaces are energetically most favorable for smaller domain wall separations. . . . . . . . . . . . . . . . . . . . . . . 53

3.4 Formation energy $E_f$ per atom as computed from DFT calculations as a function of concentration of C with 1:1 ratios for B:N. Results are shown for structures where the primitive unit cell contains 60 atoms, for stripes with zigzag interfaces, triangular graphene islands within BN matrix, and three kinds of mixed BCN structures (see text for descriptions). Note that striped domains of graphene and h-BN separated by zigzag interfaces are energetically most favorable for all concentrations and the difference in formation energy between different structures increases as the percentage of C atoms increases. . . . . . . . . . . . . . . . . . . . . . . . . . 55

3.5 Top views showing atomistic structure and charge difference plots. Structure of (a) striped domains of graphene and h-BN separated by a zigzag interface; (b) triangular graphene island situated within BN matrix. Charge density difference plots between the C-BN systems and a system in which all the atoms are replaced by carbon atoms, for (c) striped domains of graphene and h-BN separated by a zigzag interface; (d) triangular graphene island situated within BN matrix. In (c) and (d), red and blue lobes correspond to a gain and loss of electronic charge respectively. Isosurfaces corresponding to $\Delta\rho = \pm 0.009$ e/(bohr)$^3$ have been plotted. Color scheme for atomic spheres: C (green), B (gray), N (blue). . . . . . . . . . . . . . . 57

3.6 Charge localization at interfaces, as calculated by the NBO method. (a) Total charge on each atom as a function of its $x$ coordinate (b) sum of charges of successive pairs of atoms, as a function of $x$, and (c) Difference between charge on each atom in the striped domain structure and the corresponding species of atom in the bulk material, as a function of $x$ The unit cell of the striped zigzag C-BN interface consists of 20 C, 10 B and 10 N atoms, as shown in the bottom of the figure. Color scheme for atomic spheres: C (green), B (gray), N (blue). . . . . . . . . . . . . . . . . 58

3.7 Difference between total charge on each atom and charge on each atom in the corresponding bulk system (i.e., no interfaces present) for (a) striped zigzag C-BN interface and (b) graphene island within BN matrix has been shown by the color gradient. The blue color denotes maximum positive charge and red color denotes maximum negative charge. The intermediate colors denote the amount of charge according to the color bar shown on the right hand side. Fig. 3.7(b) may be compared with Fig. 3.5(b) . . . 59

3.8 Top views of different stable adsorption geometries obtained for methanol on graphene and h-BN; (a)-(h) are the C1-C8 configurations for methanol on graphene and (i)-(p) are the C1-C8 configurations for methanol on BN. Color scheme for atomic spheres: C-graphene (green), C-methanol (yellow), H (black), O (red), B (gray), N (blue). . . . . . . . . . . . . . . . 61

3.9 Top views of the optimal adsorption geometries for methanol on the six different kinds of substrates considered: (a) graphene; (b) h-BN; (c) C-BN with an armchair interface; (d) C-BN with a zigzag interface; (e) mixed BCN; (f) triangular graphene island within BN. Color scheme for atomic spheres: C-graphene (green), C-methanol (yellow), H (black), O (red), B (gray), N (blue). . . . . . . . . . . . . . . . . . . . . . . . . . . . . 62

3.10 Bar charts indicating results from DFT calculations for the adsorption energy $E_{\text{ads}}$ and the corresponding value of $E_L$, the contribution to it from London dispersion interactions, for methanol adsorbed on (a) graphene and (b) h-BN. $E_{\text{ads}}$ and $E_L$ are indicated by black and magenta bars, respectively. C1–C8 are eight low-energy stable adsorption geometries shown in Fig. 3.8. . . . . . . . . . . . . . . . . . . . . . . . . . . . 64

3.11 Adsorption energy as a function charge at the interface for graphene island within BN matrix and three striped zigzag C-BN interfaces with neighbouring interfaces 10.85 Å 21.76 Å and 42.79 Å far apart. The plot shows a linear relationship between $E_{ads}$ and the charge at the interface. 65

3.12 (a) Bar chart indicating the contributions from different types of atoms in the substrate to $E_L$, for the lowest energy geometry on each of the six kinds of substrates considered. While the magenta bar shows the total value of $E_L$, arising due to London interactions between the methanol molecule and all the atoms in the substrate, the green, gray and blue bars show the individual contributions to $E_L$ from the interaction of methanol with C, B and N substrate atoms, respectively. The substrate labels C, h-BN, A C-BN, BCN and island structure correspond to graphene, boron nitride, armchair interface, zigzag interface, mixed BCN and island structure of graphene inside BN sheet respectively. (b) Bar chart indicating the stepwise enhancement in adsorption energy $E_{\text{ads}}$ as one proceeds from one substrate to the next, and its break-up into contributions from the three different kinds of van der Waals interactions. The adsorption energy $E_{\text{ads}}$ computed from DFT is shown by black bars, while the contributions from London, Debye and Keesom interactions are shown by magenta, maroon and orange bars, respectively. . . . . . . . . . . . . . . . 66

3.13 Redistribution of electronic charge upon the adsorption of methanol on (a) graphene (b) BN (c) zigzag C-BN (d) armchair C-BN (e) mixed BCN (f) island structure. Red and blue lobes correspond to a gain and loss of electronic charge respectively. The isosurfaces corresponding to $\Delta\rho = \pm 0.0006$ e/(bohr)$^3$ are plotted. Color scheme for atomic spheres: C-graphene (green), C-methanol (yellow), H(black), O (red), B (gray), N (blue). . . . . 67

4.1 Top views of the three kinds of substrates considered (a) graphene (b) periodic graphene oxide and (c) zigzag graphene oxide. Color scheme for atomic spheres: C (gray), O (yellow), H (black). . . . . . . . . . . . . . . . . 80

4.2 Top and side views of the optimal adsorption geometries for (a),(b) water on graphene; (c),(d) water on ZGO; Color scheme for atomic spheres: C-graphene (gray), O-substrate (yellow), O-water (red), H (black). . . . . . . 84

4.3 Top and side views of the optimal adsorption geometries for (a),(b) water on graphene functionalized with one epoxy group; (c),(d) water on graphene functionalized with one hydroxyl group. Color scheme for atomic spheres: C-graphene (gray), O-substrate (yellow), O-water (red), H (black). The dashed blue lines indicate hydrogen bonds. . . . . . . . . . . . . . . 85

4.4 (a) Interaction energies between the two molecules in a water-dimer, between a water molecule and graphene, and between a water molecule and PGO, in their equilibrium geometries.(b) Adsorption energies (per molecule) of a cluster of 10 water molecules on graphene and PGO. The red color bar in the graph denote the energy levels . . . . . . . . . . . . . 86

4.5 Top and side views of examples of configurations (snapshots) for (a),(b) 10 $H_2O$ molecules and (c),(d) 61 $H_2O$ molecules on ZGO. Note the formation of a water bridge in (c),(d), which connects hydrophilic regions. Color scheme for atomic spheres: C-graphene (gray), O-substrate (yellow), O-water (red), H (black). The dashed blue lines indicate hydrogen bonds. . . 88

4.6 Planar average density distribution of water molecules at different loading along $z$ direction. Red, green and yellow color represents the density distribution profiles for 36, 45 and 61 water molecules in the unit cell of ZGO. . . . . . . . . . . . . . . . . . . . . . . . . . . . . . . . . 89

4.7 Mean coordination number of water molecules at different loading computed for hydrophilic and hydrophobic part separately. The hydrophilic part is shown by red bar and the hydrophobic part is shown by green bar and the mean coordination number of bulk water is shown by blue line. . 90

4.8 O-O radial distribution function of bulk water containing 64 water molecules. The first peak occurs at 2.74 Å the first minimum at $r_{min} = 3.26$ Å, and the maximum value of $g$(O-O) is 3.23. . . . . . . . . . . . . . . . . . . . 91

4.9 mean value of number of h-bonds between water molecules at different loading computed for hydrophilic and hydrophobic part separately. The hydrophilic part is shown by red bar and the hydrophobic part is shown by green bar and the mean coordination number of bulk water is shown by blue line. . . . . . . . . . . . . . . . . . . . . . . . . . . . . . 92

4.10 Change in orientation of water molecules with coverage. The bars show the angle $\theta$ made by the $z$ component of the dipole moment of the water molecules with the $z$-axis, computed for the hydrophilic and hydrophobic parts separately. The hydrophilic part is shown by the red bar and the hydrophobic part is shown by the green bar. . . . . . . . . . . . . . . . . 94

4.11 Mean squared displacement (MSD) of water molecules at different loading computed using shifted time origin for (a) 36 (b) 45 and (c) 61 water molecules on ZGO. The parts of the curves marked with black dashed lines indicate the diffusive regions used to compute the diffusion constant $D$. . . . . . . . . . . . . . . . . . . . . . . . . . . . . . . . . . 95

4.12 Dipole orientational autocorrelation of water molecules at different loading computed using shifted time origin for (a) 36 (b) 45 and (c) 61 water molecules on ZGO. . . . . . . . . . . . . . . . . . . . . . . . . . . 97

5.1 Results from experiments by Ojha *et al.*[35] (a) Elemental mapping of $Mo_2C$-$Mo_2N$ composite nanowires shows the presence of Mo, C and N in the composite system (b) Current density of pure $Mo_2C$ and pure $Mo_2N$ at 0.4 V overpotential (c) Current density of doped $Mo_2C$-$Mo_2N$ compounds at 0.4 V overpotential . . . . . . . . . . . . . . . . . . . . . . . . . 109

5.2 Side views of surface slabs used for calculations on $Mo_2C_{1-x}N_x$ surfaces. For (a) $x$ = 0, (b) $x$ = 0.25, (c) $x$ = 0.375 and (d) $x$ = 0.5 we have considered the orthorhombic(100) surface and for (e) $x$ = 0.625, (f) $x$ = 0.75 and (g) $x$ = 1 we have considered the tetragonal(001) surface. Note that the angle of view is slightly different in the upper and lower panels. . . . . . . . 109

5.3 Difference in total energy between tetragonal and orthorhombic structures, for bulk $Mo_2C_{1-x}N_x$, a a function of N concentration $x$. Red circles and blue diamonds indicate results with and without van der Waals interactions incorporated, respectively. Note that a positive/negative value indicates the orthorhombic/tetragonal structure is favored. . . . . . . . . 114

5.4 Changes in lattice parameters with N concentration $x$ in bulk $Mo_2C_{1-x}N_x$ structures. (a)-(c) Change in lattice parameters with $x$ for orthorhombic structure, (d) change in volume with $x$ for orthorhombic structure, (e)-(g) change in lattice parameters with $x$ for tetragonal structure. and (h) Change in volume with $x$ for tetragonal structure. Filled circles and open diamonds are results with and without van der Waals interactions incorporated. . . . . . . . . . . . . . . . . . . . . . . . . . . . . . . . . 115

5.5 (a)-(c) Side view of (100), (010) and (001) surface slabs for $Mo_2C$ in orthorhombic structure. (d)-(e) Side view of (100) and (001) surface slabs for $Mo_2N$ in tetragonal structure. . . . . . . . . . . . . . . . . . . . . . . 116

5.6 Side views of H atom adsorbed on $Mo_2C_{1-x}N_x$ surfaces. For $x$ = 0, 0.25, 0.375 and 0.5 we have considered the orthorhombic(100) surface and for $x$ = 0.625, 0.75 and 1 we have considered the tetragonal(001) surface. Note that the angle of view is different in the top and bottom rows; in all cases H atoms are adsorbed in a hollow site. . . . . . . . . . . . . . . . . . . . 117

5.7 Adsorption energy of single H atom on $Mo_2C_{1-x}N_x$. With increasing N concentration, adsorption energy decreases. For $x$ = 0, 0.25, 0.375 and 0.5 we have taken orthorhombic structure and for $x$ = 0.625, 0.75 and 1,we have taken tetragonal structure. . . . . . . . . . . . . . . . . . . . . . 118

5.8 (a) Change in charge on Mo as a function of N doping concentration (b) Correlation between position of d-band center and charge on Mo (c) Correlation between adsorption energy of single H and position of d-band center for $Mo_2C_{1-x}N_x$. For $x$ = 0, 0.25, 0.375 and 0.5 we have taken orthorhombic structure and for $x$ = 0.625, 0.75 and 1 we have taken tetragonal structure. . . . . . . . . . . . . . . . . . . . . . . . . . . . . . 119

5.9 (a) experimental result for $\log_{10}$ of current density at 0.4 V overpotential as a function of different N concentrations in $Mo_2C_{1-x}N_x$ (b) experimental result for $\log_{10}$ of current density at 0.4 V overpotential vs. theoretical result for H adsorption energy for different N concentrations in $Mo_2C_{1-x}N_x$ 120

5.10 Calculated values of Gibbs free energy $\Delta G$ for hydrogen adsorption. . . 121

6.1 Results from DFT for (a) electronic band structure along high-symmetry directions of the Brillouin zone, and (b) projected density of states (PDOS) of bulk $CsPbBr_3$ in the cubic structure. The figure on the right shows the PDOS, with the DOS projected onto Br-4p (blue), Pb-6s (maroon) and Pb-6p (green) orbitals. In both figures, the dashed line shows the position of the Fermi level. . . . . . . . . . . . . . . . . . . . . . . . . . . . 135

6.2 Change in band gap with lattice parameter of cubic $CsPbBr_3$ (a) without SOC and (b) with SOC. Note that without SOC, the change is monotonic, whereas with SOC, it is non-monotonic due to the presence of a band inversion. Note the position of the point in (b) that indicates the equilibrium lattice constant for $CsPbBr_3$. . . . . . . . . . . . . . . . . . . . . . . . 136

6.3 (a) Movement of valence band and conduction band with lattice parameter (b) Change in different orbital contributions with lattice parameter.All positions are measured with respect to a deep-lying core level that does not shift with lattice parameter. . . . . . . . . . . . . . . . . . . . . . . . 137

6.4 Projected band-structure of bulk $CsPbBr_3$ at optimized lattice constant. The color of each point indicates the orbital character of the band at that wave-vector. A blue color indicates fully Br 4p character, yellow color indicates fully Pb 6p character, and the intermediate colors denote appropriate amount of partial contributions from Br 4p and Pb 6p . . . . . 139

6.5 Movement of valence and conduction band edges with lattice parameter. Results at (a) $a$ = 5.69 Å and (b) 5.52 Å. In each case, the left and right panels show the results without with SOC, respectively. The blue and green colors indicate bands that have primarily Pb 6p and Br 4p character, respectively. . . . . . . . . . . . . . . . . . . . . . . . . . . . . . 140

6.6 Change in band gap of Cubic $CsPbBr_3$ with Sn doping (a) without SOC and (b) with SOC . . . . . . . . . . . . . . . . . . . . . . . . . . . . 141

6.7 Change in lattice constant with Sn doping . . . . . . . . . . . . . . . . . 142

6.8 Position of atomic levels for (a) $CsPbBr_3$ and (b)$CsSn_0.25Pb_0.75Br_3$. Green, blue and red colors indicate predominantly Pb 6p, Br 4p and Sn 5p character, respectively. In each case, the left and right panels show results without and with SOC, respectively. . . . . . . . . . . . . . . . . . . . . . 142

7.1 Experimental results (from our collaborators in the group of Prof. Ranjani Viswanatha) (a) Schematic diagram of gated PL (b) Room temperature gated PL emission for different Mn doped $CsPbBr_{3-3x}Cl_x$ nanocrystal samples denoted by MP1 to MP5 . . . . . . . . . . . . . . . . . . . . 153

7.2 Structure of cubic (a) $CsPbBr_3$ (b) $CsPbCl_3$ (c) Mn-doped $CsPbBr_3$ (d) Mn-doped $CsPbCl_3$. Doping concentration of Mn is 12.5% in (c) and (d) Color scheme for atomic spheres: Cs (sky blue), Pb (green) Br (blue) Cl (light green). . . . . . . . . . . . . . . . . . . . . . . . . . . . . . . . . 154

7.3 DFT results for electronic band structure of the undoped halide perovskites. $CsPbBr_3$ (a) without and (b) with spin-orbit coupling. The conduction band has Pb 6p character and the valence band arises from Br 4p and Pb 6s orbitals. Band structure of $CsPbCl_3$ (c) without and (d) with spin-orbit coupling. The conduction band has Pb 6p character and the valence band arises from Cl 3p and Pb 6s orbitals. . . . . . . . . . . . . . . . . . . . . . . . 156

7.4 Projected band structure of (a) spin up and (b) spin down states of 12.5% Mn-doped $CsPbBr_3$. The contributions from Mn 3d, Pb 6p and Br 4p are represented by red, green and blue colors respectively. The intermediate colors shown by the color triangle denotes the amount of overlap between the orbitals. Note that Mn hybridizes with the valence band in the spin up states and with the conduction band in the spin down states. . . . . . 158

7.5 Projected band structure of the conduction band for Mn doped $CsPbBr_3$ showing the contributions from Mn 3d, Pb 6p and Br 4p orbitals (a) without and (b) with spin-orbit coupling. The contributions from Mn 3d, Pb 6p and Br 4p are represented by red, green and blue colors respectively. The intermediate colors shown by the color triangle denotes the amount of overlap between the orbitals . . . . . . . . . . . . . . . . . . . . . . . . 158

7.6 Projected phonon spectrum, as calculated from DFPT, for (a) Mn-doped $CsPbBr_3$ and (b) Mn-doped $CsPbCl_3$. The branches are colored according to their weights on the different atoms in the unit cell, as shown in the RGB color triangle. . . . . . . . . . . . . . . . . . . . . . . . . . . . 160

7.7 (a),(b) Eigenvectors corresponding to the two degenerate phonon modes $b_{d5}(1)$ and $b_{d5}(2)$ of Mn-doped CsPbBr$_3$. (c),(d) The presence of electron-phonon coupling is evidenced from the shift in the electronic bands under atomic displacement corresponding to the two modes Mn-doped CsPbBr$_3$. Green solid lines: equilibrium band structure. Red dotted lines: band structure of the structure after distorted along the mode vector with an atomic displacement of 0.06 $\mathring{A}\dot{C}$olor scheme for atomic spheres: Cs (sky blue), Pb (green) Br (blue) Mn (red). . . . . . . . . . . . . . . . . . . . . . . 162

# List of Tables

4.1 Fitting parameters, obtained using Eq. (4.8), for dipole orientational correlation function for 36, 45 and 61 water molecules on ZGO, and the resulting values for relaxation time $\tau$. . . . . . . . . . . . . . . . . . . . . . . . 98

5.1 Lattice parameter of bulk $Mo_2C$ and $Mo_2N$ . . . . . . . . . . . . . . . . . . 113

Chapter 1

# Introduction

## 1.1 Rational Design of Materials for Energy Applications

The work done in this thesis has been performed in the spirit of 'rational design of materials'. Most of the materials we use today for various applications have been developed through a process of trial and error or accidental discovery. The goal now is to replace this by a process of targeted search, where we are able to predict beforehand which combination of elements from the periodic table, taken in which proportion, will result in a desired property that is suitable for a specific application.

The first step of the rational design of materials is to define the problem clearly. After the problem is defined, conceptual design of materials and prediction of their properties using different theoretical tools are performed. These properties are then matched with the experimental results. If there is a lack of agreement between the experimental results and theoretical predictions, a thorough analysis is performed to find out the reasons for the mismatch, and a redesigning of materials is performed. We note that, typically, experiments are more costly and time consuming, when compared to theoretical calculations. So a proper theoretical understanding and a program of rational design can help experimentalists to save time by targeting specified regions of chemical space. *Ab* *initio* density functional theory[1;2], molecular dynamics,[3] and Monte Carlo simulations[4] are some of the popular computational techniques that can be used.

In this thesis I have done 'rational design' of materials by tuning the electronic, vibrational, structural, dynamical and adsorption properties of various materials. While the systems studied in the thesis are diverse, the projects have in common a research philosophy motivated by the rational design of materials for energy applications.

In Chapter 1, I have provided a brief introduction to the problems studied in the thesis.

In Chapter 2 I have discussed the computational techniques used in the thesis. These include *ab initio* density functional theory,[1;2] *ab initio* density functional perturbation theory (DFPT),[5;6] and *ab initio* molecular dynamics.[7–9]

In Chapter 3 I have studied the adsorption of the polar methanol molecule on polar graphene-BN interfaces. Weak binding plays an important role in applications such as gas storage and adsorptive cooling. The energy range for the weak binding is of the order of a tenth of an eV which falls in the range of van der Waals interactions. I note that much of the previous work on weak binding has focused on cases where the adsorbed molecule is a non-polar molecule such as hydrogen, methane and carbon dioxide.[10–12] I have tuned the charge at the graphene-BN interfaces between the two materials by varying the orientation and geometry of the interface, so as to maximize the adsorption energy of the methanol molecule. The higher the charge that is localized at the interface, the greater the electrostatic interaction between this interface charge and the dipole moment of the molecule, and hence the larger the enhancement in adsorption energy. Possible applications of this work include the area of adsorption cooling, which offers a promising alternative to conventional refrigeration techniques which make use of the alternating compression and expansion of refrigerant materials.

In Chapter 4 I have studied the properties of water on a graphene oxide system. This system is of great interest because of studies that indicate that it may display a very high proton conductivity,[13;14] as well as allow permeation of water though being impermeable to most gases.[15] I study how the structural and dynamical properties of this system change as a function of water uptake.

In Chapter 5 I look at the problem of catalysts for water splitting. I have attempted to understand the finding by our experimental collaborators that the hydrogen evolution reaction (HER) activity of molybdenum carbide – molybdenum nitride composite systems is enhanced as compared to pure molybdenum carbide or pure molybdenum nitride systems. To do this, I have studied the adsorption of a H atom on molybdenum carbide, molybdenum nitride and mixed systems. In this chapter I have shown that one can tune the adsorption energy of the hydrogen atom on the surfaces of these materials by changing the relative concentration of C and N; this in turn affects the HER activity.

Bulk halide perovskites show a red shift upon doping with Sn.[16–18] In contrast, our experimental collaborators have found that nanocrystals of these materials display a blue shift upon Sn doping. In Chapter 6 I have investigated theoretically the reason for this anomalous change in band gap in the Sn-doped nanocrystals. In this chapter I have tuned the electronic properties of perovskite materials by Sn doping.

Our experimental collaborators have found that Mn-doped halide perovskite nanocrystals display a delayed emission. In Chapter 7 I have investigated theoretically the possible sources of this delayed emission, and the effect of spin-orbit coupling in these materials. In this chapter I have shown that one can tune the electronic and vibrational properties of perovskite materials by Mn doping.

Above, I have discussed the materials and properties considered in this thesis. Let us now briefly consider the theoretical techniques used to investigate these questions. In Chapter 2 I have described the computational techniques and theoretical formalism used in this thesis. The main output of an *ab initio* density functional theory (DFT)[1;2] calculation is the total energy of the system. I have used the total energy from DFT calculations to perform the studies in Chapters 3 – 7.

In Chapter 3, I have studied the interaction of methanol with graphene-BN interfaces, and in Chapter 4 I have studied the interaction of water with graphene oxide. Now, as both these interactions have strengths that fall within the range of weak binding, van der Waals interactions play an important role in such cases. Even in Chapter 5, where I study the HER on molybdenum carbides and nitrides, I have found that incorporating van der Waals interactions is crucial for correctly determining the relative stability of the orthorhombic and tetragonal structures for the carbide and nitride materials. Similarly, in Chapter 6 we have found that van der Waals interactions play a crucial role in determining the correct structures and electronic properties for perovskite materials. It is well known that London dispersion interactions are not incorporated in ‘conventional DFT’. So, in order to include the dispersion interactions, in Chapters 3, 4, 5 and 6, I have used the computationally affordable ‘DFT-D2’ treatment introduced by Grimme,[19] to incorporate van der Waals interactions.

The inorganic halide perovskite structures I have considered in Chapters 6 and 7 contain Pb atoms. Now as Pb is a heavy atom, the (relativistic) spin-orbit interactions play a crucial role in determining the electronic structure. So in Chapters 6 and 7, in order to appropriately include spin-orbit interactions, I have used fully relativistic pseudopotentials.[20]

In Chapter 5, to see the HER activity of molybdenum carbide, nitride and mixed structures for different concentrations of C and N, I have calculated the Gibbs free energy. This also requires a computation of the zero point energies, and hence vibrational energies, in the adsorbed and gas phase systems. The vibrational frequencies that are necessary for this computation are calculated using *ab initio* density functional perturbation theory (DFPT).[5;6] Similarly, also in Chapter 7, I have used DFPT to calculate the phonon spectra of halide perovskites.

To calculate the structural and dynamical properties of water on a graphene oxide substrate, I have performed *ab initio* molecular dynamics simulations.[7–9] More specifically, I have performed Car-Parrinello molecular dynamics (CPMD) [21] as it is computationally cheaper than Born-Oppenheimer molecular dynamics (BOMD).[7]

As already mentioned above, in Chapter 3, I have studied the adsorption of a polar molecule on a substrate with polar interfaces. I have considered methanol as the polar molecule and graphene-BN as the substrate. At some graphene-BN interfaces, lines of charge appear, which increase the adsorption energy of methanol as compared to over just graphene or just h-BN. The charges at the interface change depending on the orientation and geometry of the interface, both of which I have varied, so as to tune the adsorption strength. To compare the adsorption of methanol on differently engineered substrates, the substrates I have considered are graphene, boron nitride, striped domains with armchair interfaces or zigzag interfaces, mixed BCN, and finally a triangular graphene island in a boron nitride matrix. This last triangular island is found to have more charge localized at the interface than all the other substrate geometries. Indeed, the highest adsorption strength of methanol is observed on this triangular island, with an enhanced adsorption energy of 65% relative to that over graphene. I analyze the binding by separating out the contributions from different kinds of van der Waals interactions. The London dispersion contribution captures the majority of the binding, and is approximately the same for all the substrates considered. The contribution from Debye interactions, which is the interaction between permanent dipole moments/charges and induced moments/charges of the substrate and molecule is found to be fairly small. My results suggest that the enhancement in binding on going to the different kinds of substrates I have considered arises almost entirely from Keesom interactions, which are the interactions between permanent moments/charges of the substrates and molecules; the electrostatic interaction between the permanent dipole moment of the methanol molecule and the lines of charge that are formed at graphene-BN interfaces can be labeled as Keesom interactions.

Fuel cells have several benefits over conventional combustion-based technologies. One possible application of them is in passenger vehicles. They can operate at higher efficiencies than combustion engines and can convert the chemical energy to electrical energy. Several kinds of fuel cells are available and each has its advantages and limitations. Proton exchange membrane (PEM) fuel cells deliver high power density and have low weight and volume compared to other types of fuel cells. PEM fuel cells are used primarily for transportation applications. The electrolyte plays a key role in fuel cells. Ideally, it must permit transport of only the appropriate ions (protons) between the anode and cathode. Due to its wide range of possible operating conditions and high conductivity, a material called nafion has been the most commonly used electrolyte in PEM fuel cells. However, there are certain limitations of nafion: high cost, fuel crossover, and the water uptake capacity is also not so high. Recently it has been shown that graphene oxide could be a useful alternative to nafion.[14] Graphene oxide has a water uptake capacity of 31.1%, as compared to 25.6% in nafion[22]. Moreover, graphene oxide is much cheaper than nafion. In recent experiments, it has been shown that the conductivity of a single layer of graphene oxide increases almost linearly from $6 \times 10^{-7}$ Scm$^{-1}$ at 55% relative humidity to $2 \times 10^{-4}$ S cm$^{-1}$ at 90% relative humidity.[13;14] In Chapter 4, I have attempted to study some of the factors affecting the proton conductivity through water on a graphene oxide substrate. I have looked at the energetics of water on graphene oxide by performing static density functional theory calculations, and the structural and dynamical properties by performing *ab initio* molecular dynamics simulations. As the coverage of water molecules on graphene oxide increases, I find that the coordination number of water molecules and the number of hydrogen bonds per water molecule increases. Also with increasing content of water, the diffusion coefficient of water on the surface increases, and the relaxation time decreases. These features should contribute to the fast proton transport on graphene oxide used as an electrolyte in Proton Exchange Membrane Fuel Cells.

Hydrogen is a promising renewable and sustainable energy source. Although hydrogen is the most abundant element on earth, it does not exist as a free molecule. The most effective way of generating hydrogen is through electrolysis of water, which can be divided into two reactions: the hydrogen evolution reaction (HER) and the oxygen evolution reaction (OER). Both these reactions require an efficient catalyst to lower the overpotential of the reaction. Though Pt has been found to be an efficient electrocatalyst for hydrogen production, it is costly and scarce in nature. So a cost effective alternative is highly desirable. It has been shown previously that earth abundant transition metal compounds such as borides, carbides, nitrides, chalcogenides and phospides can be effective alternatives to Pt.[23–28] In Chapter 5, we have shown that $Mo_2C$-$Mo_2N$ composite structures can be a useful alternative to Pt and show better HER activity than either the pure carbide or pure nitride at low overpotentials. We also show that N-rich samples show better HER activity than C-rich samples. This matches with results obtained by our experimental collaborators. We have calculated the Gibbs free energy to predict the HER activity of the samples. We have also obtained the somewhat surprising result that incorporation of van der Waals interactions in the calculations is essential to correctly reproduce the experimental findings for the relative structural stability of two competing structures (orthorhombic vs. tetragonal) for the bulk carbide and nitride structures.

For bulk inorganic halide perovskites, cation doping results in a red shift in the photoluminescence, i.e, the band gap decreases as the cation doping concentrations increases.[16–18] Our experimental collaborators have recently found a blue shift in Sn-doped perovskite nanocrystals, i.e., the band gap increases as the Sn concentration concentration in the perovskite nanocrystals increases. In Chapter 6, I have performed calculations to explore the reason for the unusual band-gap change in Sn-doped perovskite nanocrystals as compared to the bulk. Van der Waals interactions and spin-orbit coupling play a key role in our calculations. Our experimental collaborators found that the nanocrystals of these materials are stable in the cubic structure, whereas for bulk, the orthorhombic structure is favored. I find that for the cubic perovskite structure, there is a band inversion which results in blue shift in band gap upon Sn doping.

To achieve cost and energy efficient devices in the field of lighting, reducing energy losses is a big goal. Energy losses mainly arise from non-radiative recombination like Auger recombination[29] and losses due to surface defects.[30;31] A slow supply of excited state electrons from Mn states to the host levels could reduce the losses. Our experimental collaborators have recently observed delayed fluorescence in Mn-doped perovskite nanocrystals. In Chapter 7 I have investigated the reason for the delayed fluorescence. I find that the effects of spin-orbit coupling (SOC) play an extremely important role for these systems, as SOC is responsible for the position of the Mn levels getting buried deep within the conduction band. I have also shown that Mn dopant atoms have a significant amount of both electronic and vibrational coupling with Pb atoms. This vibrational coupling, as well as electron-phonon coupling, is responsible for the delayed fluorescence observed for Mn-doped perovskite systems.

In Chapter 8, the main results of each chapter are summarized, and possible directions for future work are discussed.

## Bibliography

[1] W. Kohn and L. J. Sham, "Self-consistent equations including exchange and correlation effects," *Physical review*, vol. 140, no. 4A, p. A1133, 1965.

[2] P. Hohenberg and W. Kohn, "Inhomogeneous electron gas," *Physical review*, vol. 136, no. 3B, p. B864, 1964.

[3] A. Rahman, "Correlations in the motion of atoms in liquid argon," *Physical review*, vol. 136, no. 2A, p. A405, 1964.

[4] N. Metropolis and S. Ulam, "The monte carlo method," *Journal of the American statistical association*, vol. 44, no. 247, pp. 335–341, 1949.

[5] S. Baroni, P. Giannozzi, and A. Testa, "Greenfis-function approach to linear response in solids," *Physical Review Letters*, vol. 58, no. 18, p. 1861, 1987.

[6] S. Baroni, S. De Gironcoli, A. Dal Corso, and P. Giannozzi, "Phonons and related crystal properties from density-functional perturbation theory," *Reviews of Modern Physics*, vol. 73, no. 2, p. 515, 2001.

[7] R. Car and M. Parrinello, "Unified approach for molecular dynamics and density-functional theory," *Physical review letters*, vol. 55, no. 22, p. 2471, 1985.

[8] M. C. Payne, M. P. Teter, D. C. Allan, T. Arias, and a. J. Joannopoulos, "Iterative minimization techniques for ab initio total-energy calculations: molecular dynamics and conjugate gradients," *Reviews of modern physics*, vol. 64, no. 4, p. 1045, 1992.

[9] M. E. Tuckerman, "Ab initio molecular dynamics: basic concepts, current trends and novel applications," *Journal of Physics: Condensed Matter*, vol. 14, no. 50, p. R1297, 2002.

[10] Y. Miyamoto, A. Rubio, M. L. Cohen, and S. G. Louie, "Chiral tubules of hexagonal $BC_2N$," *Physical Review B*, vol. 50, no. 7, p. 4976, 1994.

[11] O. Stephan, P. Ajayan, C. Colliex, P. Redlich, J. Lambert, P. Bernier, and P. Lefin, "Doping graphitic and carbon nanotube structures with boron and nitrogen," *Science*, vol. 266, no. 5191, pp. 1683–1685, 1994.

[12] L. Ci, L. Song, C. Jin, D. Jariwala, D. Wu, Y. Li, A. Srivastava, Z. Wang, K. Storr, L. Balicas, *et al.*, "Atomic layers of hybridized boron nitride and graphene domains," *Nature materials*, vol. 9, no. 5, p. 430, 2010.

[13] K. Hatakeyama, M. R. Karim, C. Ogata, H. Tateishi, A. Funatsu, T. Taniguchi, M. Koinuma, S. Hayami, and Y. Matsumoto, "Proton conductivities of graphene oxide nanosheets: single, multilayer, and modified nanosheets," *Angewandte Chemie International Edition*, vol. 53, no. 27, pp. 6997–7000, 2014.

[14] M. R. Karim, K. Hatakeyama, T. Matsui, H. Takehira, T. Taniguchi, M. Koinuma, Y. Matsumoto, T. Akutagawa, Nakamura, *et al.*, "Graphene oxide nanosheet with high proton conductivity," *Journal of the American Chemical Society*, vol. 135, no. 22, pp. 8097–8100, 2013.

[15] R. Nair, H. Wu, P. Jayaram, I. Grigorieva, and A. Geim, "Unimpeded permeation of water through helium-leak–tight graphene-based membranes," *Science*, vol. 335, no. 6067, pp. 442–444, 2012.

[16] H.-J. Feng, T. R. Paudel, E. Y. Tsymbal, and X. C. Zeng, “Tunable optical properties and charge separation in $CH_3NH_3Sn_xPb_{1-x}I_3/TiO_2$-based planar perovskites cells,” *Journal of the American Chemical Society*, vol. 137, no. 25, pp. 8227–8236, 2015.

[17] D. Zhao, Y. Yu, C. Wang, W. Liao, N. Shrestha, C. R. Grice, A. J. Cimaroli, L. Guan, R. J. Ellingson, K. Zhu, *et al.*, “Low-bandgap mixed tin–lead iodide perovskite absorbers with long carrier lifetimes for all-perovskite tandem solar cells,” *Nature Energy*, vol. 2, no. 4, p. 17018, 2017.

[18] Y. Ogomi, A. Morita, S. Tsukamoto, T. Saitho, N. Fujikawa, Q. Shen, T. Toyoda, K. Yoshino, S. S. Pandey, T. Ma, *et al.*, “$CH_3NH_3Sn_xPb_{1-x}I_3$ perovskite solar cells covering up to 1060 nm,” *The journal of physical chemistry letters*, vol. 5, no. 6, pp. 1004–1011, 2014.

[19] S. Grimme, “Semiempirical GGA-type density functional constructed with a long-range dispersion correction,” *Journal of computational chemistry*, vol. 27, no. 15, pp. 1787–1799, 2006.

[20] A. Dal Corso and A. M. Conte, “Spin-orbit coupling with ultrasoft pseudopotentials: Application to au and pt,” *Physical Review B*, vol. 71, no. 11, p. 115106, 2005.

[21] R. Car and M. Parrinello, “Unified approach for molecular dynamics and density-functional theory,” *Physical review letters*, vol. 55, no. 22, p. 2471, 1985.

[22] T. Bayer, S. Bishop, M. Nishihara, K. Sasaki, and S. M. Lyth, “Characterization of a graphene oxide membrane fuel cell,” *Journal of Power Sources*, vol. 272, pp. 239–247, 2014.

[23] H. Vrubel and X. Hu, “Molybdenum boride and carbide catalyze hydrogen evolution in both acidic and basic solutions,” *Angewandte Chemie International Edition*, vol. 51, no. 51, pp. 12703–12706, 2012.

[24] M. D. Scanlon, X. Bian, H. Vrubel, V. Amstutz, K. Schenk, X. Hu, B. Liu, and H. H. Girault, "Low-cost industrially available molybdenum boride and carbide as fiplatinum-likefi catalysts for the hydrogen evolution reaction in biphasic liquid systems," *Physical Chemistry Chemical Physics*, vol. 15, no. 8, pp. 2847–2857, 2013.

[25] R. Michalsky, Y.-J. Zhang, and A. A. Peterson, "Trends in the hydrogen evolution activity of metal carbide catalysts," *ACS Catalysis*, vol. 4, no. 5, pp. 1274–1278, 2014.

[26] W.-F. Chen, J. T. Muckerman, and E. Fujita, "Recent developments in transition metal carbides and nitrides as hydrogen evolution electrocatalysts," *Chemical communications*, vol. 49, no. 79, pp. 8896–8909, 2013.

[27] B. Cao, G. M. Veith, J. C. Neuefeind, R. R. Adzic, and P. G. Khalifah, "Mixed close-packed cobalt molybdenum nitrides as non-noble metal electrocatalysts for the hydrogen evolution reaction," *Journal of the American Chemical Society*, vol. 135, no. 51, pp. 19186–19192, 2013.

[28] W.-F. Chen, K. Sasaki, C. Ma, A. I. Frenkel, N. Marinkovic, J. T. Muckerman, Y. Zhu, and R. R. Adzic, "Hydrogen-evolution catalysts based on non-noble metal nickel–molybdenum nitride nanosheets," *Angewandte Chemie International Edition*, vol. 51, no. 25, pp. 6131–6135, 2012.

[29] A. Chernenko, P. Dorozhkin, V. Kulakovskii, A. Brichkin, S. Ivanov, and A. Toropov, "Auger recombination of excitons in semimagnetic quantum dot structure in a magnetic field," *Physical Review B*, vol. 72, no. 4, p. 045302, 2005.

[30] M. M. Krause, J. Mooney, and P. Kambhampati, "Chemical and thermodynamic control of the surface of semiconductor nanocrystals for designer white light emitters," *ACS nano*, vol. 7, no. 7, pp. 5922–5929, 2013.

[31] V. Pinchetti, A. Anand, Q. A. Akkerman, D. Sciacca, M. Lorenzon, F. Meinardi, M. Fanciulli, L. Manna, and S. Brovelli, "Trap-mediated two-step sensitization of

manganese dopants in perovskite nanocrystals," *ACS Energy Letters*, vol. 4, no. 1, pp. 85–93, 2018.

Chapter 2

# Methods and Formalism

In this chapter, I briefly review the formalism underlying the methods used in this thesis, as well as outline some technical details of how computations are performed.

## 2.1 The Many-Body Problem

The Hamiltonian for a many-body system of nuclei and electrons is given by:[1]

$$\hat{H} = -\sum_{I} \frac{\hbar^2}{2M_I} \nabla_I^2 - \frac{\hbar^2}{2m_e} \sum_{i} \nabla_i^2 + \frac{1}{2} \sum_{I \neq J} \frac{Z_I Z_J e^2}{\left|\mathbf{R}_I - \mathbf{R}_J\right|} - \sum_{i,I} \frac{Z_I e^2}{|\mathbf{r}_i - \mathbf{R}_I|} + \frac{1}{2} \sum_{i \neq j} \frac{e^2}{\left|\mathbf{r}_i - \mathbf{r}_j\right|}, \quad (2.1)$$

where the nuclear positions, nuclear masses and the atomic numbers of the atoms in the system are given by $\mathbf{R}_I$, $M_I$ and $Z_I$ respectively, and the indices $I, J$ run over all the nuclei in the system. The electronic positions, electronic mass and charge are given by $\mathbf{r}_i$, $m_e$ and $e$ respectively, with indices $i$, $j$ that run over all the electrons in the system, and $\hbar$ is Planck's constant divided by $2\pi$. The first two terms of the right hand side of Eq. (2.1) are respectively the nuclear and electronic kinetic energies. The subsequent terms take into account the nuclei-nuclei Coulomb repulsion, electron-nuclei Coulomb attraction and the electron-electron Coulomb repulsion, respectively.

The many body Schrödinger equation is then

$$H\Psi(\mathbf{R},\mathbf{r}) = E\Psi(\mathbf{R},\mathbf{r}). \tag{2.2}$$

Though we are able to write down the Hamiltonian, this many-body problem is basically impossible to solve (even numerically), especially when the number of particles is large. For a solid, the number of particles is typically of the order of $10^{23}$.

### 2.1.1 Born-Oppenheimer or Adiabatic Approximation

The Born-Oppenheimer approximation is a way to separate the nuclear and electronic degrees of freedom. The nuclei are much heavier than the electrons.[2] So the time scales related to the electronic motion are much smaller than the time scales related to the nuclear motion. Thus the nuclei can be considered as effectively stationary in electronic time scales. The electronic Hamiltonian can thus be solved using a time-independent Schrödinger equation for electrons in a stationary external (nuclear) potential.

Applying this approximation to Eq. (2.1), the first term on the right hand side (RHS) becomes very small and can be treated as a perturbation. The wavefunctions and energies of the electrons can be described in such a way that they have only a parametric dependence on the nuclear postions $\mathbf{R}$. The wavefunction of the total system, $\Psi(\mathbf{R},\mathbf{r})$ can be written as:

$$\Psi(\mathbf{R},\mathbf{r}) = \sum_s \chi_s(\mathbf{R})\psi_s(\mathbf{R},\mathbf{r}), \tag{2.3}$$

where $\{\psi_s(\mathbf{R},\mathbf{r})\}$ is a complete set of electronic eigenstates for each $\mathbf{R}$, and $\chi_s(\mathbf{R})$ are the nuclear wavefunctions. Note that the position vectors $\mathbf{r}$ and $\mathbf{R}$ denote the set of all position vectors $\{\mathbf{r}_i\}$ and $\{\mathbf{R}_I\}$ of the electrons and the nuclei respectively. Now, the many-body equation in Eq. (2.2) can be re-written as a set of two coupled differential equations:

$$\left[-\frac{\hbar^2}{2m_e}\sum_i \nabla_i^2 + \frac{1}{2}\sum_{I\neq J}\frac{Z_I Z_J e^2}{\left|\mathbf{R}_I - \mathbf{R}_J\right|} - \sum_{i,I}\frac{Z_I e^2}{|\mathbf{r}_i - \mathbf{R}_I|} + \frac{1}{2}\sum_{i\neq j}\frac{e^2}{\left|\mathbf{r}_i - \mathbf{r}_j\right|}\right]\psi_s(\mathbf{R},\mathbf{r}) = E_s(\mathbf{R})\psi_s(\mathbf{R},\mathbf{r}), \tag{2.4}$$

$$\left[-\sum_I \frac{\hbar^2}{2M_I}\nabla_I^2 + E_s(\mathbf{R})\right]\chi_s(\mathbf{R}) = \varepsilon\chi_s(\mathbf{R}). \tag{2.5}$$

$E_s(\mathbf{R})$ is the eigenvalue of Eq. (2.4), and is the smeared out potential seen by the nuclei due to the speedy electrons. $E_s(\mathbf{R})$ is called the Born-Oppenheimer potential energy surface, and when it is known, Eq. (2.5) becomes easily solvable. The solution to Eq. (2.4), however, is not straightforward within the quantum mechanical framework and requires further approximations to deal with the Coulomb two-body terms and the exchange and correlation interactions.

### 2.1.2 Density Functional Theory

Density Functional theory (DFT) was a landmark development in the field of computational science that enabled electronic structure theory to be applied to real problems. It describes a complete transformation of the Schrödinger equation, one in which the many-body $N$-electron wavefunction is replaced by the electronic density as the basic variable. This makes the calculation much simpler as it implies that the electronic density (which depends only on position, which is a three-variable quantity) can give us all the information contained in the wavefunction (which is a $3N$-variable quantity).

The electronic density, $n(\mathbf{r})$, is determined from the many-electron wavefunction using the electronic density operator, $\hat{n}(\mathbf{r})$, as given below:[1]

$$n(\mathbf{r}) = \frac{\langle\psi|\hat{n}(\mathbf{r})|\psi\rangle}{\langle\psi|\psi\rangle};\ \hat{n}(\mathbf{r}) = \sum_{i=1}^{N}\delta(\mathbf{r} - \mathbf{r}_i). \tag{2.6}$$

DFT further simplifies the problem by replacing the many-body interacting electron system with a single-electron non-interacting system and including a term that incorporates all the many-body effects in the system through a term that describes the exchange and correlation between the electrons.

### Hohenberg-Kohn Theorems

The basic framework of DFT is based on two theorems introduced by Hohenberg and Kohn.[3] The theorems are as stated below.

**Theorem I:** For any system of interacting particles in an external potential $V_{ext}(\mathbf{r})$, the potential $V_{ext}(\mathbf{r})$ is determined uniquely, up to an additive constant, by the ground state particle density $n_0(\mathbf{r})$.[1]

This theorem suggests that the external potential in a system can be uniquely determined from its ground state electronic density. Using this external potential, the Schrödinger equation can be solved to determine the many-body wavefunction; and from the wavefunction, the observable electronic density can be determined. This allows a self-consistent procedure to be utilized to determine the true ground state density and the true ground state wavefunction of the system.

**Theorem II:** A universal functional for the energy $E[n]$ in terms of $n(\mathbf{r})$ can be defined, valid for any external potential $V_{ext}(\mathbf{r})$. For any particular $V_{ext}(\mathbf{r})$, the exact ground state energy of the system is the global minimum value of this functional, and the density $n(\mathbf{r})$ that minimizes the functional is the exact ground state density $n_0(\mathbf{r})$.[1]

The ground state expectation value of any observable can be written as a functional of $n_0(\mathbf{r})$ of the system; energy being the most important observable that is calculated. This second theorem suggests that the energy that corresponds to the true ground state electronic density will always be lower than the energy corresponding to any other density.

The electronic Hamiltonian, $H_e$, of the system is given by:[1]

$$H_e = -\frac{\hbar^2}{2m_e}\sum_i \nabla_i^2 + \frac{1}{2}\sum_{i\neq j}\frac{e^2}{|\mathbf{r}_i - \mathbf{r}_j|} + \sum_i V_{ext}(\mathbf{r}_i); \tag{2.7}$$

the ground state energy of the system, $E_0$, written as a functional of $n_0(\mathbf{r})$, is given by:

$$E_0[n_0] \equiv \langle \Psi_0[n_0] \mid H_e \mid \Psi_0[n_0] \rangle = T_e[n_0] + E_{e-e}[n_0] + \int V_{ext}(\mathbf{r}) n_0(\mathbf{r}) d\mathbf{r}, \tag{2.8}$$

where $T_e[n_0]$ and $E_{e-e}[n_0]$ are, respectively, the kinetic energy and the energy due to interactions between the electrons in the system. The total energy in the ground state is rewritten as:

$$E_0[n_0] = F[n_0] + \int V_{ext}(\mathbf{r}) n_0(\mathbf{r}) d\mathbf{r}, \tag{2.9}$$

where $F[n_0]$ is a universal functional of the density that is the same for all electronic systems. It is system-independent and depends only on the electronic density of the system. The second term on the RHS of Eq. (2.9) is also a functional of the density, and it is system-dependent as it contains the information regarding the electron-nuclei interactions in the system, and/or any other external potential.

DFT is in principle exact, but problems arise because the true functional form of $F[n_0]$ is unknown. It is due to this inadequacy in our knowledge that approximations need to be used, making DFT approximate in its application. To deal with the functional $F[n_0]$, an *ansatz* was proposed by Kohn and Sham; this representation made it possible for the widespread and successful application of DFT to real problems.

### Kohn-Sham Formulation

The Kohn-Sham formulation allows for the mapping of a $N$-electron interacting problem onto a problem comprised of $N$ non-interacting single-electrons, with the same electronic density.[4] These $N$ electrons are assumed to occupy a set of orbital states called the Kohn-Sham states, such that each state can contain two electrons, following Pauli's exclusion principle. These fictitious states, $\psi_s(\mathbf{r})$, are related to the true ground state electronic density by:

$$n_0(\mathbf{r}) = 2\sum_{s=1}^{N/2} |\psi_s(\mathbf{r})|^2, \tag{2.10}$$

where $s$ is an index that runs over all the occupied Kohn-Sham states,[1] and the factor of 2 arises from spins.

The universal functional $F[n]$ can be split up as:

$$F[n] = T_0[n] + E_H[n] + E_{xc}[n]. \tag{2.11}$$

Each term in the above equation is described below:

1. Here, $T_0[n]$ is the kinetic energy of the fictitious non-interacting electrons. This comprises a majority of the kinetic energy of the many-electron system and is calculated using the equation:

$$T_0[n] = -2\frac{\hbar^2}{2m_e}\sum_{s=1}^{N/2}\int \psi_s^*(\mathbf{r})\nabla^2\psi_s(\mathbf{r})d\mathbf{r}. \tag{2.12}$$

2. $E_H[n]$ is the Hartree term that separates out the electron-electron Coulombic interaction from any residual energy contribution due to the exchange asymmetry and correlations. The Hartree energy, $E_H$, is given by,

$$E_H[n] = \frac{e^2}{2}\int \frac{n(\mathbf{r})n(\mathbf{r}')}{|\mathbf{r}-\mathbf{r}'|}d\mathbf{r}d\mathbf{r}'. \tag{2.13}$$

3. $E_{xc}[n]$ is the exchange-correlation energy that accounts for the kinetic energy difference between the many-electron interacting system and the $N$ single-electrons non-interacting system; and also the residual energy contributions due to the exchange asymmetry and correlations. It is given by the equation:

$$E_{xc}[n] = F[n] - (T_0[n] + E_H[n]). \tag{2.14}$$

The functional forms of $T_0[n]$ and $E_H[n]$ are known, and they can be easily calculated. The functional forms for the rest of the energy contributions, however, are not known, and are heaped into the third term, $E_{xc}[n]$. There are different working approximations for this term with varying levels of accuracy and varying computational costs; some of them are described in the next section.

On applying the Kohn-Sham representation of the universal function $F[n]$, Eq. (2.9) can be written as:

$$E_0[n_0] = T_0[n_0] + E_H[n_0] + E_{xc}[n_0] + \int V_{ext}(\mathbf{r})n_0(\mathbf{r})d\mathbf{r}, \tag{2.15}$$

$$= T_0[n_0] + \int V_{KS}(\mathbf{r})n_0(\mathbf{r})d\mathbf{r}, \tag{2.16}$$

where $V_{\mathrm{KS}}$ is the effective potential experienced by the fictitious non-interacting electrons.

Alternatively, the Kohn-Sham equations can be written as:[4]

$$\left\{-\frac{\hbar^2}{2m_e}\nabla^2 + V_{\mathrm{KS}}(\mathbf{r})\right\}\psi_s(\mathbf{r}) = E_s\psi_s(\mathbf{r}), \tag{2.17}$$

and

$$V_{\mathrm{KS}}(\mathbf{r}) = V_H(\mathbf{r}) + V_{xc}(\mathbf{r}) + V_{ext}(\mathbf{r}). \tag{2.18}$$

where $V_H(\mathbf{r}) = \frac{\delta E_H}{\delta n(\mathbf{r})}$ is the Hartree potential and $V_{xc}(\mathbf{r}) = \frac{\delta E_{xc}}{\delta n(\mathbf{r})}$ is the exchange-correlation potential.

The three equations, Eqs. (2.10), (2.17) and (2.18) can be used self-consistently to determine the true ground state electronic density and wavefunction of a system; a flowchart describing this procedure is shown in Fig. 2.1. First a trial density is considered, e.g., from a combination of atomic wavefunctions and plane waves. The Kohn-Sham potential could be calculated from Eq. (2.1); using the Kohn-Sham potential, Eq. (2.17) could be solved to determine the Kohn-Sham states. The new density $n^{\mathrm{out}}$ is obtained from these Kohn-Sham states. If the difference between input and output densities is lower than a

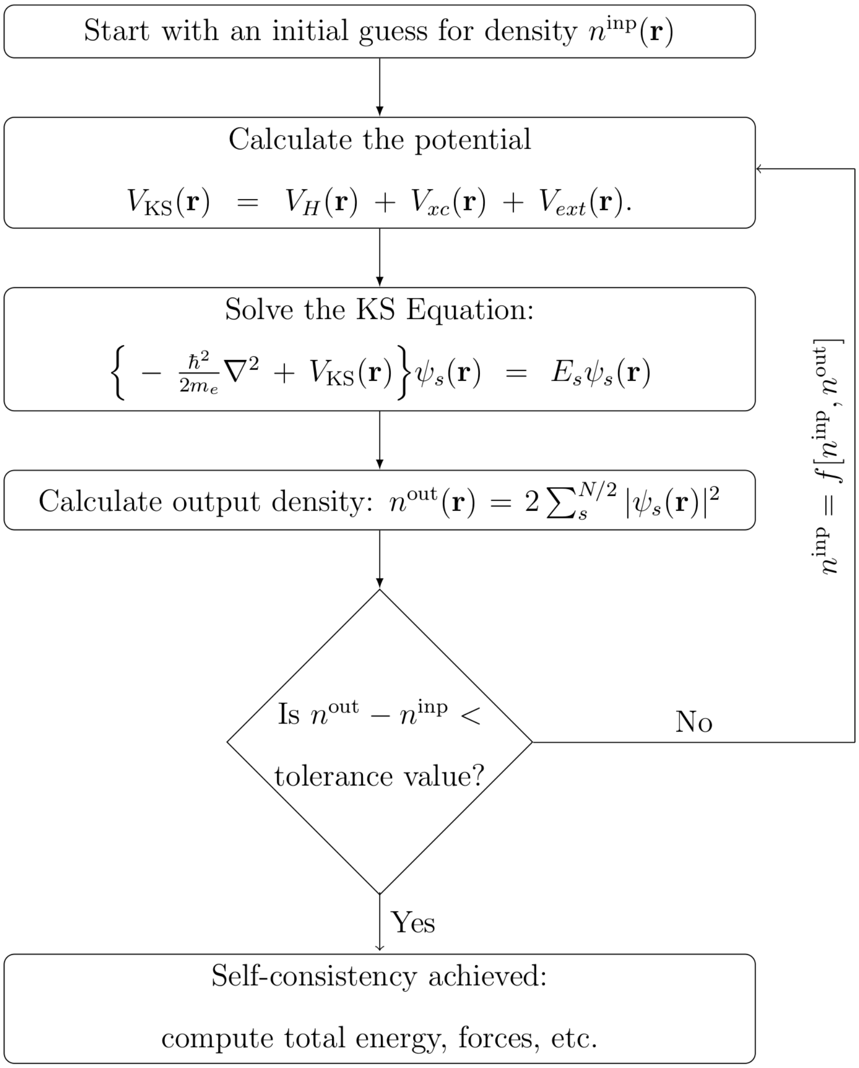

Figure 2.1: Flow chart demonstrating the self-consistency loop used to iteratively solve the Kohn-Sham equations

pre-defined tolerance, self-consistency is achieved. Otherwise the output density is used (after some mixing with the old density) as the trial density in the next iteration, and the whole procedure is repeated until convergence is achieved.

Upon achieving self-consistency, the electronic ground state energy can be calculated. To obtain the total ground state energy of the system the Coulomb interaction energy between the nuclei is added to the electronic energy.[1]

### 2.1.3 Exchange-correlation Functionals

From the Kohn-Sham equations the ground state property of any system can be obtained by self-consistent solution of single particle equations. To solve the Kohn-Sham equation we need to specify the exchange-correlation functional $E_{xc}[n]$.

The exchange energy arises because of the fact that the electrons are fermions, and the many-body wave-function is therefore antisymmetric upon the exchange of any pair of electrons. The correlation energy comes from the complicated many-body interactions between the electrons. The correlation energy is defined as the difference in energy between the exact energy and the sum of the kinetic, Hartree and exchange energies of the system. The functional form of the exchange-correlation interaction is not known, and approximations are used to treat these terms. In this thesis, we have used two forms of exchange correlation functionals. These are described below.

**Local Density Approximation**

In the Local Density Approximation (LDA) the assumption is that exchange and correlation are local in nature.[5–7] So the exchange-correlation term comes from the density of each point in space. According to this approximation, the exchange-correlation energy for a density $n(\mathbf{r})$ is given by:

$$E_{xc}^{LDA} = \int n(\mathbf{r})\epsilon_{xc}[n(\mathbf{r})]d\mathbf{r}, \tag{2.19}$$

where $\epsilon_{xc}(n)$ is the exchange-correlation energy per particle of a uniform electron gas of density $n(\mathbf{r})$. The exchange-correlation energy density is assumed to be the same as that in a homogeneous electron gas:

$$\epsilon_{xc}[n(\mathbf{r})] = \epsilon_{xc}^{\mathrm{hom}}[n(\mathbf{r})]. \tag{2.20}$$

Values of $\epsilon_{xc}^{\mathrm{hom}}[n(\mathbf{r})]$ have been obtained from Quantum Monte Carlo simulations by Ceperley and Alder,[6] which were later parametrized by Perdew and Zunger,[8] using a simple analytical form.

### Generalized Gradient Approximations

In a real system the electron density is usually not homogeneous. In order to take care of the inhomogeneous nature of the density one can consider not only the electron density but also the gradient of the density. This is known as the Generalized Gradient Approximation (GGA). The exchange correlation energy can then be written as:

$$E_{xc}^{\mathrm{GGA}} = \int d\mathbf{r}\; n(\mathbf{r})\epsilon_{xc}[n(\mathbf{r}), |\nabla n(\mathbf{r})|], \tag{2.21}$$

where $\epsilon_{xc}[n(\mathbf{r}), |\nabla n(\mathbf{r})|)$ is the exchange-correlation energy per electron, that depends on the local density $n(\mathbf{r})$ as well as the gradient of the density $|\nabla n(\mathbf{r})|$. The GGA usually corrects the over-binding effect of the LDA. However the GGA is known to often underbind. Several distinct forms of GGA functional are available. Two of the most widely used forms are the Perdew-Burke-Ernzerhof functional (PBE)[9] and the Perdew-Wang functional (PW91)[10]

## 2.1.4 Basis Sets

The Kohn-Sham orbitals are generally expanded in terms of a suitable basis set $\{\phi_j(\mathbf{r})\}$ in order to solve the Kohn-Sham equations.

$$\psi_i(\mathbf{r}) = \sum_j c_j \phi_j(\mathbf{r}). \tag{2.22}$$

A variety of basis sets can be used for this expansion such as plane waves[11;12], localized atomic orbitals[13], Muffin Tin Orbitals,[14] etc. In this thesis, we have used a plane-wave basis set which is briefly introduced below.

As electrons experience a periodic potential in an extended solid, plane waves are a natural choice of the basis set, according to Bloch's theorem.

The Kohn-Sham orbitals can then be represented as:

$$\psi_{s,\mathbf{k}}(\mathbf{r}) = \sum_{\mathbf{G}} c_{s,\mathbf{k}+\mathbf{G}} e^{i(\mathbf{k}+\mathbf{G}).\mathbf{r}}, \tag{2.23}$$

where $\mathbf{G}$ is a reciprocal lattice vector, $s$ is the band index, and $\mathbf{k}$ is a wavevector in the first Brillouin zone. This (in principle, infinite) summation is truncated by introducing a kinetic energy cutoff ($E_{\text{cut}}$) which determines the number of plane waves in the basis, so that we retain only those plane waves $e^{i(\mathbf{k}+\mathbf{G}).\mathbf{r}}$, such that $(\hbar^2/2m_e)|\mathbf{k}+\mathbf{G}|^2 \leq E_{\text{cut}}$.

One advantage of plane waves as a basis set is that the kinetic energy is a diagonal matrix in this representation. Another advantage is that the convergence of the basis set is controlled by a single parameter $E_{\text{cut}}$. However, if one tries to expand the wavefunctions in the core region using plane waves, one needs a huge number of plane waves, resulting in a high computational cost. This problem is resolved by the use of pseudopotentials, which are described below.

### 2.1.5 Pseudopotential Approximation

This approximation is based on the fact that generally the valence electrons determine the chemical bonding and material properties. The core electrons are tightly bound to the nucleus and highly localized in nature. In all-electron plane wave DFT calculations a large number of plane waves is required to describe the core electrons accurately, leading to a high plane-wave cutoff. Also due to the orthogonality condition valence wavefunctions have several oscillations in the core region which again leads to a high plane-wave cutoff.

To get rid of this problem we introduce the pseudopotential approximation.[15]. Here the potential is formed in such a way that the core orbitals are neglected completely, but at the same time treating the interaction between the valence electrons and the ionic core with sufficient accuracy, yet requiring a low cutoff. The pseudopotential is constructed in such a way that in the valence region the pseudo-wavefunction matches exactly with the true wavefunction. In the core region the pseudo-wavefunction is nodeless and goes smoothly to zero, therefore requiring a low cutoff.

There are certain conditions obeyed by a good pseudopotential. First the pseudo-wavefunction and its first and second derivatives should match smoothly at the core radius cutoff. Secondly it should require a low plane wave cutoff. It was initially believed that one should conserve electronic charge, i.e., the square amplitude of wavefunctions of the real and pseudo wavefunctions are identical, in both the core and valence regions.[16] This is known as "norm-conserving". The success of a pseudopotential lies in its transferability to different chemical environments. Generally norm-conserving psedopotentials show good transferability.

The pseudopotential approximation drastically reduces the computational expense. However, norm-conserving pseudopotentials still need a large number of plane waves, especially for those cases where the valence wavefunction is nodeless, such as for elements in the first row of the periodic table. In "ultrasoft pseudopotentials", the condition of norm-conserving is relaxed and the computational cost is reduced further.[17] The loss of charge due to the relaxing of norm-conserving condition is compensated for by adding an "augmentation charge" in the core region of the pseudopotential. In ultrasoft pseudopotentials a separate cutoff for charge density is used in addition to kinetic energy cutoff. The required charge density cutoff is typically 8 to 12 times the cutoff for the wavefunction.

### 2.1.6 k-point Sampling and Smearing

Any observable of the wave-function is obtained by integrating over all the wavevectors in the first Brillouin zone (BZ). Integrating over all **k**-points leads to huge computational cost. In practice, this is replaced by a finite mesh of **k**-points. The most commonly used **k**-point sampling method is a Monkhorst-Pack grid [18] where the grid is generated using the formula

$$\mathbf{k}_{n_1,n_2,n_3} = \sum_{\beta=1}^{3} \frac{2n_\beta - N_\beta - 1}{2N_\beta}\mathbf{b}_\beta, \qquad (n_\beta = 1, 2, 3, \ldots, N_\beta) \tag{2.24}$$

where $N_\beta$ is the number of divisions in reciprocal space along the $\beta$th direction ($\beta$ = 1, 2, 3) and $\mathbf{b}_1, \mathbf{b}_2$ and $\mathbf{b}_3$ are the primitive reciprocal lattice vectors.

As the number of **k**-points increases, the accuracy of the calculation also increases and the computational cost also goes up. So, symmetries of the system are used to reduce the Brillouin zone to the irreducible Brillouin zone (IBZ). In the case of isolated systems or very large supercells, it would be enough if the **k** space is sampled only at the Brillouin zone origin $\mathbf{k} = (0, 0, 0)$, also known as the $\Gamma$ point.

In metals, the Fermi surface separates the occupied region from the unoccupied region in **k** space. In the case of metals, at $T = 0$ there is a sharp discontinuity in **k** space on going from occupied states to the unoccupied states. This requires a large number of **k**-points in order to reproduce the Fermi surface accurately. Using the smearing technique, one can replace the step function with a smoothly varying function for the occupation of states near the Fermi energy. As a result fewer **k**-points are required. Some of the existing smearing techniques are Gaussian smearing,[19] Methfessel-Paxton smearing,[20] and Marzari-Vanderbilt smearing.[21]. The larger the smearing, the better is the convergence with respect to **k** points, but the lower is the accuracy.

### 2.1.7 Dispersion Interactions: The DFT-D2 Method

The interaction between charge fluctuations in one part of the system with the rest of the system is the source of the London dispersion interaction. This interaction is attractive, long range and non-local in nature[24;25]. Local and semilocal functionals (e.g., LDA, GGA) fail to incorporate dispersion interactions. Several methods have developed in recent years to include this interaction into DFT calculations. Among them the "DFT-D2" treatment of Grimme gives a fairly accurate treatment of London dispersion interactions at relatively low computational cost,[26] and is used in this thesis.

The dispersion corrected total energy is given as:

$$E_{\text{DFT-D2}} = E_{\text{DFT}} + E_{disp}, \tag{2.25}$$

where $E_{\mathrm{DFT}}$ is the total energy from DFT calculations and $E_{disp}$ is the dispersion correction which is given by:

$$E_{disp} = -s_6 \sum_{I=1}^{N_{at}-1} \sum_{J=I+1}^{N_{at}} \frac{C_6^{IJ}}{R_{IJ}^6} f_{damp}(R_{IJ}), \tag{2.26}$$

where $N_{at}$ is the number of atoms in the system, $C_6^{IJ}$ denotes the dispersion coefficient for a pair of atoms $I$ and $J$,

$$C_6^{IJ} = \sqrt{C_6^I C_6^J}, \tag{2.27}$$

$s_6$ is a global scaling factor that depends only on the approximate functional used, and $R_{IJ}$ is the interatomic distance between the atoms $I$ and $J$. $f_{damp}(R_{IJ})$ is a damping function used to avoid singularity at small $R_{IJ}$, given as:

$$f_{damp}(R_{IJ}) = \frac{1}{1 + e^{-d(\frac{R_{IJ}}{R_r}-1)}}, \tag{2.28}$$

where $R_r$ is the sum of atomic van der Waals radii,[27] and $d$ is a damping parameter with a typical value of 20.[26]

### 2.1.8 Spin-Polarized Density Functional Theory

For spin-polarized DFT, the total electron density can be separated into spin up and spin down electron densities. The spin-polarized electron densities are given by

$$n^\sigma(\mathbf{r}) = \sum_{s=1}^{N^\sigma} \psi_s^{\sigma *}(\mathbf{r}) \psi_s^\sigma(\mathbf{r}), \tag{2.29}$$

where $\sigma = \{\uparrow, \downarrow\}$ is the spin of the electron, and $N^\sigma$ is the number of orbitals of spin $\sigma$. The total electronic density of the spin-polarized system is the sum of the spin up and spin down electronic densities: $n(\mathbf{r}) = n^\uparrow(\mathbf{r}) + n^\downarrow(\mathbf{r})$. The magnetic moment of the spin polarized system is given by: $m(\mathbf{r}) = n^{\uparrow}(\mathbf{r}) - n^{\downarrow}(\mathbf{r})$. Note that the direction of magnetization is nominal, as we are considering collinear magnetic calculations and no spin-orbit interactions are present.

The Kohn-Sham equations for spin-polarized calculations are given by

$$\left\{-\frac{\hbar^2}{2m_e}\nabla^2 + V^{\sigma}_{\mathrm{KS}}(\mathbf{r})\right\}\psi^{\sigma}_s(\mathbf{r}) = \epsilon^{\sigma}_s\,\psi^{\sigma}_s(\mathbf{r}), \tag{2.30}$$

where $V^{\sigma}_{\mathrm{KS}}$ is the Kohn-Sham potential, which is given by:

$$V^{\sigma}_{\mathrm{KS}}(\mathbf{r}) = V_{ext}(\mathbf{r}) + V_H(\mathbf{r}) + V^{\sigma}_{xc}(\mathbf{r}), \tag{2.31}$$

The spin dependence arises only from the exchange-correlation potential. The exchange-correlation potential can be defined as

$$V^{\sigma}_{xc}(\mathbf{r}) = \frac{\delta E_{xc}[n(\mathbf{r}), m(\mathbf{r})]}{\delta n^{\sigma}(\mathbf{r})}, \tag{2.32}$$

For spin-polarized systems all the equations mentioned above are solved in a similar manner to the non-spin-polarized Kohn-Sham equations.

## 2.2 Calculation of Forces and Stresses

In order to determine the optimized geometry of the system, the forces and stresses in the system need to be minimized.

The force on each ion $I$ is equal to the first derivative of the total energy with respect to the ionic position $R_I$. According to the Hellmann-Feynman theorem,[22] this force is the expectation value of the derivative of the Hamiltonian.

$$\mathbf{F_I} = -\frac{\partial E(\mathbf{R}_I)}{\partial \mathbf{R}_I} = -\langle \psi | \frac{\partial \hat{H}}{\partial \mathbf{R}_I} | \psi \rangle \tag{2.33}$$

where $E(\mathbf{R_I})$ is the total energy for a given set of nuclear co-ordinates $\{\mathbf{R}_I\}$ and $\psi$ is the eigenfunction of the Hamiltonian $\hat{H}$. By moving the atoms using some minimization technique the force can be used to find the ground state coordinates of the system.

Stresses can be calculated from the derivative of the total energy $E_{tot}$ with respect to the strain. According to the Nielsen and Martin theorem,[23] stress is the the expectation value of the derivative of the Hamiltonian with respect to the strain:

$$\sigma_{\alpha\beta} = -\frac{1}{\Omega}\frac{\partial E}{\partial \epsilon_{\alpha\beta}} = -\frac{1}{\Omega}\langle \psi | \frac{\partial \hat{H}}{\partial \epsilon_{\alpha\beta}} | \psi \rangle, \tag{2.34}$$

where $\epsilon_{\alpha\beta}$ is the strain and $\Omega$ is the volume of the system.

## 2.3 Wannier Functions and Model Hamiltonians

The description of materials in terms of localized orbitals not only simplifies computations in many cases, but can provide better insights. While the molecular orbitals used by chemists may be difficult to understand for physicists who talk about “Bloch waves”, similarly the transformation from a description in terms of a set of isolated atoms with localized orbitals to periodic solids with extended Bloch states may be difficult to understand for chemists. Wannier functions provide a natural extension from atomic orbitals to solids. The Wannier function of an isolated band is defined as

$$w_n(\mathbf{r} - \mathbf{R}) = \frac{V}{(2\pi)^d} \int_{BZ} d\mathbf{k} e^{-i\mathbf{k}.\mathbf{R}} \psi_{n,\mathbf{k}}(\mathbf{r}), \tag{2.35}$$

where $V$ is the unit cell volume, $d$ is the number of spatial dimensions and $\psi_{n,\mathbf{k}}(\mathbf{r})$ are the Bloch functions corresponding to the $n^{th}$ band, and the integration is over the first Brillouin zone. The inverse transformation can be expressed as

$$\psi_{n,\mathbf{k}}(\mathbf{r}) = \sum_{R} e^{-i\mathbf{k}.\mathbf{R}} w_n(\mathbf{r}-\mathbf{R}). \tag{2.36}$$

In Eq. (2.35) the definition of the Wannier function is not unique since the phase associated with the Bloch function is arbitrary. A particular choice of phase is called a gauge and the transformation between different gauges is called a gauge transformation.

In the case of entangled bands, i.e., where the bands cannot be isolated, there are two possible methods for the construction of Wannier functions: (a) the projection method and (b) the Marzari and Vanderbilt maximally localized Wannier function construction method. In both these methods one starts from the known eigenstates of the Hamiltonian of the Bloch function and performs unitary transformations according to Eq. (2.35).

### 2.3.1 Projection method

The construction of Wannier functions via the projection method is simple yet effective. Here one starts from $J$ localized trial orbitals $g_n(\mathbf{r})$ corresponding to some initial guess for the Wannier function. These trial orbitals are projected onto Bloch functions to obtain

$$|\phi_{n,\mathbf{k}}(\mathbf{r})\rangle = \sum_{n=1}^{J} |\psi_{n,\mathbf{k}}(\mathbf{r})\rangle \langle \psi_{n,\mathbf{k}}|g_n\rangle. \tag{2.37}$$

The overlap matrix $(S_k)_{mn}$ is then computed using the formula

$$(S_k)_{mn} = \langle \psi_{m,\mathbf{k}}|\phi_{m,\mathbf{k}}\rangle. \tag{2.38}$$

The Eq. (2.38) is then used to construct Löwdin-orthonormalized Bloch-like states

$$|\tilde{\psi}_{n,\mathbf{k}}(\mathbf{r})\rangle = \sum_{m=1}^{J} |\phi_{n,\mathbf{k}}(\mathbf{r})\rangle (S_k^{-1/2})_{mn} \tag{2.39}$$

These $|\tilde{\psi}_{n,\mathbf{k}}(\mathbf{r})\rangle$ when substituted in Eq. (2.35) in place of $|\psi_{n,\mathbf{k}}(\mathbf{r})\rangle$ result in a well localized Wannier function. Because any arbitrary rotation among the $|\psi_{n,\mathbf{k}}(\mathbf{r})\rangle$ cancels out exactly, the outcome of Eq. (2.37) is not affected by any gauge transformation and thus is uniquely defined. The method is successful as long as the inner product matrix $A_k = \langle \psi_{n,\mathbf{k}} | g_n \rangle$ is not singular.

### 2.3.2 Maximally localized Wannier functions

In this method the localization is defined to minimize the spread functional

$$\Omega = \sum_n \langle r^2 \rangle_n - \langle \mathbf{r} \rangle_n^2, \tag{2.40}$$

where $n$ is the Wannier function index, $\langle \mathbf{r} \rangle_n$ is the position of the center of the $n^{th}$ Wannier function and $\langle r^2 \rangle_n$ is the $r^2$ matrix element. The spread depends neither on the coordinate origin, nor on the choice of lattice site. The spread functional can be divided into a gauge independent part $\Omega_I$ and a gauge dependent part $\tilde{\Omega}$. The gauge independent part $\Omega_I$ can be expressed as

$$\Omega_I = \sum_n \langle r^2 \rangle_n - \sum_{\mathbf{R},n,m} |\langle \mathbf{R}, m | \mathbf{r} | 0, n \rangle|^2, \tag{2.41}$$

and the gauge dependent part $\tilde{\Omega}$ can be expressed as

$$\tilde{\Omega} = \sum_n \sum_{\mathbf{R},m} |\langle \mathbf{R}, m | \mathbf{r} | 0, n \rangle|^2. \tag{2.42}$$

The minimization of $\Omega$ thus corresponds to the minimization of the gauge independent part $\Omega_I$ only.

## 2.4 Phonon Calculations: Density Functional Perturbation Theory

Different physical properties of solids such as the resistivity of metals and superconductivity, largely depend on the lattice-dynamical behavior. With the development of DFT it is possible to obtain accurate phonon dispersions on a fine grid of wave vectors covering the entire Brillouin zone (BZ) using linear response theory of lattice vibrations, also known as the density functional perturbation theory (DFPT).[31–33]

### 2.4.1 Lattice Dynamics from Electronic-Structure Theory

We can decouple the the vibrational degrees of freedom from the electronic degrees of freedom according to the adiabatic approximation (see Section 2.1.1). The lattice-dynamical properties of a system can then be determined by the eigenvalues $\varepsilon$ and the eigenfunctions $\chi$ of the Schrödinger equation:

$$\left[-\sum_I \frac{\hbar^2}{2M_I}\nabla_I^2 + E(\mathbf{R})\right]\chi(\mathbf{R}) = \varepsilon\chi(\mathbf{R}). \tag{2.43}$$

where $\mathbf{R}_I$ is the coordinate of the $I$th nucleus, $M_I$ its mass and $E(\mathbf{R})$ is the Born-Oppenheimer potential energy surface.

The equilibrium geometry is found by equating the Hellman-Feynman forces to zero, $\mathbf{F}_I = -\frac{\partial E(\mathbf{R})}{\partial \mathbf{R}_I} = 0$. The vibrational frequencies $\omega$ corresponding to this geometry are found by determining the eigenvalues of the Hessian of the Born-Oppenheimer energy, scaled by nuclear masses:

$$\det\left[\frac{1}{\sqrt{M_I M_J}}\frac{\partial^2 E(\mathbf{R})}{\partial \mathbf{R}_I \partial \mathbf{R}_J} - \omega^2\right] = 0. \tag{2.44}$$

The Hessian of the Born-Oppenheimer energy surface appearing in Eq. (2.44) is obtained by differentiating the Hellman-Feynman forces with respect to nuclear coordinates:

$$\frac{\partial^2 E(\mathbf{R})}{\partial \mathbf{R}_I \partial \mathbf{R}_J} = -\frac{\partial \mathbf{F}_I}{\partial \mathbf{R}_J}, \tag{2.45}$$

where the Hellmann-Feynman forces are given as:

$$\mathbf{F}_I = -\int n_{\mathbf{R}}(\mathbf{r})\frac{\partial V_{\mathbf{R}}(\mathbf{r})}{\partial \mathbf{R}_I} d\mathbf{r} - \frac{\partial E_N(\mathbf{R})}{\partial \mathbf{R}_I}, \tag{2.46}$$

where $E_N(\mathbf{R})$ is the electrostatic interaction between different nuclei. Calculation of

Eq. (2.45) involves finding the ground-state electronic charge density $n_{\mathbf{R}}(\mathbf{r})$ as well as its linear response to a distortion of the nuclear geometry, $\partial n_{\mathbf{R}}(\mathbf{r})/\partial \mathbf{R}_I$. This is shown in the next section.

### 2.4.2 Linear Response

The electron-density response $\partial n_{\mathbf{R}}(\mathbf{r})/\partial \mathbf{R}_I$, needed to determine the matrix of interatomic force constants, can be evaluated by linearizing the one-electron KS equations, charge density and the effective potential, with respect to the wave function, density and potential variations, respectively.

Linearizing the charge density leads us to:

$$\Delta n(\mathbf{r}) = 4\,\mathrm{Re}\sum_{n=1}^{N/2} \psi_n^*(\mathbf{r})\Delta\psi_n(\mathbf{r}), \tag{2.47}$$

where $\Delta$ is the finite-difference operator. The variation of Kohn-Sham orbitals, $\Delta\psi_n(\mathbf{r})$, is obtained by first-order perturbation theory as follows:

$$(H_{SCF} - \epsilon_n)|\Delta\psi_n\rangle = -(\Delta V_{SCF} - \Delta\epsilon_n)|\psi_n\rangle, \tag{2.48}$$

where $H_{SCF}$ is the unperturbed KS Hamiltonian and $\Delta\epsilon_n = \langle\psi_n|\Delta V_{SCF}|\psi_n\rangle$ is the first-order variation of KS eigenvalues $\epsilon_n$. The first-order correction to the self-consistent potential is given by

$$\Delta V_{SCF}(\mathbf{r}) = \Delta V(\mathbf{r}) + e^2 \int \frac{\Delta n(\mathbf{r}')}{|\mathbf{r}-\mathbf{r}'|} d\mathbf{r}' + \frac{dv_{xc}(n)}{dn}\Big|_{n=n(\mathbf{r})} \Delta n(\mathbf{r}). \tag{2.49}$$

Equations (2.47) – (2.49) form a set of self-consistent equations for the perturbed system completely analogous to the KS equations in the unperturbed case, with the KS eigenvalue equation being replaced by the solution of a linear system, given by Eq. (2.48). Note that $\Delta V_{SCF}(\mathbf{r})$ is a linear functional of $\Delta n(\mathbf{r})$, which in turn depends linearly on the $\Delta\psi$'s, casting the whole self-consistent calculation in terms of a generalized linear problem.

The advantage of DFPT over other nonperturbative methods for calculating the vibrational properties (such as the frozen-phonon method, where the total energies are calculated for a series of displaced atomic positions, and numerical differences are then computed), is that the responses to perturbations of different wavelengths are decoupled. This feature allows one to calculate phonon frequencies at arbitrary wave vector **q**, avoiding the use of supercells and with a computational load independent of phonon wavelength.

## 2.5 Electron-phonon coupling

The electron-phonon coupling can be calculated using different approaches such as frozen-phonon approach,[28–30]density functional perturbation theory approach,[31–33] and by using Born-Oppenheimer molecular dynamics (BOMD).[34;35] To calculate the electron-phonon coupling we have used the frozen phonon method, using which we can estimate the strength of the coupling corresponding to particular phonon modes. In this approach, the change in a property of interest caused by a specific phonon mode is calculated by performing calculations for two or more sets of atomic coordinates, one set corresponding to the perfect crystal (i.e., the equilibrium coordinates) and another set for coordinates corresponding to the crystal with a specific set of displacements according to the relevant phonon eigenvectors. The electron-phonon interaction Hamiltonian can be expressed as a Taylor series expansion of the electronic potential:

$$\Delta V^{\nu}(\mathbf{r},\mathbf{R}) = \sum_{I} \frac{\partial V}{\partial \mathbf{R}_I} \cdot \mathbf{u}_I^{\nu}, \tag{2.50}$$

where $V$ is the electronic potential, $\mathbf{R}_I$ denotes the nuclear position of atom $I$ and the vibrational eigenmode $\nu$. The dispalacement vector $\mathbf{u}_I^{\nu}$ of atom $I$ and vibrational eigenmode $\nu$ can be expressed in terms of normal mode coordinates as

$$\mathbf{u}_I^{\nu} = \frac{1}{\sqrt{M_I}} Q^{\nu} \mathbf{X}_I^{\nu}, \tag{2.51}$$

where

$$Q^{\nu} = \sqrt{\frac{\hbar}{2\omega^{\nu}}}(a_{\nu}^{\dagger} + a_{\nu}). \tag{2.52}$$

Here $M_I$ is the mass of the atom $I$, $\hbar$ is the reduced Planck's constant and $\omega^{\nu}$ is the frequency of the vibrational mode $\nu$. $\mathbf{X}_I^{\nu}$ are the three components of the vibrational eigenmode and $a_{\nu}^{\dagger}$ and $a_{\nu}$ are the creation and annihilation operators of the $\nu$-phonon mode.

According to Eq. (2.50) and Eq. (2.51), the electron-phonon coupling matrix element has the form

$$g^{\nu}(m,n) = \sum_I \sqrt{\frac{\hbar}{2M_I\omega^{\nu}}}\langle\psi_m, I^{\nu}|\frac{\partial V}{\partial \mathbf{R_I}} \cdot \mathbf{X}_I^{\nu}(a_{\nu}^{\dagger} + a_{\nu})|\psi_n\rangle. \tag{2.53}$$

According to the frozen phonon approach for the electron-phonon coupling, the change in potential caused by a phonon distortion in Eq. (2.53) is replaced by

$$\sum_I \frac{\partial V}{\partial \mathbf{R_I}} \cdot \mathbf{X}_I^{\nu} = \frac{V_{\mathrm{scf}}^{\nu}(\mathbf{r}) - \mathbf{V}_{\mathrm{scf}}^{\mathbf{0}}(\mathbf{r})}{u^{\nu}}, \tag{2.54}$$

where $u^{\nu} = \sqrt{\sum_I \frac{1}{M_I}\mathbf{X}_I^{\nu 2}}$ is the frozen phonon displacement caused by the lattice vibrations.

## 2.6 First principles molecular dynamics

### 2.6.1 Verlet algorithm and Velocity Verlet algorithm

For an initial set of ionic coordinates molecular dynamics (MD) provides local configurational space. Different thermodynamic properties can be obtained by time averaging statistical quantities after performing a molecular dynamics simulation.

According to classical molecular dynamics the particle trajectories can be determined from the instantaneous force acting on them. The force can be calculated from the Hellmann-Feynman theorem.[22] Newton's equation of motion is:

$$M_I\ddot{\mathbf{R}}_I = -\frac{\partial E(\mathbf{R}_I)}{\partial \mathbf{R}_I} = \mathbf{F}_I. \tag{2.55}$$

The Eq. (2.55) is discretized and integrated in time to obtain trajectories. There are several numerical algorithms available for integrating the equation of motion. The Verlet algorithm is one of the simplest algorithms. At any instant of time $t$, the position of the particle can be expanded as

$$\mathbf{R}_I(t+\Delta t) = \mathbf{R}_I(t) + \mathbf{v}_I(t)\Delta t + \frac{1}{2}\mathbf{a}_I(t)\Delta t^2 + ... \tag{2.56}$$

where $\mathbf{R}_I$, $\mathbf{v}_I$ and $\mathbf{a}_I$ are the position, velocity and acceleration, respectively.

By summing over the equations for $\mathbf{R}_I(t+\Delta t)$ and $\mathbf{R}_I(t-\Delta t)$ we obtain

$$\mathbf{R}_I(t+\Delta t) = 2\mathbf{R}_I(t) - \mathbf{R}_I(t-\Delta t) + \mathbf{a}_I(t)\Delta t^2, \tag{2.57}$$

where the error in the estimate of the new position is $\mathcal{O}(\Delta t^4)$. $\Delta t$ is the time step chosen for the molecular dynamics. The Verlet algorithm does not use velocities to compute the new position, which is computed using

$$\mathbf{v}(t) = \frac{\mathbf{R}_I(t+\Delta t) + \mathbf{R}_I(t-\Delta t)}{2\Delta t} + \mathcal{O}(\Delta t^2). \tag{2.58}$$

The advantages of the Verlet algorithm are that it is fast, memory efficient and numerical integration errors are of the order $\mathcal{O}(\Delta t^4)$. But the algorithm is not self-starting, i.e., we need an initialization step for $\mathbf{R}_I(t-\Delta t)$. A more commonly used algorithm is the Velocity Verlet algorithm. Here the ionic velocities are used together with forces to compute the trajectories. In this algorithm velocities and positions are propagated independently. According to this algorithm, the position and velocity of the particle at any instant of $t$ can be expanded as

$$\mathbf{R}_I(t+\Delta t) = \mathbf{R}_I(t) + \mathbf{v}_I(t)\Delta t + \frac{(\Delta t)^2}{2M_I}F_I(t) \tag{2.59}$$

$$\mathbf{v}_I(t+\Delta t) = \mathbf{v}_I(t) + \frac{(\Delta t)^2}{2M_I}[F_I(t+\Delta t) + F_I(t)] \tag{2.60}$$

The timestep should be sufficiently small to ensure that the force on each ion over a timestep $\Delta t$ is a good approximation to the real force.

### 2.6.2 Born-Oppenheimer molecular dynamics

In Born-Oppenheimer molecular dynamics the ions are considered as classical particles. Also the Born-Oppenheimer or adiabatic approximation is taken into consideration, i.e., the nuclei can be considered as effectively stationary in electronic time scales. So the force can be calculated using the formula

$$\mathbf{F_I} = -\frac{\partial E(\mathbf{R}_I)}{\partial \mathbf{R}_I} = -\langle \psi | \frac{\hat{H}}{\partial \mathbf{R}_I} | \psi \rangle, \tag{2.61}$$

where $\psi$ is the eigenfunction of the Hamiltonian $\hat{H}$. If we assume that $V_{ext}$ is local, then Eq. (2.61) can be expressed as

$$-\langle \psi | \frac{\partial \hat{H}}{\partial \mathbf{R}_I} | \psi \rangle = -\int \frac{\partial \mathbf{V}_{ext}}{\partial \mathbf{R}_I} n(\mathbf{r}) d\mathbf{r}. \tag{2.62}$$

The three equations, Eqs. (2.55), (2.61) and (2.62 ) represent the complete set of equations determining the Born-Oppenheimer molecular dynamics. At each timestep self-consistent minimization is performed to obtain the proper electron density.

### 2.6.3 Car-Parrinello molecular dynamics

Born-Oppenheimer molecular dynamics is computationally expensive as self-consistent solution of the Kohn-Sham equations at every time step is required. Car-Parrinello molecular dynamics (CPMD) is a method where ions propagate and one finds the electronic ground state simultaneously, thus dramatically reducing the calculation time. In CPMD, electronic wavefunctions are treated as independent classical dynamic variables. The total energy can then be represented as $E \equiv E^{CP}[\mathbf{R}, \psi_j]$. The classical Lagrangian of the Car-Parrinello system is given by

$$\mathcal{L}^{\mathrm{CP}} = \frac{1}{2}\sum_j \mu \langle \dot{\psi}_j | \dot{\psi}_j \rangle + \frac{1}{2}\sum_I M_I \dot{\mathbf{R}}_I^2 - E^{\mathrm{CP}}[\mathbf{R}, \psi_j] + \sum_{jk} \Lambda_{jk}[\langle \psi_j | \psi_j \rangle - \delta_{jk}], \tag{2.63}$$

where $\mu$ is the fictitious mass corresponding to the wavefunction $\psi_j$. The first term on the right-hand-side (RHS) is the kinetic energy corresponding to the fictitious mass $\mu$. The last term arises from the orthonormality constraint on the wavefunction.

Corresponding to Eq. (2.64), the Euler-Lagrange equations of motion will be

$$\mu \ddot{\psi}_j = -\frac{\delta E^{\mathrm{CP}}}{\delta \psi_j} + \sum_k \Lambda_{jk} \psi_k \tag{2.64}$$

$$M_I \ddot{\mathbf{R}}_{\mathbf{I}} = -\frac{\partial E^{\mathrm{CP}}}{\partial \mathbf{R}_I} \tag{2.65}$$

The functional derivative $-\frac{\delta E^{\mathrm{CP}}}{\delta \psi_j}$ can be expressed as a Kohn-Sham Hamiltonian as defined in Eq. (2.17). Minimizing the energy functional $E \equiv E^{CP}[\mathbf{R}, \psi_j]$ with respect to $\psi_j$ results in ion dynamics which matches with the physical system.

# Bibliography

[1] R. M. Martin and R. M. Martin, *Electronic structure: basic theory and practical methods.* Cambridge university press, 2004.

[2] M. Born and R. Oppenheimer, “Zur quantentheorie der molekeln,” *Annalen der physik*, vol. 389, no. 20, pp. 457–484, 1927.

[3] P. Hohenberg and W. Kohn, “Inhomogeneous electron gas,” *Physical review*, vol. 136, no. 3B, p. B864, 1964.

[4] W. Kohn and L. J. Sham, “Self-consistent equations including exchange and correlation effects,” *Physical review*, vol. 140, no. 4A, p. A1133, 1965.

[5] R. O. Jones and O. Gunnarsson, “The density functional formalism, its applications and prospects,” *Reviews of Modern Physics*, vol. 61, no. 3, p. 689, 1989.

[6] D. M. Ceperley and B. Alder, “Ground state of the electron gas by a stochastic method,” *Physical Review Letters*, vol. 45, no. 7, p. 566, 1980.

[7] S. H. Vosko, L. Wilk, and M. Nusair, “Accurate spin-dependent electron liquid correlation energies for local spin density calculations: a critical analysis,” *Canadian Journal of physics*, vol. 58, no. 8, pp. 1200–1211, 1980.

[8] J. P. Perdew and A. Zunger, “Self-interaction correction to density-functional approximations for many-electron systems,” *Physical Review B*, vol. 23, no. 10, p. 5048, 1981.

[9] J. P. Perdew, K. Burke, and M. Ernzerhof, “Generalized gradient approximation made simple,” *Physical review letters*, vol. 77, no. 18, p. 3865, 1996.

[10] J. P. Perdew and Y. Wang, “Pair-distribution function and its coupling-constant average for the spin-polarized electron gas,” *Physical Review B*, vol. 46, no. 20, p. 12947, 1992.

[11] P. Giannozzi, S. Baroni, N. Bonini, M. Calandra, R. Car, C. Cavazzoni, D. Ceresoli, G. L. Chiarotti, M. Cococcioni, I. Dabo, *et al.*, “Quantum espresso: a modular and open-source software project for quantum simulations of materials,” *Journal of physics: Condensed matter*, vol. 21, no. 39, p. 395502, 2009.

[12] X. Gonze, J.-M. Beuken, R. Caracas, F. Detraux, M. Fuchs, G.-M. Rignanese, L. Sindic, M. Verstraete, G. Zerah, F. Jollet, *et al.*, “First-principles computation of material properties: the abinit software project,” *Computational Materials Science*, vol. 25, no. 3, pp. 478–492, 2002.

[13] J. M. Soler, E. Artacho, J. D. Gale, A. García, J. Junquera, P. Ordejón, and D. Sánchez-Portal, "The siesta method for ab initio order-n materials simulation," *Journal of Physics: Condensed Matter*, vol. 14, no. 11, p. 2745, 2002.

[14] H. Dreyssé, *Electronic structure and physical properties of solids.* Springer, 2000.

[15] W. E. Pickett, "Pseudopotential methods in condensed matter applications," *Computer Physics Reports*, vol. 9, no. 3, pp. 115–197, 1989.

[16] D. Hamann, M. Schlüter, and C. Chiang, "Norm-conserving pseudopotentials," *Physical Review Letters*, vol. 43, no. 20, p. 1494, 1979.

[17] D. Vanderbilt, "Soft self-consistent pseudopotentials in a generalized eigenvalue formalism," *Physical review B*, vol. 41, no. 11, p. 7892, 1990.

[18] H. J. Monkhorst and J. D. Pack, "Special points for brillouin-zone integrations," *Physical review B*, vol. 13, no. 12, p. 5188, 1976.

[19] C.-L. Fu and K.-M. Ho, "First-principles calculation of the equilibrium ground-state properties of transition metals: Applications to Nb and Mo," *Physical Review B*, vol. 28, no. 10, p. 5480, 1983.

[20] M. Methfessel and A. Paxton, "High-precision sampling for Brillouin-zone integration in metals," *Physical Review B*, vol. 40, no. 6, p. 3616, 1989.

[21] N. Marzari, D. Vanderbilt, A. De Vita, and M. Payne, "Thermal contraction and disordering of the al (110) surface," *Physical review letters*, vol. 82, no. 16, p. 3296, 1999.

[22] R. P. Feynman, "Forces in molecules," *Physical Review*, vol. 56, no. 4, p. 340, 1939.

[23] O. Nielsen and R. M. Martin, "First-principles calculation of stress," *Physical Review Letters*, vol. 50, no. 9, p. 697, 1983.

[24] O. A. Vydrov and T. Van Voorhis, "Nonlocal van der waals density functional made simple," *Physical review letters*, vol. 103, no. 6, p. 063004, 2009.

[25] M. Dion, H. Rydberg, E. Schröder, D. C. Langreth, and B. I. Lundqvist, “Van der waals density functional for general geometries,” *Physical review letters*, vol. 92, no. 24, p. 246401, 2004.

[26] S. Grimme, “Semiempirical GGA-type density functional constructed with a long-range dispersion correction,” *Journal of computational chemistry*, vol. 27, no. 15, pp. 1787–1799, 2006.

[27] S. Grimme, “Accurate description of van der waals complexes by density functional theory including empirical corrections,” *Journal of computational chemistry*, vol. 25, no. 12, pp. 1463–1473, 2004.

[28] M. M. Dacorogna, M. L. Cohen, and P. K. Lam, “Self-consistent calculation of the q dependence of the electron-phonon coupling in aluminum,” *Physical review letters*, vol. 55, no. 8, p. 837, 1985.

[29] P. K. Lam, M. M. Dacorogna, and M. L. Cohen, “Self-consistent calculation of electron-phonon couplings,” *Physical Review B*, vol. 34, no. 8, p. 5065, 1986.

[30] K.-J. Chang and M. L. Cohen, “Electron-phonon interactions and superconductivity in Si, Ge, and Sn,” *Physical Review B*, vol. 34, no. 7, p. 4552, 1986.

[31] S. Y. Savrasov, D. Y. Savrasov, and O. Andersen, “Linear-response calculations of electron-phonon interactions,” *Physical review letters*, vol. 72, no. 3, p. 372, 1994.

[32] F. Mauri, O. Zakharov, S. de Gironcoli, S. G. Louie, and M. L. Cohen, “Phonon softening and superconductivity in tellurium under pressure,” *Physical review letters*, vol. 77, no. 6, p. 1151, 1996.

[33] A. Y. Liu and A. A. Quong, “Linear-response calculation of electron-phonon coupling parameters,” *Physical Review B*, vol. 53, no. 12, p. R7575, 1996.

[34] J. Gavartin and A. Shluger, “Ab initio modeling of electron-phonon coupling in high-k dielectrics,” *physica status solidi c*, vol. 3, no. 10, pp. 3382–3385, 2006.

[35] D. M. Ramo, A. Shluger, J. Gavartin, and G. Bersuker, “Theoretical prediction of intrinsic self-trapping of electrons and holes in monoclinic $HfO_2$,” *Physical review letters*, vol. 99, no. 15, p. 155504, 2007.

Chapter 3

# Tuning the Binding of Methanol on C-BN and BCN Systems

## 3.1 Introduction

Recently, there has been increased interest in the scientific study of weak binding of molecules on substrates. This is relevant for designing materials for applications such as gas storage (e.g., for use as a vehicular fuel) and adsorptive cooling (e.g., for use in refrigerators). Usually, the goal when designing such systems is that the adsorbed molecules should bind to the substrate strongly, yet not so strongly that they cannot be desorbed when necessary. The interactions involved in the binding are primarily van der Waals interactions, which have strength of the order of a tenth of an eV.

Most of the previous work on weak binding of molecules on substrates has been focused on systems where the adsorbed molecules are non-polar, such as hydrogen, methane or carbon dioxide (none of which have a permanent electric dipole moment).[1–3] Study of the adsorption of such non-polar molecules has shown that the adsorption energy increases on going from a non-polar to polar substrate.[4] In this chapter, we study the adsorption of a polar molecule (using methanol as an archetype) on polar graphene-BN interfaces. This work has possible applications in, for e.g., thermal energy storage. We have tuned the adsorption energy of the polar methanol molecule by tuning the magnitude of the lines of localized electric charge that accumulate at the graphene-BN interface.

In modern day science, interfaces have given rise to many interesting discoveries. Combining together different materials results in novel and unexpected behavior that is not present in the component materials. Interfaces between bulk materials give rise to two-dimensional (2D) surfaces whereas interfaces between two-dimensional materials create one-dimensional (1D) lines.

Interfaces between bulk materials have been extensively studied in the last few years.[5;6] Among these, probably the most interesting work has been the study of heterostructures of strontium titanate ($SrTiO_3$) and lanthanum aluminate ($LaAlO_3$).[7] Despite both lanthanum aluminate and strontium titanate being insulators, when they form an interface, surface charges appear at the interface between the two materials. This gives rise to many interesting phenomena such as magnetism[8] and superconductivity[9] with many promising device applications.

On the other hand, the interfaces between two dimensional materials with different bulk polarization remain relatively unexplored. Recently it has been shown that just as a 2D electron gas can be created at the interface between three-dimensional bulk materials, interfaces between two dimensional materials can lead to the formation of 1D lines of charge.[10;11]

The polarization charge is solely determined by the bulk properties of the materials involved and the orientation of the interface. The magnitude of this interfacial charge is given by the difference in the bulk polarization of the two materials, and can be expressed as $\lambda_{\text{bound}} = -(\mathbf{P}_2 - \mathbf{P}_1) \cdot \mathbf{n}$, where $\mathbf{P}_1$ and $\mathbf{P}_2$ are the bulk polarizations of the two materials and $\mathbf{n}$ is the normal vector at the interface (see Fig. 3.1).

For a charge-neutral system, if a line of positive charge appears due to the discontinuity of polarization at one interface (say with material ‘1’ on the left-hand-side and material ‘2’ on the right-hand-side), on the other interface (with ‘2’ on the left-hand-side and ‘1’ on the right-hand-side) there will be an equal and opposite line of negative

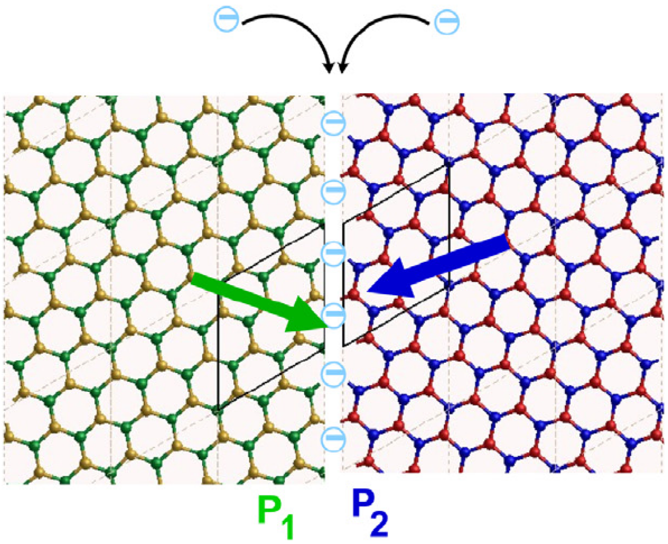

Figure 3.1: Polar discontinuity in a two dimensional honeycomb lattice composed of two domains with two different formal polarizations $\mathbf{P}_1$ and $\mathbf{P}_2$ results in a bound charge density at the interface. The figure is taken with permission from Ref. 12 ©(2015) Elsevier.

charge, so as to maintain the charge neutrality of the whole system. As a result, an electric field appears between the two interfaces. When the distance between the interfaces is sufficiently large, the free charge created by this electric field balances the polarization charge. This phenomenon is called as "polar catastrophe".[13;14]

In the present work, we are interested in the adsorption of a polar methanol molecule on systems that contain interfaces between graphene and BN. We note that though BN is a polar insulator, graphene (with a bulk polarization of zero) is actually a semi-metal, with a band gap of zero, but zero density of states at the Fermi level. However, this is true only for an infinite graphene crystal, and finite graphene fragments possess a band gap.[15;16] It is not immediately obvious whether the formalism developed for treating polar discontinuities between two polar insulators will be applicable to graphene-BN systems, which is an additional reason that makes their interfaces worthy of study.

One might expect that the greater the magnitudes of the lines of localized charge induced due to polar discontinuities at graphene-BN interfaces, the greater will be the adsorption energy of methanol, due to electrostatic interactions between the permanent dipole moment of methanol, and the line of charge at the interface. If we wish to maximize the adsorption energy of methanol, it follows that we should design the interface in such a way as to maximize the bound charge at the interface, i.e., the bound charge should not get compensated (either partially or completely) by induced free charges. As the electric field increases and the bound charge gets progressively compensated by free charge, the total charge at the interface will decrease, and hence the adsorption energy will also decrease.

Graphene-BN heterostructures have been studied previously, both theoretically[1]and experimentally[2]. They have been synthesized by chemical vapor deposition (CVD) technique on a Cu substrate, by simultaneously introducing methane and ammonia borane as the source for C and BN respectively.[3] The presence of localized interfacial states between graphene and BN has been observed by scanning tunneling microscopy (STM) and scanning tunneling spectroscopy (STS) for hybrid heterostructures on Cu[17] and on Au-intercalated Ir.[18]

In this chapter, we will try to analyze the weak binding between methanol and the substrate by dividing it into contributions from different kinds of van der Waals interactions. The three kinds of van der Waals interactions are London dispersion interactions, Debye interactions and Keesom interactions.[19] London dispersion interactions are purely quantum mechanical in nature, and arise from the interaction between two instantaneous fluctuating induced dipoles.[20] Debye interactions are usually defined as the electrostatic interactions between permanent dipoles/charges and induced dipole/charges.[21] Keesom interactions are frequently described as the electrostatic interactions between two permanent dipoles/charges;[22] note however that in the discussion below we will refer to also the electrostatic interaction between the permanent dipole moment of the adsorbed methanol molecule and the permanent charges created by engineering polar discontinuities in the graphene-BN substrate, as Keesom interactions. When analyzing our results, we have separated out these three kinds of van der Waals interactions, so as to determine which interaction is primarily responsible for enhanced binding.

A possible application of such methanol + graphene-BN systems is in thermal energy storage devices such as adsorption cooling refrigerators and air conditioners. Such devices are attracting increased attention as they are environmentally friendly; they operate on ‘waste heat’ and/or solar power, and do not make use of ecologically harmful chemicals such as freons.[23] In industrial processes and conventional electronics, up to 70% of the energy is actually waste heat, i.e., it does not perform any useful function. Methods that could somehow harness this heat for a useful purpose are extremely desirable. A frequently used adsorbate + adsorbent pair in adsorption cooling refrigerators is methanol + activated carbon.[24] The weight fraction of adsorbed methanol on activated carbon is high,[24] activated carbon has a high surface energy per unit mass, and can be cheaply produced from agricultural waste such as corn husk and coconut fiber. In order to increase the heat transfer during the operating cycle[24;25] which is the key parameter for thermal energy storage, one would like to increase the adsorption energy. Previous experiments[26;27] have shown a higher wetting enthalpy for methanol on BN-doped carbon foam than on plain carbon foam. We wish to not only provide theoretical support for these experimental results, but also to understand the underlying factors responsible for them, so as to possibly enable one to design better adsorbate + adsorbent pairs for future applications.

## 3.2 Systems under study

To study the adsorption of methanol, we consider six kinds of substrates (a) graphene (b) h-BN (c) striped graphene-BN systems with armchair interfaces, (d) striped graphene-BN systems with zigzag, (e) mixed BCN systems with a 1:1:1 B:C:N ratio, in the lowest energy atomic arrangement as determined by previous authors,[2;3] and confirmed by us and (f) triangular graphene islands, situated within a BN matrix, bounded by zigzag interfaces. Top views of representative examples of these six kinds of substrate systems are shown in Fig. 3.2. We first study the energetics of the interfaces in these systems as we vary the

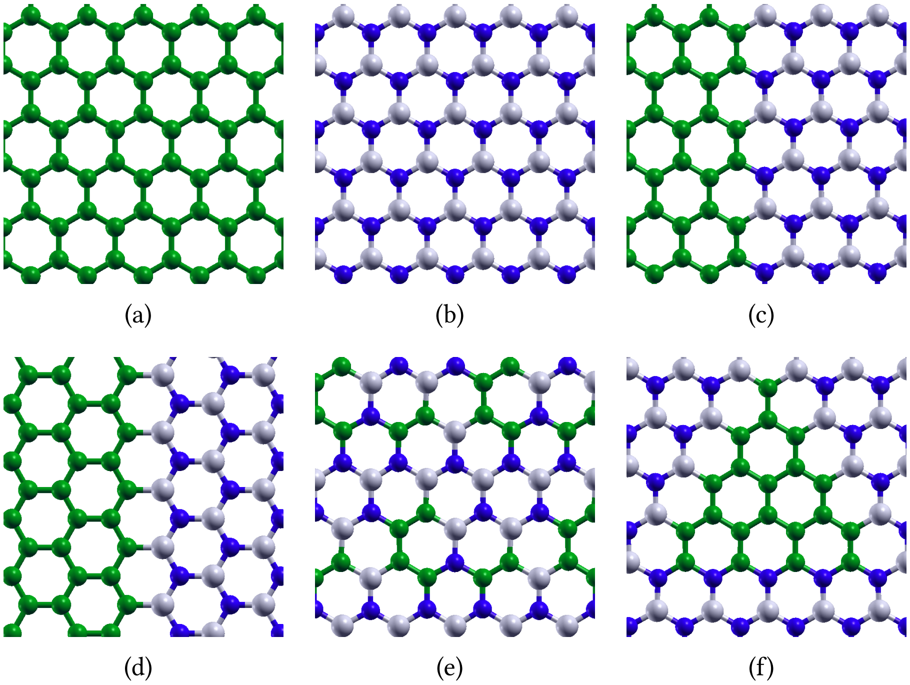

Figure 3.2: Top views of types of substrates considered for methanol adsorption: (a) graphene; (b) h-BN; (c) C-BN with an armchair interface; (d) C-BN with a zigzag interface; (e) mixed BCN; (f) triangular graphene island situated within BN matrix. Color scheme for atomic spheres: C (green), B (gray), N (blue).

separation between interfaces; we then go on to study methanol adsorption for certain specific separations.

For the calculation of methanol adsorption, we have chosen sufficiently large supercells so that interactions between periodic images of the methanol molecule (due to the use of periodic boundary conditions in our calculations) are negligible. Accordingly, we consider the following supercells: $5 \times 5$ cells for adsorption on pristine graphene and h-BN, an $8 \times 2\sqrt{3}$ cell for the stripe with armchair interfaces, and a $5\sqrt{3} \times 3$ cell for the stripe with zigzag interfaces. For adsorption on a mixed BCN system with a 1:1:1 ratio of B:C:N, we consider a 72-atom $6 \times 6$ unit cell, and a $7 \times 4\sqrt{3}$ cell for the triangular graphene island structure within BN.

In all cases, we start from a number of different initial geometries (orientations as well as lateral shifts of the methanol molecule with respect to the substrate), so as to enable us to explore the potential energy surface, and give us a greater chance of finding the structure corresponding to the global minimum in the energy landscape.

## 3.3 Computational Details

Our calculations have been performed using *ab initio* density functional theory (DFT),[28;29] as implemented in the Quantum ESPRESSO package.[30] A generalized gradient approximation of the PBE form[31] was used to describe the exchange-correlation interactions. Electronic wavefunctions were expanded using a plane wave basis set, with wavefunction and charge density cutoffs of 40 Ry and 400 Ry, respectively. Interactions between ionic cores and valence electrons were described using ultrasoft pseudopotentials.[32] The Broyden-Fletcher-Goldfarb-Shanno (BFGS) scheme for minimization of a function was used until the forces on all atoms were less than 0.001 Ry/bohr.[33–36] The Brillouin zone was sampled with a Monkhorst-Pack[37] mesh comprised of 15×15×1 k-points for the primitive unit cells of graphene and BN, and proportionately equivalent meshes for larger supercells. As we have considered monolayers of graphene, BN or graphene-BN as the substrates for methanol adsorption, along the $z$ direction (normal to the surface plane) we introduced a vacuum spacing of 15 Å so as to reduce interactions between artificially periodic images along this direction. Marzari-Vanderbilt cold smearing[38] with a width of 0.001 Ry was used for better convergence. In order to incorporate dispersion interactions, we have used the ‘ DFT-D2’ treatment introduced by Grimme.[39]

The adsorption energy of methanol on the substrate was computed as

$$E_{\text{ads}} = -(E_{\text{subs+CH}_3\text{OH}} - E_{\text{subs}} - E_{\text{CH}_3\text{OH}}), \tag{3.1}$$

where the three terms on the right-hand-side are the total energies from our DFT calculations of, respectively, methanol adsorbed on the substrate, the bare substrate, and an isolated methanol molecule in the gas phase.

To visualize the induced charges upon the adsorption of methanol on the substrate, we have plotted isosurfaces of the charge redistribution $\Delta\rho$, which is given by:

$$\Delta\rho = \rho_{\text{subs+CH}_3\text{OH}} - \rho_{\text{subs}} - \rho_{\text{CH}_3\text{OH}}, \tag{3.2}$$

where the three terms on the right-hand-side are the electronic charge densities for the systems consisting of, respectively, methanol adsorbed on the substrate, the bare substrate, and an isolated methanol molecule in the gas phase. However, in this case, unlike in Eq. (3.1), the second and third terms on the right-hand-side of Eq. (3.2) were evaluated not at their respective equilibrium geometries, but frozen at the geometries that they have in the combined system.

We have calculated the dipole moment of an isolated methanol molecule to be 1.60 D which is in good agreement with the experimental value of 1.69 D.[40] When calculating electrostatic interactions, we assumed that this dipole moment was positioned on the center of mass of the methanol molecule, with a direction that was easily calculated since the three cartesian components of the dipole moment were individually computed. Keesom interactions were calculated by making use of permanent charges on the substrate atoms; these permanent charges (i.e., charges in the absence of the methanol molecule) were calculated using Natural Bond Orbital (NBO) charge analysis.[41] Induced charges (i.e., changes in the charges on both the methanol molecule and the substrate upon bringing the molecule and the substrate together) were calculated by integrating lobes of the charge redistribution $\Delta\rho$.

## 3.4 Results

### 3.4.1 Benchmarks

First, we optimize the structure of graphene and h-BN. The optimized lattice parameters of graphene and h-BN are obtained to be 2.46 Å and 2.51 Å respectively. These values are in excellent agreement with the experimental values of 2.47 Å and 2.51 Å, respectively.[42;43] For the methanol molecule we obtain the optimal O-H and C-O bond lengths as 0.98 Å and 1.42 Å, respectively, which are in excellent agreement with the experimental values of 0.97 Å and 1.42 Å, respectively.[40]

### 3.4.2 Interface formation energies

We wish to first check whether C-BN lateral heterostructures prefer to form a fully intermixed structure or to phase segregate into domains of graphene and h-BN separated by interfaces. To investigate this, we first consider systems with 1:1:1 ratio of C:B:N. We consider four kinds of systems: (a) alternating striped domains of graphene and h-BN, separated by armchair interfaces [see, e.g., Fig. 3.2(c)], (b) alternating striped domains of graphene and h-BN, separated by zigzag interfaces [see, e.g., Fig. 3.2(d)], (c) a low-energy mixed structure obtained by previous authors[2;3] [see, e.g., Fig. 3.2(e)] and (d) a triangular graphene island situated within a BN matrix, bounded by zigzag interfaces [see, e.g., Fig. 3.2(f)].

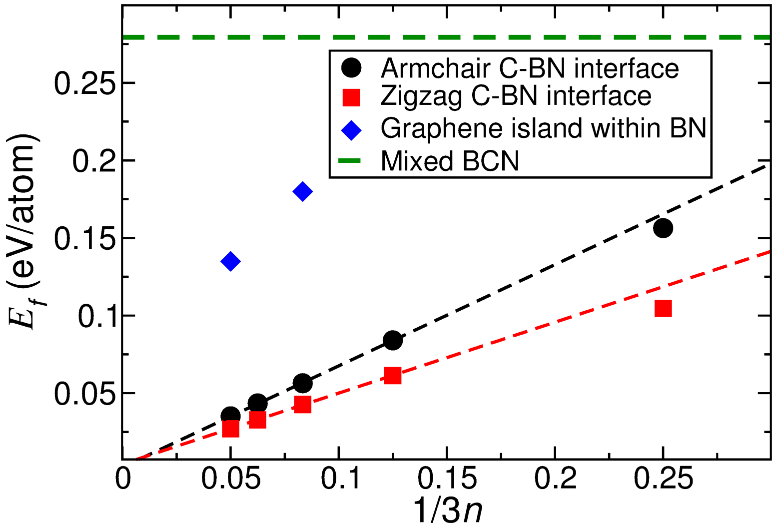

Figure 3.3: Formation energy $E_f$ per atom as computed from DFT calculations for BCN systems with 1:1:1 ratios for B:C:N. $n$ is the number of B, C or N atoms in the primitive unit cell; for the striped structures, as $n$ increases, the separation between domain walls increases. Results are shown for stripes with armchair interfaces (black dots), stripes with zigzag interfaces (red squares), triangular graphene island within BN matrix (blue diamonds), and a mixed BCN structure (green dashed line). Note that a phase segregated structures of graphene and h-BN are favored over the formation of the mixed BCN structure, and striped domains of graphene and BN separated by zigzag interfaces are energetically most favorable for smaller domain wall separations.

In order to examine the relative stability of these different BCN structures, we calculate their formation energy with respect to graphene and h-BN. The formation energy $E_f$ is given by:

$$E_f = -(1/3n)(E_{\mathrm{B}_n\mathrm{C}_n\mathrm{N}_n} - (n/2)E_{\mathrm{C}_2} - nE_{\mathrm{BN}}); \tag{3.3}$$

here, the first term on the right-hand-side of the equation is the total energy of a unit cell of BCN containing $n$ number of C, B and N atoms, $E_{\mathrm{C}_2}$ is the total energy of the primitive unit cell of graphene (containing 2 carbon atoms), and $E_{\mathrm{BN}}$ is the total energy of a primitive unit cell of BN (containing one B and one N atom).

In Fig. 3.3, we plot the formation energy $E_f$ as a function of $(1/3n)$ for armchair interfaces (black circles), zigzag interfaces (red squares) and triangular island structures (blue diamond). Note that as $n$ increases, the distance between domain walls also increases. Note also that due to the imposition of periodic boundary conditions and the 1:1:1 ratio of the three elements, we can form the triangular island structure only for certain values of $n$ and are also forced to bound the triangle by two C-B interfaces and one C-N interface. From Fig. 3.3, we see that there is a repulsive interaction between domain walls, i.e., $E_f$ decreases as $n$ increases and $1/3n$ decreases. For much of the graph (corresponding to relatively small values of $n$), the formation energy is lower for the zigzag interface than for the corresponding armchair interface; however our results suggest that for large domain widths (i.e., very small values of $(1/3n)$ – note that the black and red dashed lines appear to cross in this region) the situation will flip, i.e., the formation energy of the armchair interface becomes less than that of the corresponding zigzag interface. In Fig. 3.3 we have also plotted the value of $E_f$ corresponding to the mixed BCN structure shown in Fig. 3.2(e) (horizontal green dashed line); we see that it lies considerably higher in energy than the striped and triangular island structures, by about 0.12 to 0.28 eV per atom, depending on the domain size.

Next, we look at how the formation energy $E_f$ changes with stoichiometry. To do this, we consider 60-atom unit cells. We consider five kinds of systems: (a) striped domains of graphene and h-BN separated by a zigzag interface (b) a triangular graphene island situated within a BN matrix, bounded by zigzag interfaces, (c) three kinds of mixed BCN: (i) 'Mixed BCN-1', these are structures where $N_{\mathrm{C-C}} = N_{\mathrm{C-N}} = N_{\mathrm{C-B}}$, where $N_{X-Y}$ is the

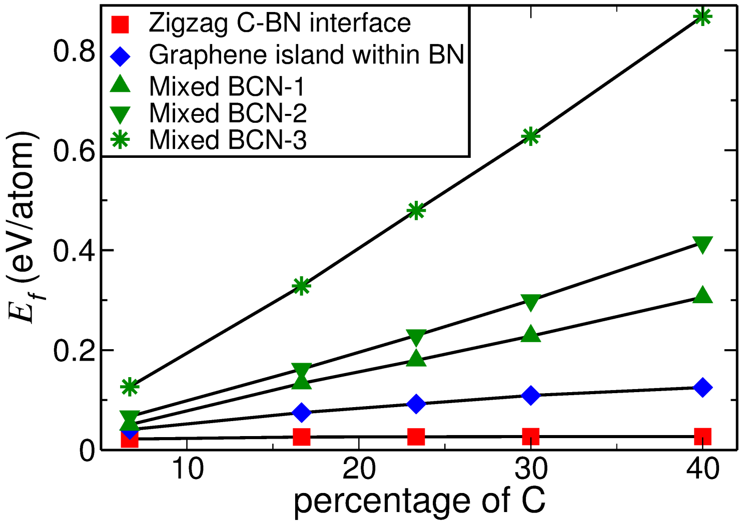

Figure 3.4: Formation energy $E_f$ per atom as computed from DFT calculations as a function of concentration of C with 1:1 ratios for B:N. Results are shown for structures where the primitive unit cell contains 60 atoms, for stripes with zigzag interfaces, triangular graphene islands within BN matrix, and three kinds of mixed BCN structures (see text for descriptions). Note that striped domains of graphene and h-BN separated by zigzag interfaces are energetically most favorable for all concentrations and the difference in formation energy between different structures increases as the percentage of C atoms increases.

number of nearest-neighbor bonds between atoms of species $X$ and $Y$, (ii) 'Mixed BCN-2', these are structures where $2N_{\mathrm{C-C}} = N_{\mathrm{C-N}} = N_{\mathrm{C-B}}$, and (iii) 'Mixed BCN-3', these are structures were $N_{\mathrm{C-C}} = 0$ and $N_{\mathrm{C-N}} = N_{\mathrm{C-B}}$.

Fig. 3.4 shows the formation energy $E_f$ as a function of the concentration of C atoms present in the system. For all the concentrations considered, the striped zigzag C-BN interface is most favored, followed by the triangular graphene island within the BN matrix and then Mixed BCN-1, Mixed BCN-2 and Mixed BCN-3, respectively. One piece of important information we extract from Fig. 3.4 is that the difference in formation energy between different structures increases as the percentage of C atoms increases. We note that this energetic ordering is in agreement with a previous report in the literature[44] that there is an hierarchy of the energetic stability of bonds of different types, given by B-N > C-C > C-N > C-B > B-B > N-N (with B-N being the most stable and N-N being the least stable). We also conclude that although the striped zigzag C-BN interface is the lowest in energy for a given stoichiometry, the triangular graphene island within a BN matrix is only slightly higher in energy, and one is therefore quite likely to find such structures present. We note that this conclusion is supported by experimental reports.[45]

### 3.4.3 Polar Discontinuity and Lines of Charge

The zigzag C-BN interface is polar whereas the armchair C-BN interface is non-polar.[46] For zigzag interfaces, due to the polar discontinuity between graphene and h-BN, a bound charge appears at the interface. In the thermodynamic limit, this bound charge is perfectly balanced by a free carrier charge density $\lambda_{\text{free}}$; this is called the polar catastrophe.[13;14]

In this context, we consider two types of configurations. In both the cases the unit cell consists of 20 C atoms, 20 B atoms and 20 N atoms. In the first case, we consider a striped zigzag C-BN interface and in the second case we consider a triangular island of C within BN matrix. Note that while all three sides of the triangle have zigzag interfaces, two of the sides have C-B bonds, whereas the third side has C-N bonds; only in this way was it possible to have the same number of C, B and N atoms in the two structures shown in panels (a) and (b).

It is of interest to compare the amount of charge at the interfaces of these two structures. For easy visualization of the charge at the interface, one can employ various methods. We first do this by employing a ‘trick’. In Fig. 3.5 we show two charge difference plots between the C-BN systems (striped zigzag and island structure) and a graphene sheet, i.e., a system in which all the atoms are carbon atoms. In the parts of the C-BN system consisting of carbon atoms, the charge difference $\Delta\rho$ is zero, since the C-BN system and graphene have essentially the same charge density. However, in the BN domain, such a charge difference plot shows clearly the ionic nature of the bonding, with red lobes (indicating an area of excess negative charge) surrounding N atoms, and blue lobes (indicating an area of excess positive charge) surrounding B atoms. Because of the highly symmetric arrangement of B and N atoms in h-BN, in the interior of the BN domain, the net dipole moment is zero. However, this symmetry is broken at the interface, and

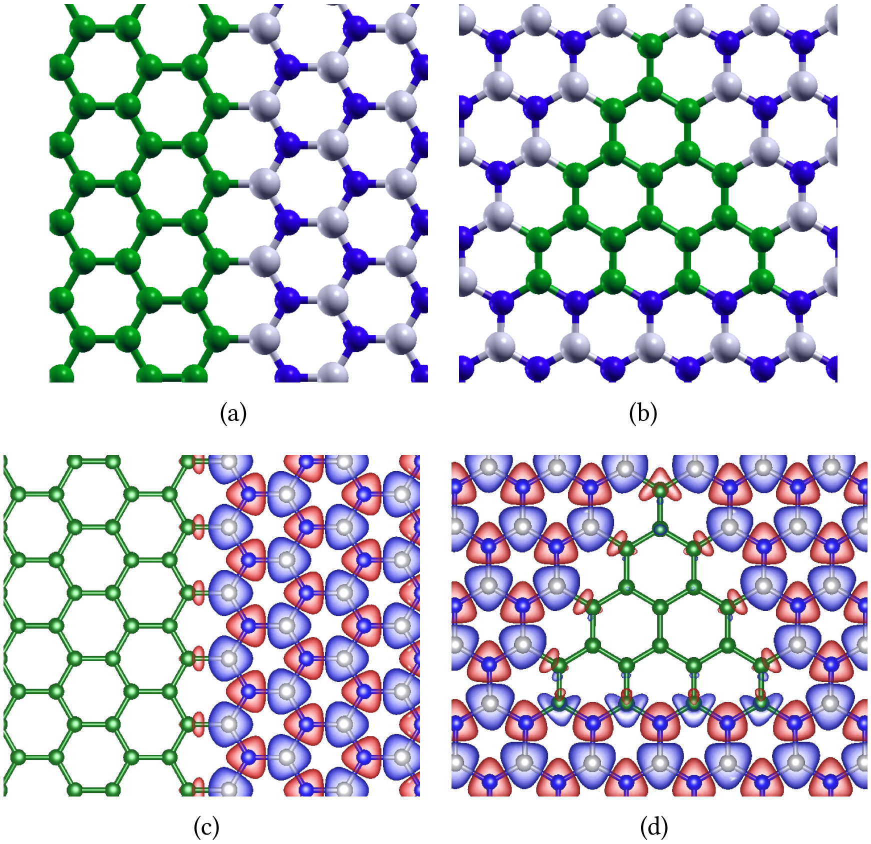
(a) (b)

(c) (d)

Figure 3.5: Top views showing atomistic structure and charge difference plots. Structure of (a) striped domains of graphene and h-BN separated by a zigzag interface; (b) triangular graphene island situated within BN matrix. Charge density difference plots between the C-BN systems and a system in which all the atoms are replaced by carbon atoms, for (c) striped domains of graphene and h-BN separated by a zigzag interface; (d) triangular graphene island situated within BN matrix. In (c) and (d), red and blue lobes correspond to a gain and loss of electronic charge respectively. Isosurfaces corresponding to $\Delta\rho = \pm 0.009$ e/(bohr)$^3$ have been plotted. Color scheme for atomic spheres: C (green), B (gray), N (blue).

one sees that a line of charge is created at the zigzag interfaces [see Fig. 3.5 (a)]. In this figure, we have only shown the C-B zigzag interface, at which a line of negative charge (red lobes) appears, there will be a similar line of positive charge at the C-N interface. Similarly, for the island structure, (see Fig. 3.5 (b)) there are lines of negative charge at the two sides of the triangle that feature C-B bonds, and positive charge on the third side featuring C-N bonds. However, we can see that there is a larger negative charge at the apex of the triangle where the two sides composed of C-B bonds meet. On comparing (a) and (b), as well as on evaluating the magnitude of the interfacial charge, one finds that the charges are larger in (b) than in (a). This is because of depolarizing fields are larger in (a), both because of the larger separation between domain walls and the orientation of the domain walls.

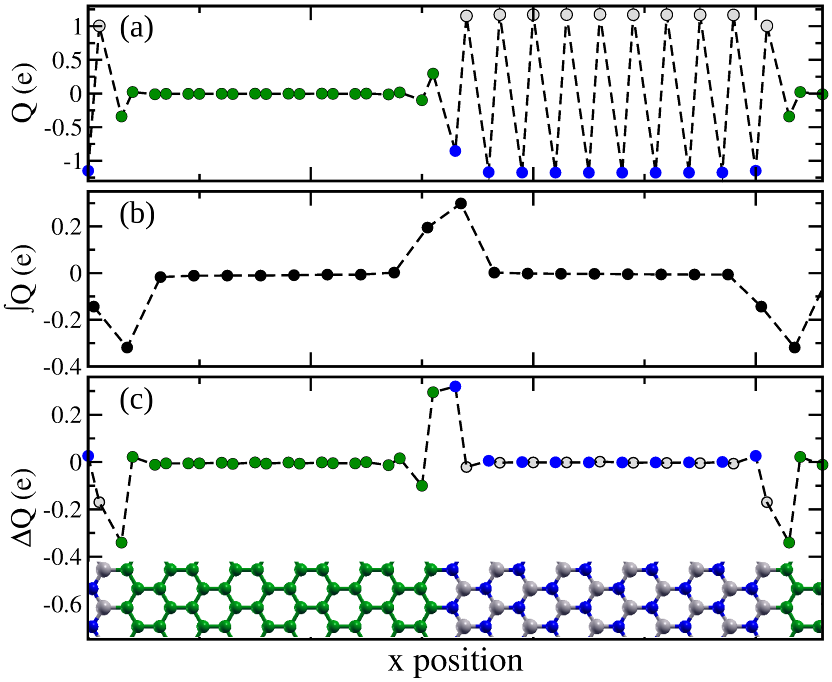

Figure 3.6: Charge localization at interfaces, as calculated by the NBO method. (a) Total charge on each atom as a function of its $x$ coordinate (b) sum of charges of successive pairs of atoms, as a function of $x$, and (c) Difference between charge on each atom in the striped domain structure and the corresponding species of atom in the bulk material, as a function of $x$ The unit cell of the striped zigzag C-BN interface consists of 20 C, 10 B and 10 N atoms, as shown in the bottom of the figure. Color scheme for atomic spheres: C (green), B (gray), N (blue).

We will now depict the lines of charge at the interface in another way. In Fig. 3.6(a), we have plotted the charge (as obtained using the NBO analysis) on each atom in the primitive unit cell for the striped zigzag structure shown at the bottom of panel (c). We see that in the graphene region, all atoms have charge zero, whereas in the BN region, the boron/nitrogen atoms have positive/negative charge. There is however a change in the charges at the interface region. If we integrate the charges over a region of $x$ corresponding to 2.155 Å, we see in Fig. 3.6(b) that we have net zero charge in the interior of both the graphene and BN domains. However, we have a positive charge at the zizgag interface featuring C-N bonds, and a negative charge at the interface featuring C-B bonds. This charge is seen to be localized in the neighborhood of the two interfaces. Panel (c) shows the same information as panel (a), but this time showing $\Delta Q$, the difference in charge $Q$ between the atoms in the striped zigzag system and an atom of the same species in a bulk system.

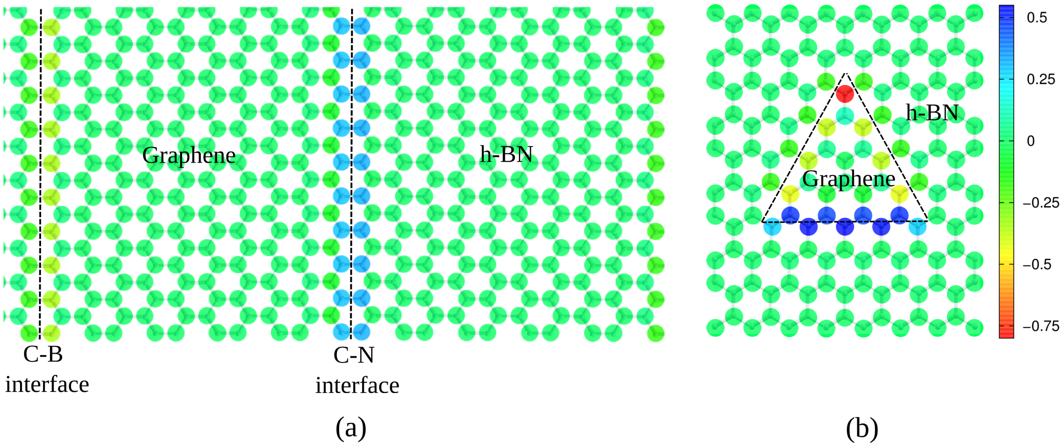

Figure 3.7: Difference between total charge on each atom and charge on each atom in the corresponding bulk system (i.e., no interfaces present) for (a) striped zigzag C-BN interface and (b) graphene island within BN matrix has been shown by the color gradient. The blue color denotes maximum positive charge and red color denotes maximum negative charge. The intermediate colors denote the amount of charge according to the color bar shown on the right hand side. Fig. 3.7(b) may be compared with Fig. 3.5(b)

We will now show the localization of lines of charge at the interface in a third way. In Fig. 3.7 we have plotted again the atomistic structure of the two systems, but this time each atom is colored according to $\Delta Q$, following the color bar on the right of the figure. An aqua green color represents $\Delta Q = 0$; we see that most atoms have this color; i.e., they have the same charge as they would have in the bulk system. However, in Fig. 3.7(a), we see that for the striped system, we have negative/positive lines of charge at the zigzag C-B/C-N interfaces. In Fig. 3.7(b), we see that the lines of charge on the two C-B sides are slightly more negative, and on the C-N side are strongly more positive. However, the largest $|\Delta Q|$ is seen to occur at the apex of the triangle, where the two C-B sides meet, where we have a strong localization of negative charge.

### 3.4.4 Adsorption of Methanol

Next, we consider the adsorption of a methanol molecule on the six kinds of substrates: (a) graphene, (b) h-BN, (c) a striped armchair interface between graphene and h-BN, (d) a striped zigzag interface between graphene and h-BN, (e) a mixed BCN with a 1:1:1 B:C:N ratio and (f) a triangular graphene island, situated within a BN matrix, bounded by zigzag interfaces.

By considering various initial geometries, we have obtained a number of stable adsorption geometries for methanol on graphene. Eight examples are shown in Figs. 3.8(a)–(h), they are labeled C1–C8 in order of decreasing stability. A top view of the most favored adsorption geometry C1 for methanol on graphene is shown again in Fig. 3.9(a). We obtain $E_{\text{ads}}$ = 0.26 eV, which is close to an earlier reported value of 0.22 eV.[47] In the lowest energy configuration, the O-H bond of the methanol molecule is pointed towards a hollow site on the graphene sheet, and the C atom of the methanol molecule is positioned vertically atop a C atom of the graphene sheet. The O and C atoms of methanol lie at vertical heights of 3.20 Å and 3.21 Å respectively, above the graphene sheet, i.e., the O–C bond in methanol lies almost parallel to the graphene substrate.

Similarly, we find a number of stable adsorption geometries for methanol on h-BN. Eight examples are shown in Figs. 3.8(i)–(p); they are labeled again C1–C8 in order of decreasing stability. The top view of the most favored adsorption geometry C1 on h-BN is shown again in Fig. 3.9(b). For this geometry, we obtain $E_{\text{ads}}$ = 0.29 eV, i.e., the binding is increased by 11% relative to that on graphene. In this lowest energy configuration, the O-H bond of methanol now points toward an N atom on the h-BN substrate rather than a hollow site, and the C atom in methanol now lies vertically above a bridge site on the substrate. The O atom of the methanol is also now somewhat closer to the substrate than it was on graphene: it now sits at a vertical height of 3.15 Å above the substrate; however the C atom of methanol sits at a height of 3.22 Å.

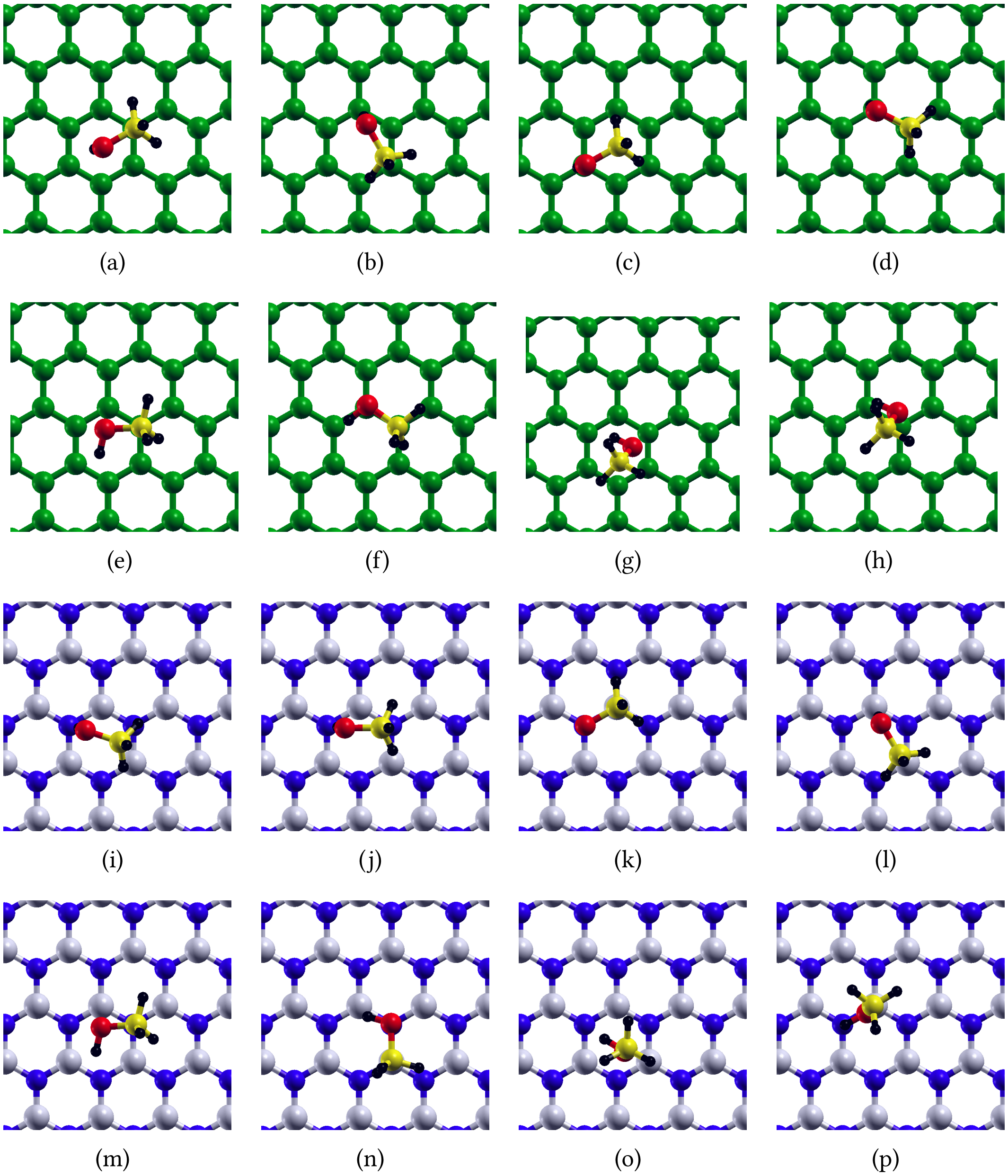
(a) (b) (c) (d)

(e) (f) (g) (h)

(i) (j) (k) (l)

(m) (n) (o) (p)

Figure 3.8: Top views of different stable adsorption geometries obtained for methanol on graphene and h-BN; (a)-(h) are the C1-C8 configurations for methanol on graphene and (i)-(p) are the C1-C8 configurations for methanol on BN. Color scheme for atomic spheres: C-graphene (green), C-methanol (yellow), H (black), O (red), B (gray), N (blue).

Next, we consider the adsorption of methanol on two types of striped C-BN interfaces: armchair and zigzag. The top views of the most favored adsorption geometries are shown in Figs. 3.9(c) and 3.9(d), respectively. In these most favored geometries, the adsorption energy is 0.31 eV for the armchair interface and 0.34 eV for the zigzag interface. Thus, by creating striped C-BN interfaces, the binding of methanol can be increased by up to 16%

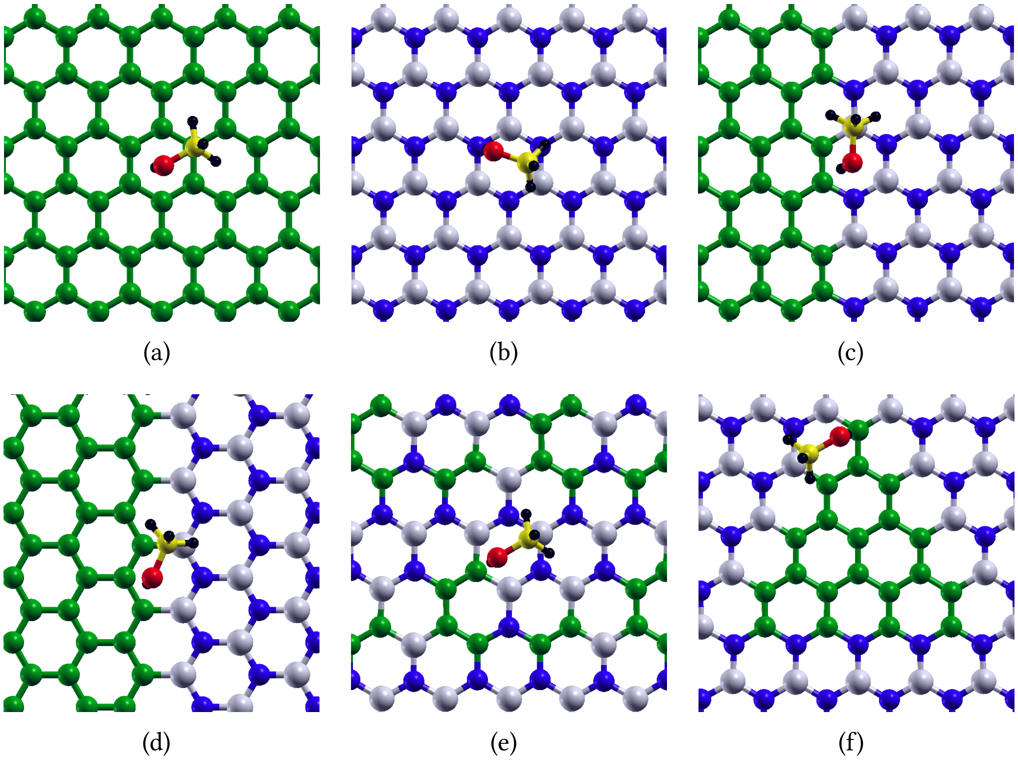
(a) (b) (c) (d) (e) (f)

Figure 3.9: Top views of the optimal adsorption geometries for methanol on the six different kinds of substrates considered: (a) graphene; (b) h-BN; (c) C-BN with an armchair interface; (d) C-BN with a zigzag interface; (e) mixed BCN; (f) triangular graphene island within BN. Color scheme for atomic spheres: C-graphene (green), C-methanol (yellow), H (black), O (red), B (gray), N (blue).

(at armchair interfaces) and up to 31% (at zigzag interfaces), with respect to the binding on graphene. For a striped zigzag C-BN system, there are two kinds of interfaces: C-B and C-N. Of these two, we find that adsorption is more favorable on the former; on the latter kind of interface, the highest value of $E_{\text{ads}}$ found by us is 0.24 eV. This can be understood by steric considerations. Upon looking at the charges on an isolated methanol molecule, we find that there is a positive charge of 0.59 e on the O atom, and there is a negative charge of -0.64 e on the C atom (there is almost no net charge on the H atoms). Since the C atom is in the interior of the molecule whereas the O atom is closer to the exterior, it is more favorable for the positively charged O atom to come close to the negatively charged C-B interface, thereby lowering the electrostatic energy.

For methanol adsorption on mixed BCN, the top view of the most favored adsorption geometry is shown in Fig. 3.9(e). The binding is significantly increased with respect to graphene, with $E_{\text{ads}}$ = 0.35 eV, an enhancement of 32% over that on graphene. Though this value of $E_{\text{ads}}$ is very slightly higher than that on a striped C-B zigzag interface, we recall that we have found that the mixed configuration of the substrate is not energetically favored, compared to structures where domains of graphene and h-BN are separated by zigzag or armchair interfaces.

Finally, we consider the adsorption of methanol on the triangular graphene island within a BN matrix. The adsorption energy is highest in this case with $E_{\text{ads}}$ = 0.43 eV. This corresponds to an enhancement of 65% in the adsorption energy over that on graphene. In the most favored geometry the O-H bond of the methanol molecule is pointed towards the vertex of the triangle where two C-B interfaces meet, and the C atom of the methanol molecule is positioned vertically atop the B atom at the vertex. The O and C atoms of the methanol molecule lie at vertical heights of 3.02 Å and 3.07 Å respectively.

## 3.5 Analysis and Discussion

We want to examine the different factors that are playing role in determining the energetics and favored configurations. As mentioned above, we will separate out the contributions from London, Debye and Keesom interactions, where interactions between the permanent dipole moment of the methanol molecule and the lines of charge that appear at C-B and C-N interfaces are subsumed into the Keesom interactions.

We will first discuss what factors determine the most favored geometry of a methanol molecule on pristine graphene and pristine BN. For both these substrates, we have found a number of stable geometries, with a wide range of values of $E_{\text{ads}}$. The top views of some of these different possible adsorption geometries for a methanol molecule adsorbed on graphene and BN are shown in Fig. 3.8

From our DFT calculations, it is possible to extract the contribution from London dispersion to the total energy of a configuration and hence the adsorption energy. For methanol adsorbed on the substrate, the dispersion contribution $E_L$ is given by:

$$E_{\mathrm{L}} = -(E^{\mathrm{disp}}_{\mathrm{subs+CH_3OH}} - E^{\mathrm{disp}}_{\mathrm{subs}} - E^{\mathrm{disp}}_{\mathrm{CH_3OH}}), \tag{3.4}$$

where the three terms on the right-hand-side of the equation are the contribution from London dispersion interactions (LDI) to the total energy of the corresponding systems.

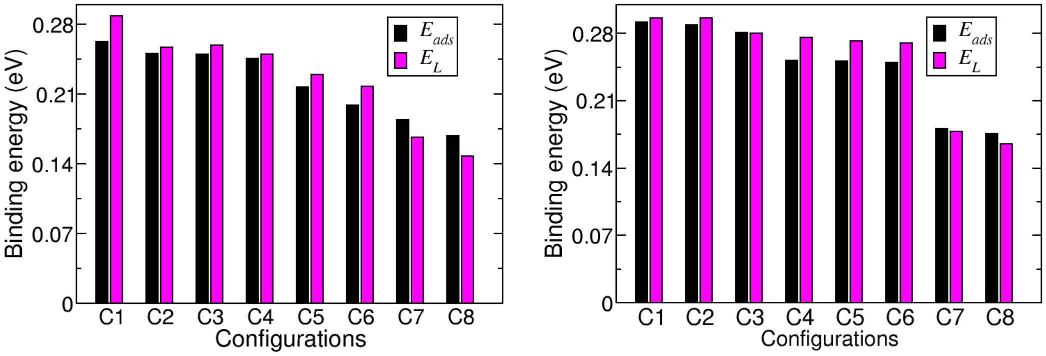

(a) (b)

Figure 3.10: Bar charts indicating results from DFT calculations for the adsorption energy $E_{\mathrm{ads}}$ and the corresponding value of $E_L$, the contribution to it from London dispersion interactions, for methanol adsorbed on (a) graphene and (b) h-BN. $E_{\mathrm{ads}}$ and $E_L$ are indicated by black and magenta bars, respectively. C1–C8 are eight low-energy stable adsorption geometries shown in Fig. 3.8.

In Figs. 3.10(a) and 3.10(b), we have shown the values of $E_{\mathrm{ads}}$ (black bars) and $E_L$ (magenta bars online) for several different stable configurations, for adsorption on graphene and h-BN, respectively. We can see that the trends in $E_{\mathrm{ads}}$ follow the trends in $E_L$; i.e., to a pretty good approximation, we can conclude that the relative ordering of the energetics of different adsorption geometries is determined by the strength of LDI in these geometries – when we are considering adsorption on pure graphene or pure h-BN.

We have mentioned above that as the distance between neighbouring interfaces increases, there is a greater amount of free charge in the system that can partially balances the bound charge that appears at the interfaces due to the discontinuity in polarization.Thus, one would expect that as the distance between interfaces increases, the bound charge at the interface should decrease, and the adsorption energy should also decrease. To verify whether this is indeed true, we have considered four different graphene-BN interfaces: (a) a graphene island within a BN matrix where there is essentially no compensation of bound charge by free charge (b) a striped system where the neighbouring zigzag interfaces are 10.85 Å far apart (c) a striped system where the neighbouring zigzag interfaces are 21.76 Å far apart (d) a striped system where the neighbouring zigzag interfaces are 42.79 Å far apart. For all these systems, we have considered adsorption of methanol.

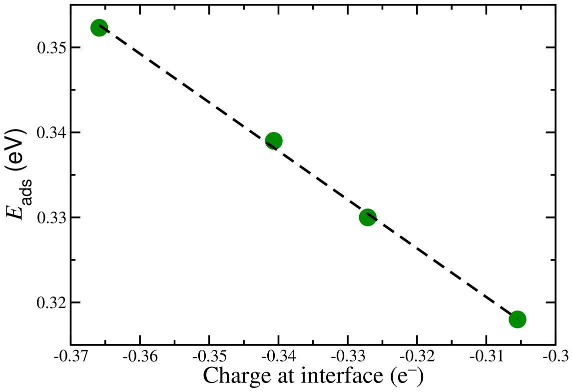

Figure 3.11: Adsorption energy as a function charge at the interface for graphene island within BN matrix and three striped zigzag C-BN interfaces with neighbouring interfaces 10.85 Å 21.76 Å and 42.79 Å far apart. The plot shows a linear relationship between $E_{ads}$ and the charge at the interface.

From Fig. 3.11 we can see that for striped zigzag C-BN interfaces, as the distance between the interfaces increases, the total charge at the interfaces decreases. We find that indeed, as a result, the adsorption energy also decreases. From the figure, we find that the adsorption energy of methanol on the substrates correlates quite well with the charge at the interface.

When we consider all six substrates for methanol adsorption, for all the lowest energy configurations as shown in Fig. 3.9, the value of $E_L$ is more or less the same although the values of $E_{\text{ads}}$ differ significantly on these six different substrates. Thus, though the majority of the binding comes from London dispersion interactions, the enhancement in binding on going from graphene to h-BN and further to BCN, cannot be explained by an increase in the contribution from London dispersion interactions. In Fig. 3.12(a) we have split up the contribution to $E_L$ from interactions of the methanol molecule with C,

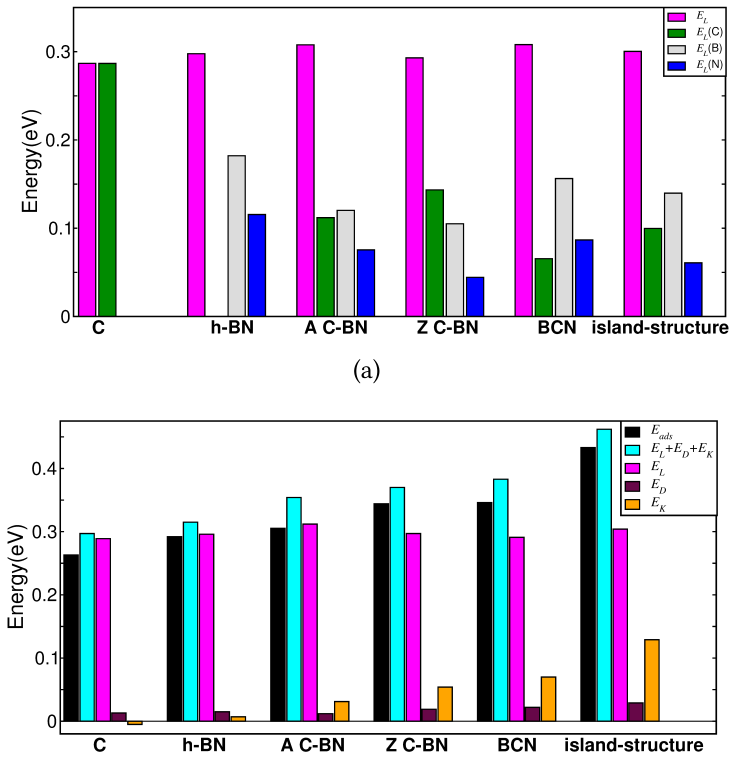

(a)

(b)

Figure 3.12: (a) Bar chart indicating the contributions from different types of atoms in the substrate to $E_L$, for the lowest energy geometry on each of the six kinds of substrates considered. While the magenta bar shows the total value of $E_L$, arising due to London interactions between the methanol molecule and all the atoms in the substrate, the green, gray and blue bars show the individual contributions to $E_L$ from the interaction of methanol with C, B and N substrate atoms, respectively. The substrate labels C, h-BN, A C-BN, BCN and island structure correspond to graphene, boron nitride, armchair interface, zigzag interface, mixed BCN and island structure of graphene inside BN sheet respectively. (b) Bar chart indicating the stepwise enhancement in adsorption energy $E_{\text{ads}}$ as one proceeds from one substrate to the next, and its break-up into contributions from the three different kinds of van der Waals interactions. The adsorption energy $E_{\text{ads}}$ computed from DFT is shown by black bars, while the contributions from London, Debye and Keesom interactions are shown by magenta, maroon and orange bars, respectively.

B and N atoms of the substrate, respectively, for the lowest energy adsorption geometries for the six kinds of substrates considered in this study. We see that though the relative and absolute sizes of these contributions is different in each case, they add up to yield approximately the same value of $E_L$, as we had already mentioned above.

Next to quantify the electrostatic interactions, we consider the permanent charges on the substrate, permanent dipole moment of methanol molecule, induced charges on the

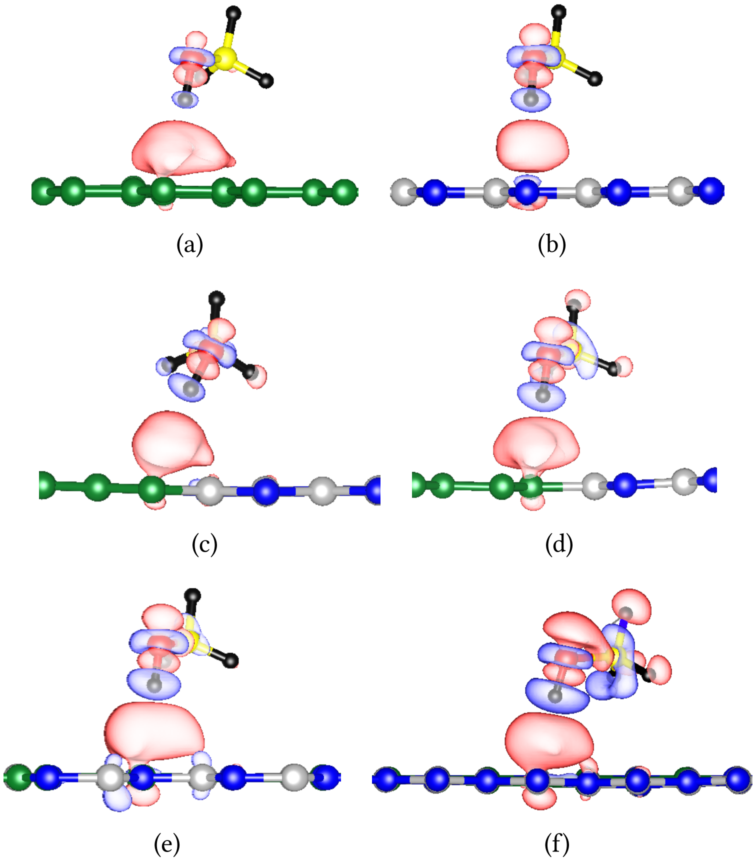

Figure 3.13: Redistribution of electronic charge upon the adsorption of methanol on (a) graphene (b) BN (c) zigzag C-BN (d) armchair C-BN (e) mixed BCN (f) island structure. Red and blue lobes correspond to a gain and loss of electronic charge respectively. The isosurfaces corresponding to $\Delta\rho = \pm 0.0006$ e/(bohr)$^3$ are plotted. Color scheme for atomic spheres: C-graphene (green), C-methanol (yellow), H(black), O (red), B (gray), N (blue).

substrate and induced charges on the methanol molecule. Accordingly, in Fig. 3.13 we have plotted the isosurfaces of the charge redistribution $\Delta\rho$ [recall Eq. (3.2)] for the most favored adsorption geometries on the six kinds of substrates considered here.

From Fig. 3.13 we can say that for all the six cases, upon methanol adsorption, there is induced electron density in the $\pi$ cloud of the substrate, just below the methanol molecule [large red lobes in Figs. 3.13(a)–(f)] and an induced multipole on the methanol molecule. The strength of this induced multipole increases from Fig. 3.13(a) to Fig. 3.13(f), reflecting also the increase in $E_{\text{ads}}$.

Next, we wish to quantify the contributions to adsorption energy from different kinds of van der Waals interactions. We have already seen (recall green bars Fig. 3.12) that the contribution $E_L$ to all six systems is almost the same. This is quite interesting, given that the adsorption geometries in the six systems look quite different: in some of them, the C atom in methanol sits at an atop site, and in others it sits at a bridge site. However, we note that there are certain similarities also, e.g., in all six cases, the polar O-H bond in methanol points toward a substrate atom; moreover, this substrate atom is always a C atom, except for the case of a BN substrate, where no C atoms are present in the substrate.

As for all the substrates, the value of $E_L$ is same, it follows that enhancements in $E_{\text{ads}}$ on going from graphene to the other substrates must arise from various kinds of electrostatic interactions. We first look at the Debye contribution $E_D$. This comes from the electrostatic interactions between the permanent moment of the methanol molecule and the induced charges on the substrate, and the electrostatic interactions between the induced charges on the methanol molecule and permanent charges on the substrate atoms. The Debye contribution can be calculated using the formula

$$E_D = \sum_i \frac{q_i^{\text{ind}}}{4\pi\epsilon_0} \frac{\vec{\mu}^{\text{perm}} \cdot \mathbf{R}_i}{{R_i}^3} + \sum_{j,k} \frac{Q_j^{\text{ind}} \; q_k^{\text{perm}}}{4\pi\epsilon_0 r_{jk}}, \tag{3.5}$$

where $i$ and $j$ run over all the lobes of induced charge in the substrate and the methanol molecule, respectively, and $k$ runs over all the atoms in the substrate; $q_i^{\text{ind}}$ and $Q_j^{\text{ind}}$ are the total charge contained in the $i$th lobe of induced charge in the substrate, and the $j$th lobe of induced charge in the methanol molecule, respectively, $q_k^{\text{perm}}$ is the permanent charge on the substrate atom $k$, $\vec{\mu}^{\text{perm}}$ is the permanent dipole moment of the methanol molecule; $\mathbf{R}_i$ is the vector connecting the weighted center of the $i$th lobe of induced charge in the substrate to the center of the methanol dipole moment, $r_{jk}$ is the distance from the weighted center of the $j$th lobe of induced charge in the methanol molecule to the $k$th atom in the substrate; $\epsilon_0$ is the permitivity of free space. The first term on the right-hand-side of Eq. (3.5) denotes the electrostatic interaction between the permanent moment of the methanol molecule and the induced charges on the substrate, while the second term on the right-hand-side of Eq. (3.5) denotes the electrostatic interaction between the induced charges on the methanol molecule and permanent charges on the substrate atoms. Note that both these terms converge slowly with the distances $R_i$ and $r_{ij}$, and therefore have to be summed carefully. Also note that the second term is absent for adsorption on a graphene system, for which there are no permanent charges on the substrate; however, we actually find that the contribution from this second term is very small for the other cases too.

The contribution from Debye interactions to $E_{\text{ads}}$ is plotted in Fig. 3.12(b) (see the maroon bars). We see that while there are small differences in $E_D$ between the six systems, the overall contribution from Debye interactions is fairly negligible, and cannot explain the observed trends in $E_{\text{ads}}$.

Finally, we compute $E_K$, the contribution from Keesom interactions to $E_{\text{ads}}$; the Keesom interactions are the interactions between permanent moments/charges. The Keesom interaction includes the electrostatic interaction between permanent moment of the methanol molecule and the localized charges that appear on the substrate at interfaces. The contribution from Keesom interactions can be calculated using the formula

$$E_{\text{K}} = \sum_i \frac{q_i^{\text{perm}}}{4\pi\epsilon_0} \frac{\vec{\mu}^{\text{perm}} \cdot \mathbf{D}_i}{{D_i}^3} + \sum_j \frac{1}{4\pi\epsilon_0} \Big[ \frac{\vec{\mu}^{\text{perm}} \cdot \vec{\mu}_j^{\text{perm}}}{{d_j}^3} - 3 \frac{(\vec{\mu}^{\text{perm}} \cdot \mathbf{d_j})(\vec{\mu}_j^{\text{perm}} \cdot \mathbf{d_j})}{{d_j}^5} \Big], \tag{3.6}$$

where $i$ runs over all the atoms in the substrate and $j$ runs over all the periodic images of methanol molecules; $q_i^{\text{perm}}$ is the permanent charge on the substrate atom $i$, $\vec{\mu}_j^{\text{perm}}$ is the permanent dipole moment of the $j$th periodic image of methanol molecule, $\mathbf{D_i}$ is the vector connecting the central methanol dipole and the permanent charges on the substrate and $\mathbf{d_j}$ is the vector connecting the central methanol dipole and $j$th periodic image of methanol dipole. The first term of the right hand side of Eq. (3.6) denotes the electrostatic interaction between the permanent moment of the methanol molecule and the permanent charges on the substrate, while the second term of the right hand side of the Eq. (3.6) denotes the electrostatic interaction between the periodic images of the methanol molecule.

The values of $E_K$ for the six kinds of substrates are plotted in the last set of bars (orange online) in Fig. 3.12(b). For methanol on graphene, the Keesom interaction is zero as there are no permanent charges on the substrate. The Keesom interaction increases as we move on to h-BN, the armchair graphene-BN interface, the zigzag graphene-BN interface, mixed BCN and the triangular island structure. For adsorption on h-BN, we note that though there is no net dipole moment on the BN sheet, individual B-N bonds are ionic and hence polar in nature. Since the methanol molecule is not positioned symmetrically with respect to the BN sheet, but lies closer to a N atom [see Fig. 3.9(c)] there is an overall contribution to $E_K$ from the Coulomb interaction between the dipole moment of methanol and the permanent charges on the B and N atoms. If we compare the trends in the black bars (adsorption energy) and orange bars (Keesom energy) in Fig. 3.12(b), we can conclude that the progressively enhanced binding of methanol on the various kinds of interfaces comes almost entirely from Keesom interactions, i.e., from electrostatic interactions between the permanent dipole moment on the methanol molecule and charges induced at B-C and B-N interfaces on the substrates.

## 3.6 Conclusions

In summary, we have used density functional theory, incorporating van der Waals interactions, to study the adsorption of methanol on graphene, h-BN, an armchair C-BN interface, a zigzag C-BN interface, mixed BCN and a triangular graphene island within a BN matrix.

We have shown that striped zigzag and armchair C-BN interfaces are more favorable to form than mixed BCN structures. For small domain widths, zigzag C-BN interfaces are more energetically favorable, however our results suggest that for very large widths, armchair interfaces should become lower in energy. Though less favorable energetically than striped interfaces, small triangular graphene islands within a BN matrix are only slightly higher in energy, and therefore quite likely to form.

We find that the adsorption energy of a methanol molecule increases as the substrate is changed from graphene to h-BN to systems containing interfaces between graphene and BN. The strongest adsorption of methanol is observed at the apices of triangular inclusions of graphene situated within a BN matrixl with an enhancement in the adsorption energy of 65% relative to that on pristine graphene. This finding supports recent experimental reports that methanol binds more strongly on BN-doped carbon foam than on plain carbon foam.[48;49]

Further, we analyze the various contributions to binding by separating into different kinds of van der Waals interactions. We find out that although London dispersion interactions are responsible for the majority of the binding, their contribution is almost the same for all the kinds of substrates considered. Even though Debye interactions are larger for adsorption on h-BN than on graphene, and even larger for the C-BN interfaces and BCN, their contributions to binding are fairly small and can be largely neglected. We have shown that the enhancement in binding on the substrates containing C, B and N atoms arises almost entirely due to Keesom interactions, with the major component being the electrostatic interaction between permanent charges on the substrate and the permanent dipole moment of the methanol molecule. Our results can provide guidance for how to increase the binding of polar molecules on adsorbents. One possible area where such insights can possibly be applied is that of designing materials for thermal energy storage.

## Bibliography

[1] Y. Miyamoto, A. Rubio, M. L. Cohen, and S. G. Louie, "Chiral tubules of hexagonal $BC_2N$," *Physical Review B*, vol. 50, no. 7, p. 4976, 1994.

[2] O. Stephan, P. Ajayan, C. Colliex, P. Redlich, J. Lambert, P. Bernier, and P. Lefin, "Doping graphitic and carbon nanotube structures with boron and nitrogen," *Science*, vol. 266, no. 5191, pp. 1683–1685, 1994.

[3] L. Ci, L. Song, C. Jin, D. Jariwala, D. Wu, Y. Li, A. Srivastava, Z. Wang, K. Storr, L. Balicas, *et al.*, “Atomic layers of hybridized boron nitride and graphene domains,” *Nature materials*, vol. 9, no. 5, p. 430, 2010.

[4] N. Kumar, K. Moses, K. Pramoda, S. N. Shirodkar, A. K. Mishra, U. V. Waghmare, A. Sundaresan, and C. Rao, “Borocarbonitrides, $B_xC_yN_z$,” *Journal of Materials Chemistry A*, vol. 1, no. 19, pp. 5806–5821, 2013.

[5] J. Mannhart and D. Schlom, “Oxide interfaces an opportunity for electronics,” *Science*, vol. 327, no. 5973, pp. 1607–1611, 2010.

[6] H. Y. Hwang, Y. Iwasa, M. Kawasaki, B. Keimer, N. Nagaosa, and Y. Tokura, “Emergent phenomena at oxide interfaces,” *Nature materials*, vol. 11, no. 2, p. 103, 2012.

[7] A. Ohtomo and H. Hwang, “A high-mobility electron gas at the $LaAlO_3/SrTiO_3$ heterointerface,” *Nature*, vol. 427, no. 6973, p. 423, 2004.

[8] A. Brinkman, M. Huijben, M. Van Zalk, J. Huijben, U. Zeitler, J. Maan, W. G. van der Wiel, G. Rijnders, D. H. Blank, and H. Hilgenkamp, “Magnetic effects at the interface between non-magnetic oxides,” *Nature materials*, vol. 6, no. 7, p. 493, 2007.

[9] N. Reyren, S. Thiel, A. Caviglia, L. F. Kourkoutis, G. Hammerl, C. Richter, C. Schneider, T. Kopp, A.-S. Rüetschi, D. Jaccard, *et al.*, “Superconducting interfaces between insulating oxides,” *Science*, vol. 317, no. 5842, pp. 1196–1199, 2007.

[10] J. Pruneda, “Origin of half-semimetallicity induced at interfaces of C-BN heterostructures,” *Physical Review B*, vol. 81, no. 16, p. 161409, 2010.

[11] N. Bristowe, M. Stengel, P. Littlewood, E. Artacho, and J. Pruneda, “One-dimensional half-metallic interfaces of two-dimensional honeycomb insulators,” *Physical Review B*, vol. 88, no. 16, p. 161411, 2013.

[12] R. Martinez-Gordillo and M. Pruneda, “Polar discontinuities and 1D interfaces in monolayered materials,” *Progress in Surface Science*, vol. 90, no. 4, pp. 444–463, 2015.

[13] N. Bristowe, P. Ghosez, P. B. Littlewood, and E. Artacho, "The origin of two-dimensional electron gases at oxide interfaces: insights from theory," *Journal of Physics: Condensed Matter*, vol. 26, no. 14, p. 143201, 2014.

[14] A. Janotti, L. Bjaalie, L. Gordon, and C. Van de Walle, "Controlling the density of the two-dimensional electron gas at the $SrTiO_3/LaAlO_3$ interface," *Physical Review B*, vol. 86, no. 24, p. 241108, 2012.

[15] Y.-W. Son, M. L. Cohen, and S. G. Louie, "Energy gaps in graphene nanoribbons," *Physical review letters*, vol. 97, no. 21, p. 216803, 2006.

[16] M. Y. Han, B. Özyilmaz, Y. Zhang, and P. Kim, "Energy band-gap engineering of graphene nanoribbons," *Physical review letters*, vol. 98, no. 20, p. 206805, 2007.

[17] J. Park, J. Lee, L. Liu, K. W. Clark, C. Durand, C. Park, B. G. Sumpter, A. P. Baddorf, A. Mohsin, M. Yoon, *et al.*, "Spatially resolved one-dimensional boundary states in graphene–hexagonal boron nitride planar heterostructures," *Nature communications*, vol. 5, p. 5403, 2014.

[18] R. Drost, A. Uppstu, F. Schulz, S. K. Hafkmafklafkinen, M. Ervasti, A. Harju, and P. Liljeroth, "Electronic states at the graphene–hexagonal boron nitride zigzag interface," *Nano letters*, vol. 14, no. 9, pp. 5128–5132, 2014.

[19] G. S. Tschumper, "2 reliable electronic structure computations for weak noncovalent interactions in clusters," *Reviews in Computational Chemistry*, vol. 26, p. 39, 2009.

[20] F. L. Leite, C. C. Bueno, A. L. Da Róz, E. C. Ziemath, and O. N. Oliveira, "Theoretical models for surface forces and adhesion and their measurement using atomic force microscopy," *International journal of molecular sciences*, vol. 13, no. 10, pp. 12773–12856, 2012.

[21] P. H. Blustin, "A floating gaussian orbital calculation on argon hydrochloride (ar·

hcl)," *Theoretical Chemistry Accounts: Theory, Computation, and Modeling (Theoretica Chimica Acta)*, vol. 47, no. 3, pp. 249–257, 1978.

[22] W. Keesom, "The second viral coefficient for rigid spherical molecules, whose mutual attraction is equivalent to that of a quadruplet placed at their centre," *Proc. R. Acad. Sci*, vol. 18, pp. 636–646, 1915.

[23] A. A. Askalany, M. Salem, I. Ismail, A. H. H. Ali, and M. Morsy, "A review on adsorption cooling systems with adsorbent carbon," *Renewable and Sustainable Energy Reviews*, vol. 16, no. 1, pp. 493–500, 2012.

[24] L. Wang, R. Wang, and R. Oliveira, "A review on adsorption working pairs for refrigeration," *Renewable and sustainable energy reviews*, vol. 13, no. 3, pp. 518–534, 2009.

[25] D. Wang, Y. Li, D. Li, Y. Xia, and J. Zhang, "A review on adsorption refrigeration technology and adsorption deterioration in physical adsorption systems," *Renewable and Sustainable Energy Reviews*, vol. 14, no. 1, pp. 344–353, 2010.

[26] R. Paul, A. Voevodin, J. Hu, P. Amama, S. Ganguli, A. Roy, D. Zemlyanov, and T. S. Fisher, "Boron–carbon–nitrogen foam surfaces for thermal physisorption applications," *Thin Solid Films*, vol. 528, pp. 187–193, 2013.

[27] R. Paul, D. Zemlyanov, A. Voevodin, A. Roy, and T. Fisher, "Methanol wetting enthalpy on few-layer graphene decorated hierarchical carbon foam for cooling applications," *Thin Solid Films*, vol. 572, pp. 169–175, 2014.

[28] W. Kohn and L. J. Sham, "Self-consistent equations including exchange and correlation effects," *Physical review*, vol. 140, no. 4A, p. A1133, 1965.

[29] P. Hohenberg and W. Kohn, "Inhomogeneous electron gas," *Physical review*, vol. 136, no. 3B, p. B864, 1964.

[30] P. Giannozzi, S. Baroni, N. Bonini, M. Calandra, R. Car, C. Cavazzoni, D. Ceresoli, G. L. Chiarotti, M. Cococcioni, I. Dabo, *et al.*, "Quantum espresso: a modular and open-source software project for quantum simulations of materials," *Journal of physics: Condensed matter*, vol. 21, no. 39, p. 395502, 2009.

[31] J. P. Perdew, S. Kurth, A. Zupan, and P. Blaha, "Accurate density functional with correct formal properties: A step beyond the generalized gradient approximation," *Physical review letters*, vol. 82, no. 12, p. 2544, 1999.

[32] D. Vanderbilt, "Soft self-consistent pseudopotentials in a generalized eigenvalue formalism," *Physical review B*, vol. 41, no. 11, p. 7892, 1990.

[33] C. G. Broyden, J. Dennis Jr, and J. J. Moré, "On the local and superlinear convergence of quasi-newton methods," *IMA Journal of Applied Mathematics*, vol. 12, no. 3, pp. 223–245, 1973.

[34] R. Fletcher, "A new approach to variable metric algorithms," *The computer journal*, vol. 13, no. 3, pp. 317–322, 1970.

[35] D. Goldfarb, "A family of variable-metric methods derived by variational means," *Mathematics of computation*, vol. 24, no. 109, pp. 23–26, 1970.

[36] D. F. Shanno, "Conditioning of quasi-Newton methods for function minimization," *Mathematics of computation*, vol. 24, no. 111, pp. 647–656, 1970.

[37] H. J. Monkhorst and J. D. Pack, "Special points for Brillouin-zone integrations," *Physical review B*, vol. 13, no. 12, p. 5188, 1976.

[38] N. Marzari, D. Vanderbilt, A. De Vita, and M. Payne, "Thermal contraction and disordering of the al (110) surface," *Physical review letters*, vol. 82, no. 16, p. 3296, 1999.

[39] S. Grimme, "Semiempirical GGA-type density functional constructed with a long-range dispersion correction," *Journal of computational chemistry*, vol. 27, no. 15, pp. 1787–1799, 2006.

[40] W. M. Haynes, *CRC handbook of chemistry and physics.* CRC press, 2014.

[41] E. D. Glendening, C. R. Landis, and F. Weinhold, "NBO 6.0: Natural bond orbital analysis program," *Journal of computational chemistry*, vol. 34, no. 16, pp. 1429–1437, 2013.

[42] A. Fasolino, J. Los, and M. I. Katsnelson, "Intrinsic ripples in graphene," *Nature materials*, vol. 6, no. 11, p. 858, 2007.

[43] M. Corso, W. Auwärter, M. Muntwiler, A. Tamai, T. Greber, and J. Osterwalder, "Boron nitride nanomesh," *Science*, vol. 303, no. 5655, pp. 217–220, 2004.

[44] H. Nozaki and S. Itoh, "Structural stability of $BC_2N$," *Journal of Physics and Chemistry of Solids*, vol. 57, no. 1, pp. 41–49, 1996.

[45] Y. Gong, G. Shi, Z. Zhang, W. Zhou, J. Jung, W. Gao, L. Ma, Y. Yang, S. Yang, G. You, *et al.*, "Direct chemical conversion of graphene to boron-and nitrogen-and carbon-containing atomic layers," *Nature communications*, vol. 5, p. 3193, 2014.

[46] J. Pruneda, "Origin of half-semimetallicity induced at interfaces of C-BN heterostructures," *Physical Review B*, vol. 81, no. 16, p. 161409, 2010.

[47] T. Pankewitz and W. Klopper, "Ab initio modeling of methanol interaction with single-walled carbon nanotubes," *The Journal of Physical Chemistry C*, vol. 111, no. 51, pp. 18917–18926, 2007.

[48] R. Paul, A. A. Voevodin, D. Zemlyanov, A. K. Roy, and T. S. Fisher, "Microwave-assisted surface synthesis of a boron–carbon–nitrogen foam and its desorption enthalpy," *Advanced Functional Materials*, vol. 22, no. 17, pp. 3682–3690, 2012.

[49] R. Paul, A. Voevodin, J. Hu, P. Amama, S. Ganguli, A. Roy, D. Zemlyanov, and T. S. Fisher, "Boron–carbon–nitrogen foam surfaces for thermal physisorption applications," *Thin Solid Films*, vol. 528, pp. 187–193, 2013.

Chapter 4

# Structural and Dynamical Properties of $H_2O$ on Graphene Oxide

## 4.1 Introduction

In this chapter, we have studied the properties of water on graphene oxide. This system has relevance for a number of different possible applications, include fuel cells and filtration.

Fuel cells have several benefits over conventional combustion-based technologies currently used in many power plants and passenger vehicles. They can operate at higher efficiencies than combustion engines and can convert chemical energy to electrical energy with efficiencies of up to 60%. Moreover, fuel cells can eliminate pollution caused by burning fossil fuels.

There are several types of fuel cells available, and each has its advantages and limitations. Proton exchange membrane (PEM) fuel cells deliver high power density, and have a low weight to volume ratio as compared to other fuel cells; they also have a pollutant-free operation. PEM fuel cells are used primarily for transportation applications.

The electrolyte plays a key role in fuel cells. Ideally, it must permit transport of only the appropriate ions (protons) between the anode and cathode. To date, the most commonly used electrolyte in PEM fuel cells has been a material named nafion, due to its wide range of possible operating conditions and high conductivity. However, there are certain limitations of nafion: high cost, fuel crossover, and the water uptake capacity is also not so high. [1;2]

Recently, it has been reported that graphene oxide has a higher capacity for water uptake as compared to nafion.[3] Graphene oxide (GO) has an uptake capacity of 31.1% of water, as compared to 25.6% in nafion. Moreover, graphene oxide is much cheaper than nafion. In recent experiments, it has been shown that the conductivity of single layer graphene oxide increases almost linearly from $6 \times 10^{-7}$ $\mathrm{Scm}^{-1}$ at 55% relative humidity to $2 \times 10^{-4}$ $\mathrm{S\ cm}^{-1}$ at 90% relative humidity.[4;5]

Previous authors have shown that graphene oxide can be used as a nanosieve.[6] Though free-standing graphene oxide membranes were completely impermeable to gases, water vapour permeated through hydrophilic capillary channels that formed between the hydrophobic bare graphene areas of the graphene oxide sheet. The water transport was claimed to be ultrafast due to the absence of friction between the water molecules and the hydrophobic walls of the capillaries. In previous work, Wei *et al.* have studied water flow between graphene sheets, hydroxyl-functionalized graphene sheets and partially-functionalized graphene sheets, using classical molecular dynamics.[7] They concluded that fast transport was due to the formation of porous microstructures, rather than boundary slip processes.

It has also been suggested that suitably modified graphene oxide can be used for water splitting. Recently, it has been shown that as graphene oxide consists of large surface area with multiple functional groups, it can be used as an electron sink for metal-containing photocatalysts.[8] Unpaired $\pi$-electrons on graphene oxide can bond with the metal atoms of wide band gap materials such as $TiO_2$ or ZnO to extend the range of the photocatalysts. With appropriate tuning of oxygen functionalities, the conduction band minimumn(CBM) and valence band maximum (VBM) fall at energies that make the material suitable for oxygen and hydrogen generation.

In recent years there has been considerable interest in studying the structure and dynamical properties of water in one and two-dimensional configurations,[9;10] and how the properties of such water structures are different than three-dimensional bulk water. For example, it has been shown that for water inside carbon nanotubes of suitable diameter, a single chain of water molecules can form.[9] In bulk water, each water molecule forms, on average, nearly four hydrogen bonds, whereas, in such a one-dimensional (1D) chain, each molecule loses on average two of its four hydrogen bonds. Also it has been found that the average orientation of the water dipole with respect to the nanotube axis is 35°, i.e., water molecules are ordered more along the nanotube axis than in the directions perpendicular to the axis. The rotational motion of water dipole in these 1D chains is very slow due to the rigid hydrogen bonded network. It has a relaxation time constant of 0.3 ns. The diffusion coefficient of water in these 1D chains is $1.6 \times 10^{-17}$ cm$^2$/s.

A two-dimensional layer of water molecules forms [10] between two graphene sheets at a separation of 6.8 Å. The average number of hydrogen bonds per water molecule in these two dimensional network is 2.7. The rotational motion of water molecules in this layer is faster than in bulk water. It has relaxation time constant of 4.2 ps. The diffusion coefficient of this two dimensional water layer is $1.2 \times 10^{-5}$ cm$^2$/s.

In this chapter, we have used *ab initio* density functional theory and *ab initio* molecular dynamics to study the energetics, structural and dynamical properties of water on graphene oxide. As graphene oxide consists of patches of densely functionalized regions separated by bare graphene regions,[11;12] we look at how the structural properties over the bare graphene and functionalized graphene regions change with increasing water uptake. We have also computed dynamical properties such as the mean squared displacement and dipole orientational correlation for different water uptake and compare the results with water in one- and two-dimensional configurations.

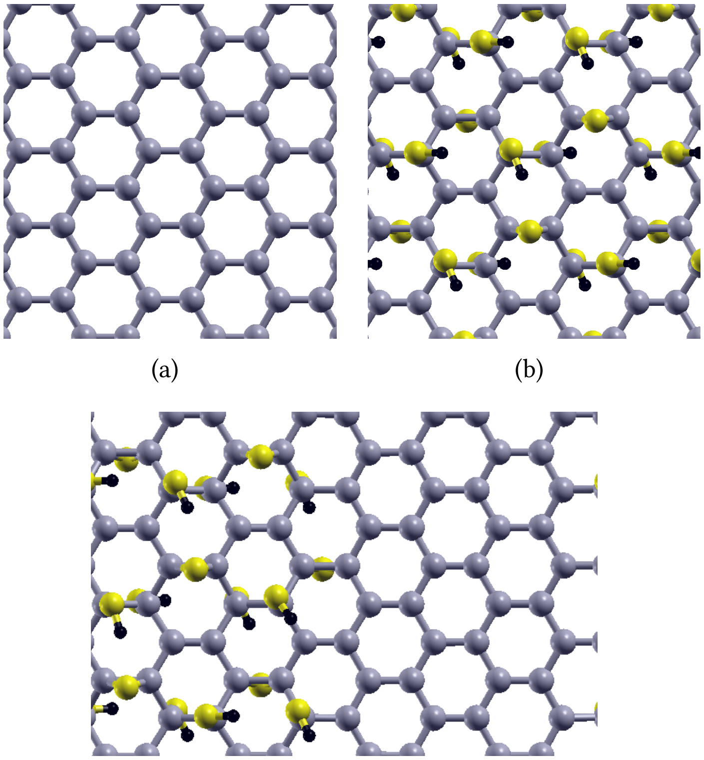

(a) (b) (c)

Figure 4.1: Top views of the three kinds of substrates considered (a) graphene (b) periodic graphene oxide and (c) zigzag graphene oxide. Color scheme for atomic spheres: C (gray), O (yellow), H (black).

## 4.2 Systems under study

To study the energetics, structural and dynamical properties of water we have considered three kinds of substrates: (a) bare graphene (b) graphene that is densely functionalized with epoxy and hydroxyl groups, that we refer to as periodic graphene oxide (PGO) and (c) graphene that contains patches of bare graphene and densely functionalized regions, separated by a zigzag interface, we will refer to this as zigzag graphene oxide (ZGO).

Fig. 4.1(a) shows the bare graphene substrate.

Our model for PGO [see Fig. 4.1(b)] is taken from the work of Wang *et al.* [13] It features a repeating motif of a triplet of functional groups (two -OH groups on one side of the graphene sheet and one -O- on the other side) attached to a sixfold carbon ring.

The PGO model is not very realistic, since it is known that in reality, graphene oxide consists of patches of bare graphene and patches that are densely covered with functional groups.[11;12] Accordingly, for a more realistic representation of graphene oxide, we use the ZGO model shown in Fig. 4.1(c).

For static density functional theory (DFT) calculations, we have used a (5 × 5) supercell of pristine graphene (containing 50 C atoms) and $2\sqrt{3} \times 2\sqrt{3}$ cell of PGO (containing 48 C atoms). For both static and dynamic calculations of water on ZGO, we have used a substrate unit cell that measures 17.06 Å × 14.78 Å, containing 96 C atoms. The vacuum region above the substrate was 20 Å.

For molecular dynamics calculations of $H_2O$ on ZGO, we have considered relative vapour pressures $P/P_0$ of 0.6, 0.7 and 0.8; here $P$ is the vapour pressure of the water molecules in the system, and $P_0$ is the saturation vapour pressure of bulk water. From Grand Canonical Monte Carlo (GCMC) simulations using classical potentials performed by our collaborators, we find that under these conditions, there are 36, 45 and 61 $H_2O$ molecules, respectively. in the simulation cell.

Calculations on bulk water are done using a cubical simulation cell with side 12.3 Å, containing 64 $H_2O$ molecules.

## 4.3 Computational Details

We have performed *ab initio* density functional theory (DFT)[14;15] and *ab initio* molecular dynamics (AIMD)[16–18] calculations to study the energetics, structural and dynamical properties of water on graphene oxide substrates. All the calculations have been performed using the Quantum ESPRESSO package.[19]

To describe the exchange-correlation interactions we have used the Becke-Lee-Yang-Parr (BLYP)[20;21] functional as it has been been reported to correctly predict the structural properties of water.[22–24] Electronic wavefunctions were expanded using a plane wave basis set with wavefunction and charge density cutoffs of 40 Ry and 400 Ry, respectively. Interactions between ionic cores and valence electrons were described using ultrasoft pseudopotentials.[25] Structural optimizations were performed using the Broyden-Fletcher-Goldfarb-Shanno (BFGS) scheme, until the Hellmann-Feynman forces on all the atoms being relaxed were less than 0.001 Ry/bohr.[26–29] Marzari-Vanderbilt cold smearing[30] with a width of 0.001 Ry was used for better convergence. The interaction of water with graphene oxide is in the range of energies typical of van der Waals interactions. It is well known that dispersion interactions are not incorporated in 'conventional' DFT. In order to have an accurate yet computationally affordable treatment of London dispersion interactions we have made use of the "DFT-D2" treatment introduced by Grimme.[31;32].

The adsorption energy, $E_{\mathrm{ads}}$, for $n$ $H_2O$ molecules on the substrate was calculated using

$$E_{\mathrm{ads}} = -(E_{\mathrm{substrate}+n\mathrm{H_2O}} - E_{\mathrm{substrate}} - nE_{\mathrm{H_2O}}), \tag{4.1}$$

where $E_{\mathrm{substrate}+n\mathrm{H_2O}}$, $E_{\mathrm{substrate}}$ and $E_{\mathrm{H_2O}}$ are the total energies for the (substrate + n $H_2O$) system, substrate and a $H_2O$ molecule in the gas phase, respectively. Note that according to this definition, $E_{ads}$ will contain contributions from both the binding between the water molecules and the substrate, and the water molecules with each other.

To calculate the structural and dynamical properties of water on a graphene oxide substrate, we have performed *ab initio* molecular dynamics simulations.[16–18] More specifically, we have performed Car-Parrinello molecular dynamics (CPMD)[33] as it is computationally cheaper than Born-Oppenheimer molecular dynamics (BOMD).[16]

As initial structures for the CPMD simulations, we have used configurations obtained by M. Rajasekaran and K.G. Ayappa, who performed Grand Canonical Monte Carlo (GCMC) simulations at different partial pressures. We have taken the initial structures from GCMC simulations performed for $P/P_0$ = 0.6, 0.7 and 0.8, where $P$ is the vapour pressure of the water molecules and $P_0$ is the saturation vapour pressure of bulk water.

Accordingly, the number of water molecules in the unit cconsidered for CPMD calculations for $P/P_0$ = 0.6, 0.7 and 0.8 was 36, 45 and 61 respectively. The molecular dynamics was performed at a constant temperature of 298 K using the Nosé-Hoover thermostat. We have used the velocity Verlet algorithm for the propagation of the electrons and ions. The total simulation time for each run was 50 ps, of which the first 10 ps of data was discarded when analyzing the data. The timestep for the MD calculations was 0.24 fs.

## 4.4 Results

### 4.4.1 Energetics of water on graphene and graphene oxide: statics

In this section we have studied the energetics of water on graphene and graphene oxide, using density functional theory.

#### Adsorption of a single water molecule on graphene and graphene oxide

First we have considered the adsorption of a single water molecule on graphene and graphene oxide substrate to compare their adsorption energies.

We have considered various possible initial orientations of water on graphene and we find that the most stable final configuration is the one-leg structure as shown in Figs. 4.2(a) and (b). In this most stable configuration, the calculated adsorption energy of a single water molecule on graphene is 0.071 eV. Previous theoretical calculations for a single $H_2O$ adsorbed on graphene obtained $E_{\text{ads}}$ to be in the range of 0.007 - 0.139 eV, depending upon the various exchange-correlations functionals used[34]. They have found the same one-leg configuration as the lowest energy geometry. By analyzing the different contributions to the adsorption energy, we find that the binding of water to graphene arises almost entirely from London dispersion interactions. In this favored adsorption geometry, the O-H bond of the water molecule is atop C and the oxygen atom of the water molecule is at 3.39 Å from graphene.

Similarly, the most stable configuration for the adsorption of a single water molecule

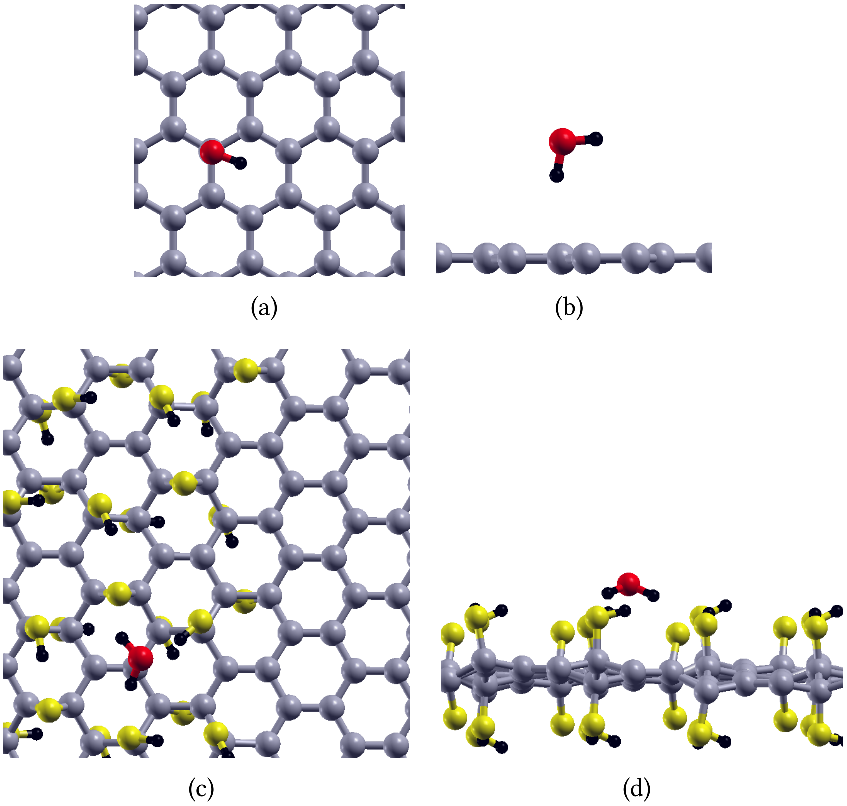
(a) (b)

(c) (d)

Figure 4.2: Top and side views of the optimal adsorption geometries for (a),(b) water on graphene; (c),(d) water on ZGO; Color scheme for atomic spheres: C-graphene (gray), O-substrate (yellow), O-water (red), H (black).

on ZGO is shown in Figs. 4.2 (c) and (d). We find that the water molecule prefers to bind on the functionalized part of the ZGO, rather than on the bare graphene part. In the most stable configuration, $E_{\text{ads}}$ on ZGO is 0.552 eV, which is a significant enhancement compared to the value on pristine graphene. In this most stable configuration, the water molecule forms three hydrogen bonds, one with an epoxy group and two with two hydroxyl groups.

In order to better understand the various contributions to the enhanced binding of water on ZGO, we will consider separately the binding of $H_2O$ to a $(5 \times 5)$ graphene supercell functionalized either with a single epoxy group or a single hydroxyl group. The most favored adsorption geometries for these cases are shown in Figs. 4.3 (a),(b) [for epoxy] and Figs. 4.3 (c),(d) [for hydroxyl].

For water on graphene, we had obtained $E_{ads} = 0.071$ eV. This increases for the epoxy

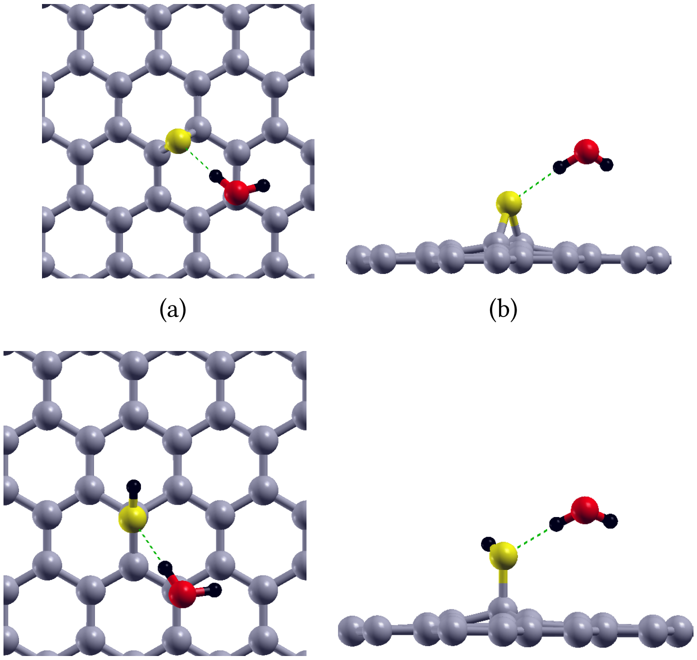

(a) (b)

(c) (d)

Figure 4.3: Top and side views of the optimal adsorption geometries for (a),(b) water on graphene functionalized with one epoxy group; (c),(d) water on graphene functionalized with one hydroxyl group. Color scheme for atomic spheres: C-graphene (gray), O-substrate (yellow), O-water (red), H (black). The dashed blue lines indicate hydrogen bonds.

group to 0.190 eV, and for the hydroxyl group to 0.252 eV. This is in accordance with the fact that the hydrogen bond length of water with epoxy is 1.99 Å and water with hydroxyl is 1.92 Å, and so the hydrogen bond strength of water-hydroxyl is more as compared to water-epoxy.

Let us recall that we had found above that the adsorption energy of a single water molecule on ZGO is 0.552 eV; here the water molecule forms one hydrogen bond with an epoxy group and two hydrogen bonds with hydroxyl groups. If we were to add separately the contributions from epoxy and hydroxyls the total summation is 0.694 eV which is 0.142 eV more than the value on ZGO. This may partly be because in ZGO, the epoxy and hydroxyl are anchored at fixed positions, and therefore the water molecule cannot simultaneously maximize its interaction strength with all three groups.

### 4.4.2 Hydrophobic and hydrophilic properties of graphene and graphene oxide substrates

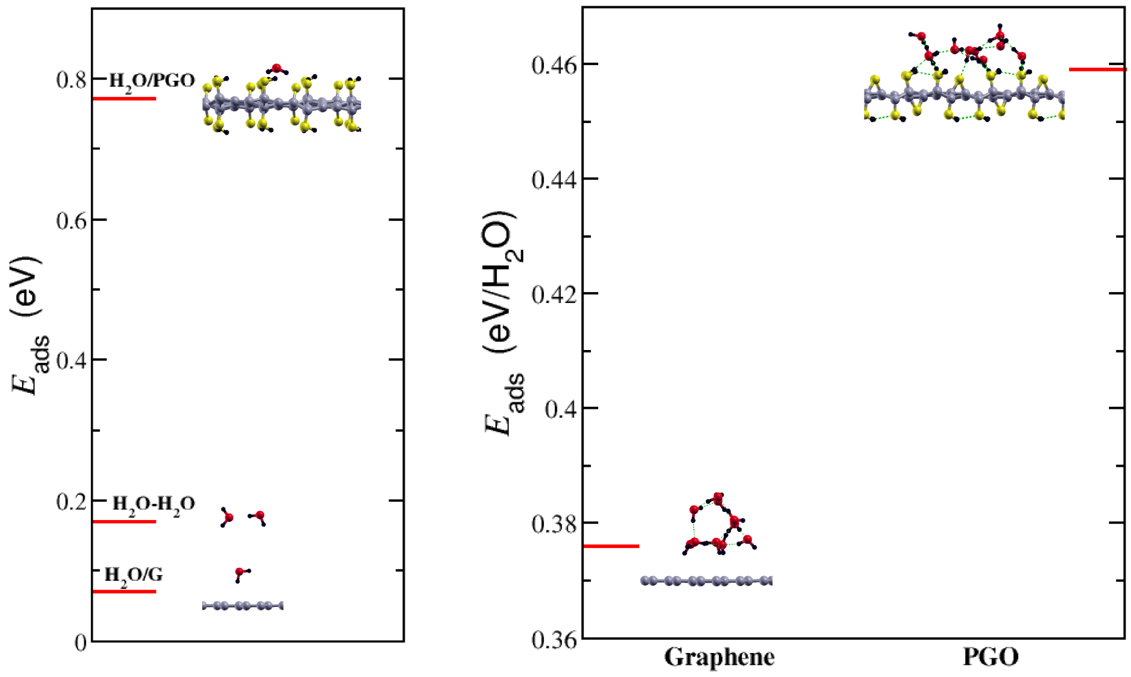

(a) (b)

Figure 4.4: (a) Interaction energies between the two molecules in a water-dimer, between a water molecule and graphene, and between a water molecule and PGO, in their equilibrium geometries.(b) Adsorption energies (per molecule) of a cluster of 10 water molecules on graphene and PGO. The red color bar in the graph denote the energy levels

Next, we want to investigate the hydrophobic and hydrophilic properties of graphene and graphene oxide. To do this, we have first computed the interaction energies of a water-dimer, a single water molecule on graphene and a single water molecule on graphene oxide. These are evaluated using the formula:

$$E_{int} = -(E_{1+2} - E_1 - E_2), \tag{4.2}$$

where $E_{1+2}$ is the total energy of the combined system 1 + 2 and $E_1$ and $E_2$ are the total energies of the isolated systems 1 and 2, respectively. The results for the interaction energies are shown in Fig. 4.4(a), We see that the binding of a water molecule on graphene is weaker than the binding between the two molecules in a water dimer, which in turn is significantly weaker than the binding of a water molecule on graphene oxide.

Next we have considered a water cluster consisting of 10 water molecules, and placed it on either graphene or periodic graphene oxide. The optimized geometries and their adsorption energies are shown in Fig. 4.4(b); the values of $E_{\text{ads}}$ have been calculated using Eq. (4.1), we recall that this definition includes contributions to binding between water molecules. We see that in the optimized geometry, the water molecules form a three dimensional (3D) cluster on graphene, whereas on PGO the geometry is more planar. Since [see panel(a)] the interaction between water molecules is stronger than the interaction of water molecules with graphene, it becomes energetically favorable for the water molecules to form a 3D cluster on graphene, and thus de-wet the substrate. In contrast, the interaction between water molecules is weaker than the interaction of water molecules with PGO [see panel(a)]. It therefore becomes favorable for the water molecules to maximize their contact area with the PGO substrate by forming a planar structure. In other words, graphene is hydrophobic, whereas (periodic – i.e., densely functionalized) graphene oxide is hydrophilic. The average spacing (difference in $z$ coordinate between the O atoms and the substrate C atoms) of the water molecules in contact with the substrate is 4.60 Å on graphene, and 4.19 Å on PGO.

### 4.4.3 Structural and dynamical properties of water on graphene oxide

From GCMC simulations, our collaborators M. Rajasekharan and K.G. Ayappa have observed that at lower coverages, water molecules bind preferentially on the functionalized part of zigzag graphene oxide. This is because of the fact that, as we saw above, $E_{\text{ads}}$ is significantly larger on functionalized portions of graphene than on bare portions of graphene. Figs. 4.5(a) and (b) show top and side views of the favored configuration at a low water loading, corresponding to 10 water molecules per unit cell; note that all the water molecules are over the hydrophilic (functionalized) regions of the ZGO. As the number of water molecules increases, a water bridge is observed to form between the functionalized part of the graphene and bare graphene region of graphene oxide. Fig. 4.5 shows, as an example, snapshots of the top and side views of the water bridges formed for the case when we have 61 water molecules present in the unit cell.

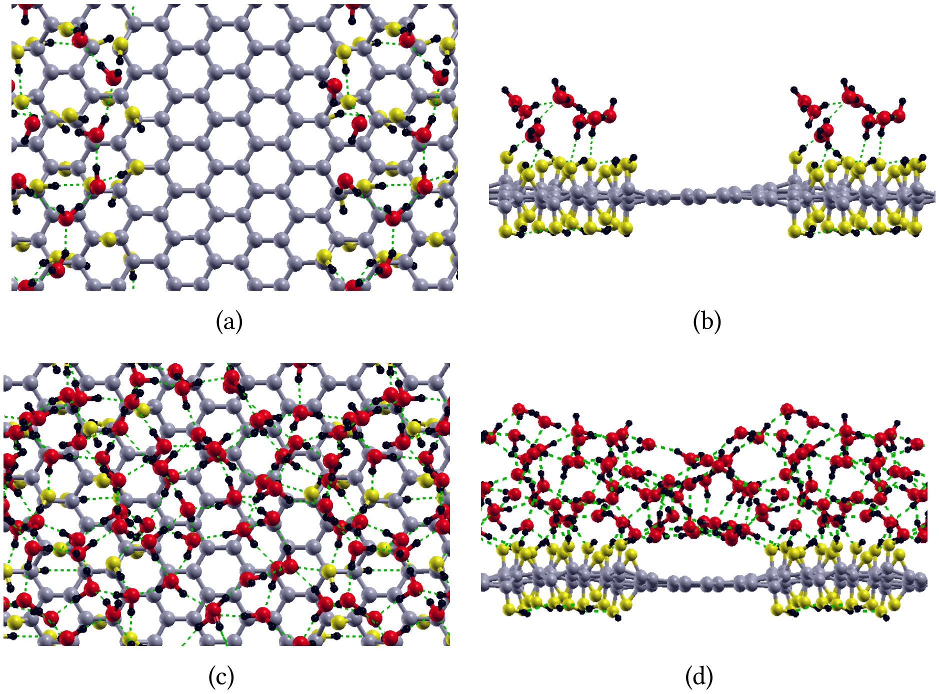
(a) (b) (c) (d)

Figure 4.5: Top and side views of examples of configurations (snapshots) for (a),(b) 10 $H_2O$ molecules and (c),(d) 61 $H_2O$ molecules on ZGO. Note the formation of a water bridge in (c),(d), which connects hydrophilic regions. Color scheme for atomic spheres: C-graphene (gray), O-substrate (yellow), O-water (red), H (black). The dashed blue lines indicate hydrogen bonds.

Taking the initial configurations obtained from GCMC simulations, we have performed Car-Parrinello molecular dynamics (CPMD) simulations for 36, 45 and 61 water molecules on ZGO. These results are compared with results on bulk water obtained using a unit cell containing 64 water molecules.

For the structural analysis, we have first computed the planar average density distribution of the water molecules along the $z$-direction i.e., along the surface normal direction. This is computed using the formula

$$\rho(z) = \frac{\langle N(Z+\Delta Z, Z)\rangle}{A\Delta Z}, \tag{4.3}$$

where $\rho(Z)$ is the planar average density at $Z$, $N$ is the number of water molecules, $\Delta Z$ is the width of the bin considered and $A$ is the surface area. Here $Z$ is the $z$-coordinate of the oxygen atom in the water molecule, and the distance is measured from the average of the z-coordinates of all the carbon atoms in the substrate.

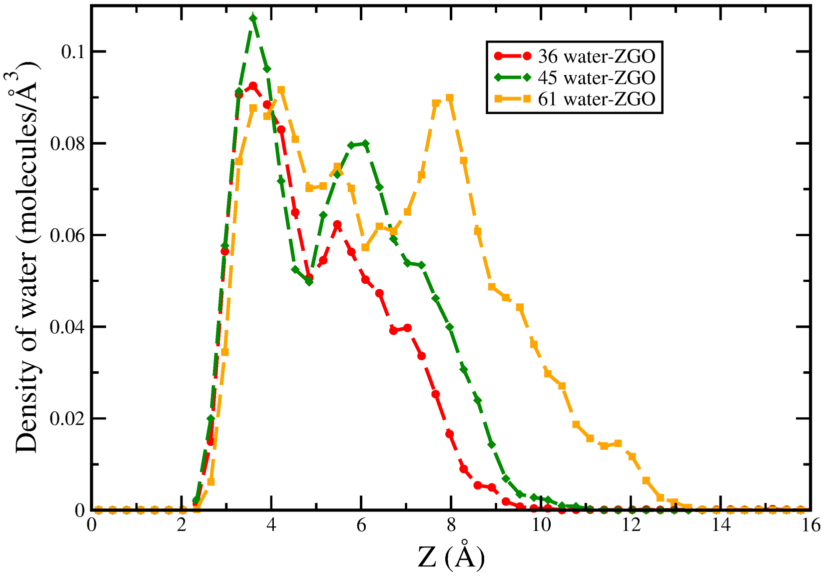

Figure 4.6: Planar average density distribution of water molecules at different loading along *z* direction. Red, green and yellow color represents the density distribution profiles for 36, 45 and 61 water molecules in the unit cell of ZGO.

In Fig. 4.6 we have plotted the planar average density distribution of 36, 45 and 61 water molecules on ZGO. For 36 water molecules (shown by the red curve), we see that the water molecules form a monolayer, separated by a distance of about 3.5 Å from the substrate. There is a smaller peak at about 5.5 Å, suggesting that a second monolayer might be incipiently forming. As we increase the number of water molecules the second layer of water molecules starts forming. For 45 water molecules (shown by the green curve) the second layer is centered at about 6 Å from the substrate. For 61 water molecules (shown by the yellow curve) we can see the second layer peak at around 5.5Å, and a distinct third layer peak at 8 Å. Thus increasing the number of water molecules results in increasing layering on ZGO.

We next want to investigate how the coordination number of water molecules on ZGO changes with increasing coverage of water. To do this, we first compute the radial

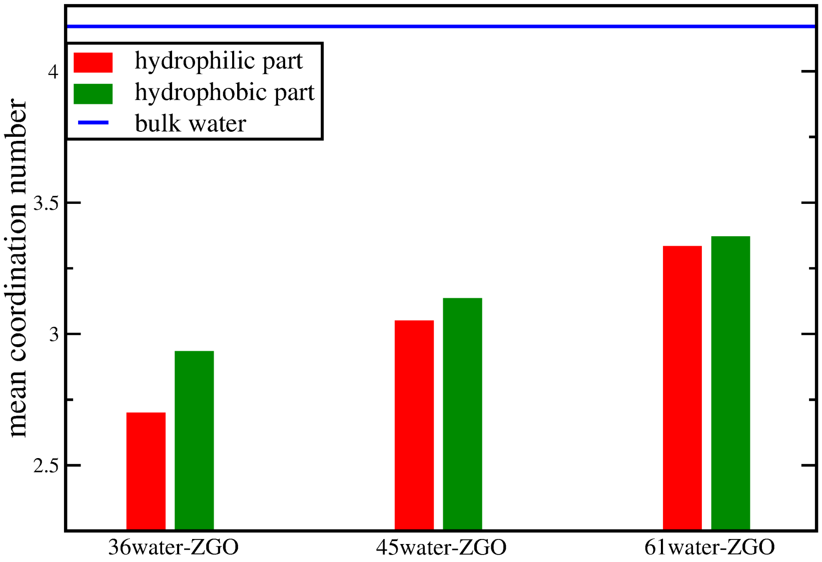

Figure 4.7: Mean coordination number of water molecules at different loading computed for hydrophilic and hydrophobic part separately. The hydrophilic part is shown by red bar and the hydrophobic part is shown by green bar and the mean coordination number of bulk water is shown by blue line.

distribution function $g(r)$ for bulk water. This gives information about the probability of finding a pair of water molecules a distance $r$ apart from one another, and is given by:[35]

$$g(r) = \frac{V}{N^2}\left\langle \sum_i \sum_{j\neq i} \delta(r - r_{ij}) \right\rangle, \tag{4.4}$$

where $N$ is the number of molecules in the system, $V$ is the volume, $i$ and $j$ run over all the water molecules in the system, and $r_{ij}$ is the distance between the relevant atoms in molecules $i$ and $j$; here we present only the results for the radial distribution function between pairs of oxygen atoms in different water molecules.

In Fig. 4.8 we have plotted our results for $g(r)$ for bulk water at 298 K. $r_{min}$, the position of the first minimum of $g(r)$ gives the radius up to which we should integrate to obtain the first coordination shell. We find this cutoff radius $r_{min}$ to be 3.26 Å which is in excellent agreement with previous theoretical results (which range from 3.27 Å to 3.55 Å, depending on the exchange-correlation functional used),[36] and is also in good agreement with an experimental result of 3.39 Å.

In Fig. 4.7, we have shown our results for the mean coordination number for the

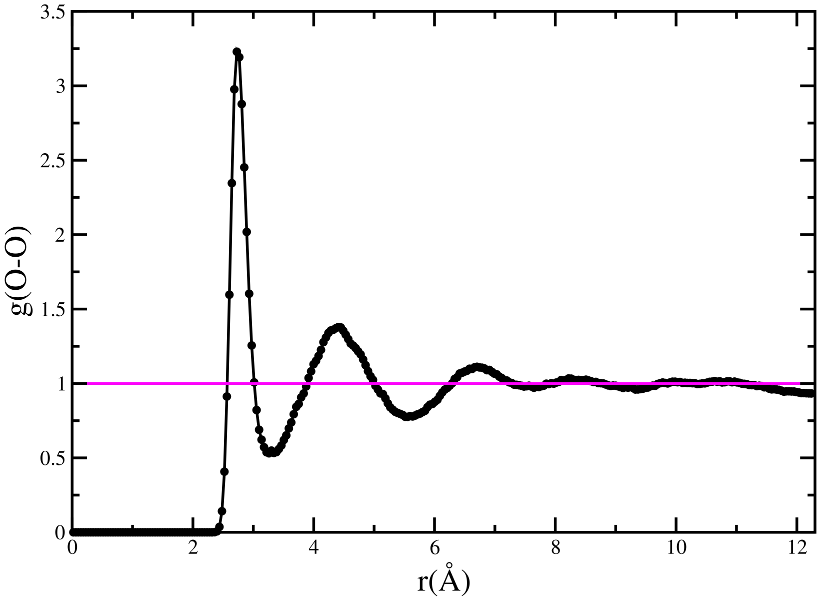

Figure 4.8: O-O radial distribution function of bulk water containing 64 water molecules. The first peak occurs at 2.74 Å the first minimum at $r_{min}$ = 3.26 Å, and the maximum value of $g$(O-O) is 3.23.

water molecules on ZGO, and seen how it changes, both as a function of coverage, and as we compare the hydrophobic and hydrophilic regions on the ZGO. We have separated out the results for the water molecules that are above the hydrophilic and hydrophobic parts of the ZGO substrate, these are defined as the functionalized and bare parts of the substrate, respectively. The results for the hydrophilic and hydrophobic parts are shown by red and green bars, respectively. To compare the results with bulk water, we have also computed the mean coordination number of bulk water shown by the horizontal blue line in Fig. 4.7; we find this value to be 4.26. This is again within the range of previously computed values, which range from 4.03 to 6.00, depending on the exchange-correlation functional used.[36]

We see that the mean coordination number of bulk water is higher than the mean coordination number of water molecules on ZGO at all coverages. As the coverage of water molecules increases, the mean coordination for both hydrophilic and hydrophobic region also increases, though it remains well below the value for bulk water. We see that the mean coordination number of the hydrophobic part is more than that in the hydrophilic part; this is in agreement with our earlier finding that water molecules prefer to form a 3D cluster in the hydrophobic part, but a 2D cluster in the hydrophilic part. However, as the coverage of the water molecule increases, the difference in mean coordination number between the hydrophilic and hydrophobic regions decreases markedly, becoming almost negligible at the highest coverage studied.

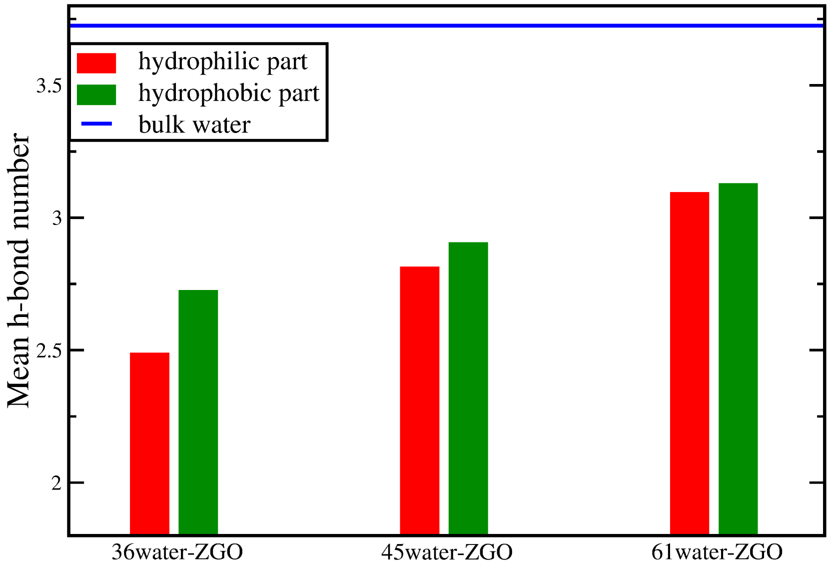

Figure 4.9: mean value of number of h-bonds between water molecules at different loading computed for hydrophilic and hydrophobic part separately. The hydrophilic part is shown by red bar and the hydrophobic part is shown by green bar and the mean coordination number of bulk water is shown by blue line.

Similarly, we have computed the mean number of hydrogen bonds between water molecules on ZGO, separately in the hydrophilic and hydrophobic part separately; these values are shown by the red and green bars in Fig. 4.9. Two water molecules are considred to be hydrogen bonded if the distance between the oxygen of two molecules are less than 3.5 Å distance of the oxygen of one molecule and hydrogen of the another molecule is less than 2.45 Å and the angle between O-H-O is more than 145°. The same criteria have been used in the previous literature for water systems using the BLYP functional.[9;10]

To compare the results with bulk water, we have also computed the corresponding value for the bulk water shown by the horizontal blue line in Fig. 4.9; we find this value to be 3.72. This is again within the range of previously computed values, which range from 3.20 to 3.82, depending on the exchange-correlation functional used.[36]

We see that the trends in the number of hydrogen bonds between the water molecules are similar to the trends in coordination number. The mean number of hydrogen bonds is always higher in bulk water than for water molecules on ZGO. As the coverage of water molecules increases, the mean number of hydrogen bonds increases,for both the hydrophilic and hydrophobic parts. Similar to coordination number the number of the hydrophilic part is more than the hydrophobic part and as the coverage of water molecules increases, the difference between the hydrophobic and hydrophilic part becomes negligible. By comparing Fig. 4.7 and Fig. 4.9, we note that though the trends are similar the coordination number and the mean number of hydrogen bonds are not exactly numerically equivalent, though they are close. Note that the number of hydrogen bonds formed depends upon the relative orientation of the water molecules, unlike the coordination number. For example, for the cell with 36 water molecules, the mean coordination numbers are 2.70 and 2.93 in the hydrophilic and hydrophobic parts, respectively, whereas the mean number of H bonds is 2.49 and 2.72, respectively. Thus, relative to the hydrophilic part, in the hydrophobic part the coordination number is enhanced by 7.4%, whereas the number of hydrogen bonds is enhanced by 10%.

These results for the mean values of the number of hydrogen bonds between water molecules on ZGO can be compared with previous values in the literature for water in low-dimensional forms. For a 1D water chain inside a carbon nanotube the value obtained was 2,[9] and for a 2D water layer between two graphene sheets the value obtained was 2.7.[10] It is interesting that the number we obtain for the water above the hydrophobic bare graphene area is so similar to that for water confined between two graphene sheets.

Next, we have studied how the water molecules orient over the hydrophilic and hydrophobic parts of the ZGO. To see this, we have plotted $\theta = \langle p_z/p \rangle$, where $\mathbf{p}$ is the dipole moment of the water molecule, and $p_z$ is its $z$-component. Note that in bulk water, there is no preferred direction of $\mathbf{p}$, and therefore $p_z = 0$ which would give $\theta = 90^\circ$. If $\theta > 90^\circ$, then on average the dipole moments point downward, similarly if $\theta < 90^\circ$, then on average the dipole moments point upward. The results for $\theta$, separately in the

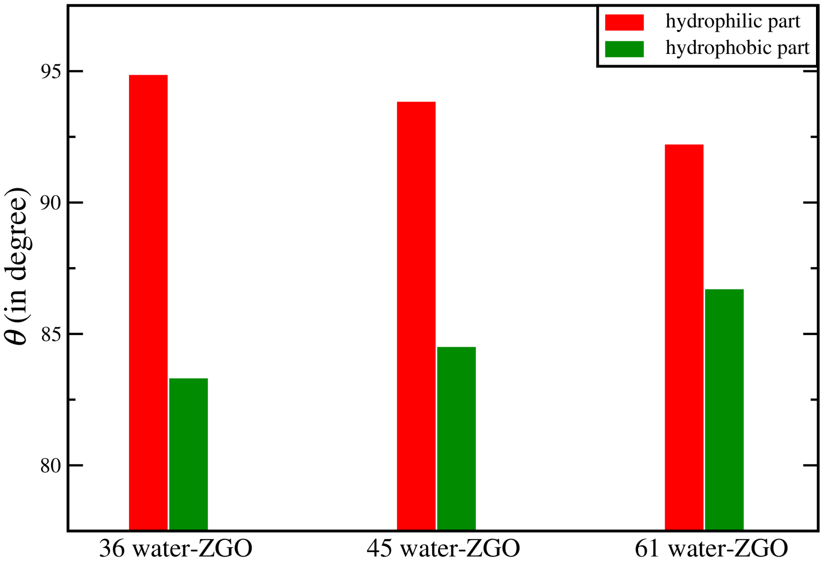

Figure 4.10: Change in orientation of water molecules with coverage. The bars show the angle $\theta$ made by the $z$ component of the dipole moment of the water molecules with the $z$-axis, computed for the hydrophilic and hydrophobic parts separately. The hydrophilic part is shown by the red bar and the hydrophobic part is shown by the green bar.

hydrophilic and hydrophobic regions of ZGO, are shown by the red and green bars in Fig. 4.10. First of all, we see that in the hydrophilic part, $\theta > 90°$, whereas in the hydrophilic part, $\theta < 90°$, though the differences from 90° are small. This implies that in the hydrophilic/hydrophobic parts, there is a slight tendency for the water molecules' dipole moments to point toward/away from the substrate. However, as the coverage of water molecules on ZGO increases, this tendency becomes less pronounced, approaching the situation for bulk water at higher coverages. We also note that this is quite different to what has been observed previously for a one-dimensional water chain confined within a carbon nanotube, where there is a strong orientational correlation, with the the average orientation of dipole with respect to nanotube axis forming an angle of 35°.[9]

We have studied the translational dynamics of interfacial water on the graphene oxide surface by analyzing the mean squared displacement (MSD). As we are interested in how fast the water molecules can move parallel to the substrate ($x - y$ plane), we have computed the two dimensional MSD, i.e., in the plane parallel to the substrate, using the formula:

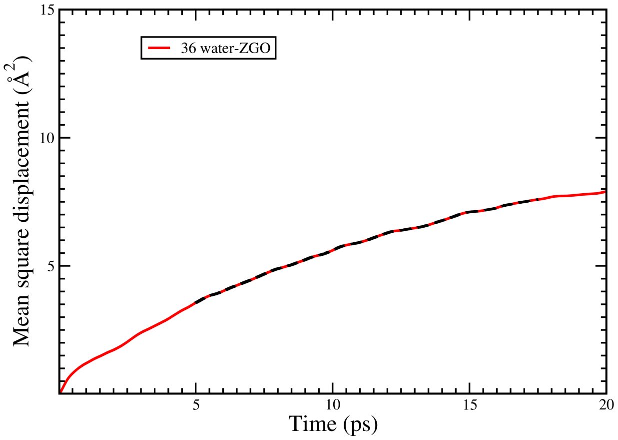

(a)

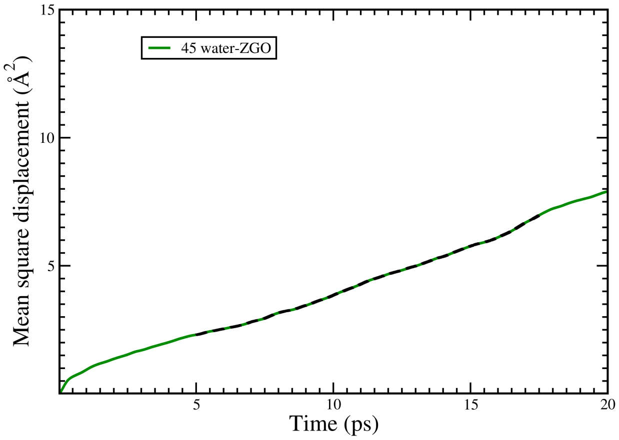

(b)

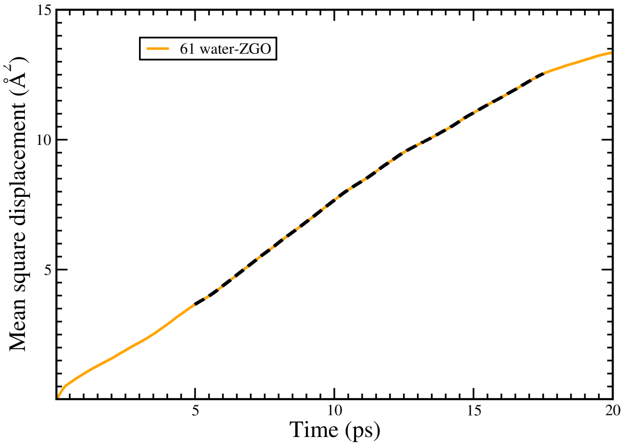

(c)

Figure 4.11: Mean squared displacement (MSD) of water molecules at different loading computed using shifted time origin for (a) 36 (b) 45 and (c) 61 water molecules on ZGO. The parts of the curves marked with black dashed lines indicate the diffusive regions used to compute the diffusion constant *D*.

$$\left\langle \Delta^2 \mathbf{r}(t) \right\rangle = \frac{1}{N} \sum_{i=1}^{N} \left\langle |\mathbf{r}_i(t) - \mathbf{r}_i(0)|^2 \right\rangle \tag{4.5}$$

where $\mathbf{r}_i(t)$ and $\mathbf{r}_i(0)$ are the position of the water molecules at times $t$ and 0 respectively. $N$ is the total number of molecules and $\left\langle \Delta^2 \mathbf{r}(\mathbf{t}) \right\rangle$ is the mean squared displacement. As we have computed two-dimensional MSD, here $\mathbf{r}$ is a two-dimensional vector composed of only the $x$ and $y$ coordinates of the water molecules.

One can then calculate the diffusion coefficient $D$ using the formula

$$D = \frac{1}{4t} \left\langle \Delta^2 \mathbf{r}(t) \right\rangle \tag{4.6}$$

where $D$ is the diffusion coefficient. To calculate the diffusion coefficient we have chosen the diffusive region of the MSD plot (shown by the regions denoted by blacked dashed lines in Fig. 4.11). Linear regressions to the dashed regions in the graphs in Fig. 4.11 gives the correlation coefficients $R^2$ of 0.9938, 0.9981 and 0.9977 for 36, 45 and 61 water molecules, respectively. Using Eq. (4.6), we obtain $D = 0.80 \times 10^{-5}$ cm$^2$/s for $P/P_0 = 0.6$ (36 water molecules), $0.93 \times 10^{-5}$ cm$^2$/s for $P/P_0 = 0.7$ (45 water molecules), and 1.80 $\times 10^{-5}$ cm$^2$/s for $P/P_0 = 0.8$ (61 water molecules). These values can be compared with previous values in the literature of $D = 1.6 \times 10^{-17}$ cm$^2$/s for a 1D water chain inside a carbon nanotube [9] and $1.2 \times 10^{-5}$ cm$^2$/s for a 2D water layer confined between two graphene sheets.[10]

Finally, we have studied the rotational motion of water on the graphene oxide surface by analyzing the dipole orientational correlation function for our MD simulations of water on ZGO. The rotational motion of water molecules is known to play a predominant role in the breaking of hydrogen bonds. It is therefore interesting to see how the rotational motion of water molecules changes with increasing water coverage.

The dipole orientational correlation function is defined as

$$C^{\alpha}(t) = \left\langle \sum_{i=1}^{N} (\mathbf{d}_i^{\mu}(t) \cdot \mathbf{d}_i^{\mu}(0)) \right\rangle, \tag{4.7}$$

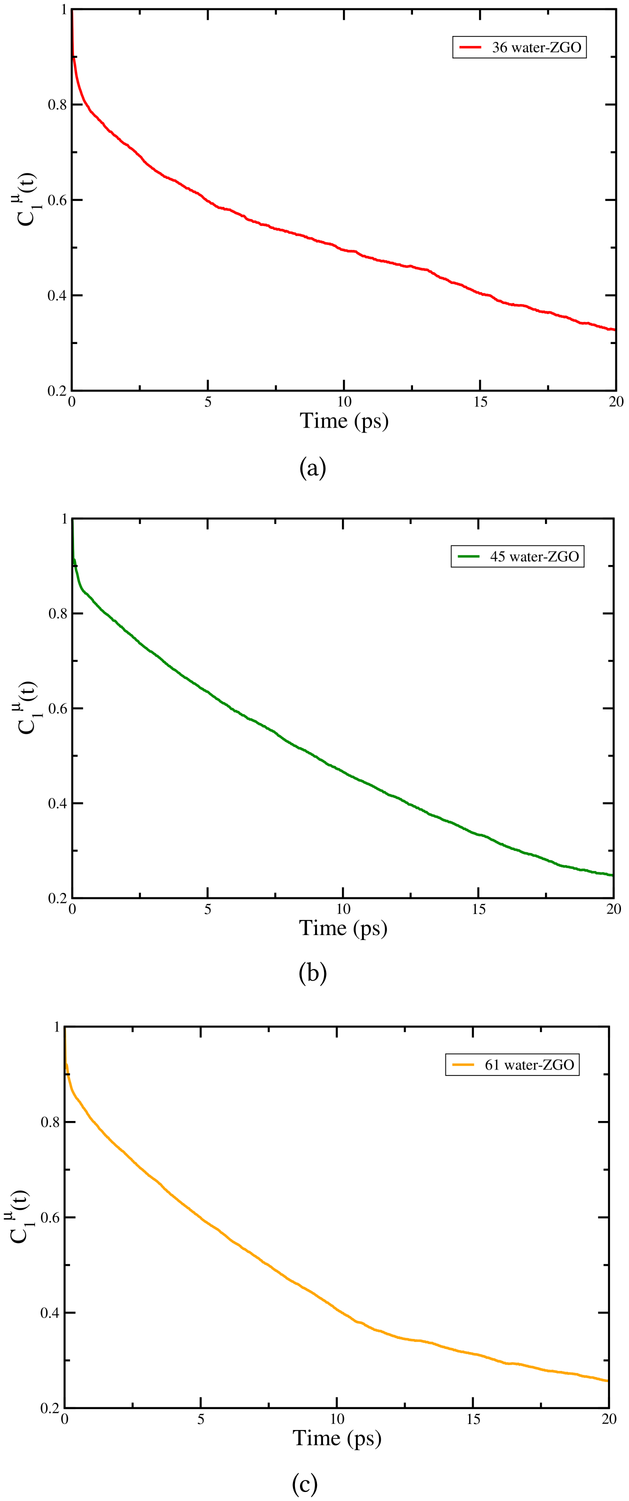

(a)

(b)

(c)

Figure 4.12: Dipole orientational autocorrelation of water molecules at different loading computed using shifted time origin for (a) 36 (b) 45 and (c) 61 water molecules on ZGO.

where $\mathbf{d}_i^{\mu}$ is the dipole moment unit vector of the water molecule $i$. Fig. 4.12(a), (b) and (c) show our results for $C^{\alpha}(t)$ for 36, 45 and 61 water molecules, respectively. These results

Table 4.1: Fitting parameters, obtained using Eq. (4.8), for dipole orientational correlation function for 36, 45 and 61 water molecules on ZGO, and the resulting values for relaxation time $\tau$.

| number of $H_2O$ molecules | $a_1$ | $\tau_1$ (ps) | $a_2$ | $\tau_2$ (ps) | $a_3$ | $\tau_3$ (ps) | $\tau$ (ps) |
|---|---|---|---|---|---|---|---|
| 36 | 0.4753 | 3.5323 | -0.9693 | 8.4484 | 1.4904 | 20.1703 | 41.97 |
| 45 | 0.0544 | 0.3272 | 0.5161 | 18.4042 | 0.4199 | 18.4378 | 18.42 |
| 61 | 0.3826 | 9.3719 | 0.1990 | 9.3758 | 0.1423 | 9.8101 | 9.56 |

are then fitted to a triple exponential function[37;38]:

$$C^{\alpha}(t) = a_0 e^{-t/\tau_0} + a_1 e^{-t/\tau_1} + a_2 e^{-t/\tau_2} + a_3 \tag{4.8}$$

where $a_0$, $a_1$, $a_2$ and $a_3$ are constants and $\tau_1$, $\tau_2$ and $\tau_3$ are fast, intermediate and slow relaxation times. The average relaxation time ($\tau$)is then calculated using the formula

$$\tau = \frac{a_1\tau_1 + a_2\tau_2}{a_1 + a_2} \tag{4.9}$$

Table 4.1 shows our results for the relaxation time of water molecules on ZGO. We observe that as the coverage of water molecules increases, the dipole relaxation time decreases. As a result, hydrogen bonds will break at a shorter time. These values can be compared with previously obtained values for the dipole relaxation time of 300 ps for a 1D water chain inside a carbon nanotube [9] and 4.2 ps for a 2D water layer between two graphene sheets.[10]

The systematic increase of the planar diffusion coefficient and decrease of dipole relaxation time with the number of water molecules indicates that increasing layering of water molecules on ZGO helps in-plane diffusion. This confirms the fact that near the interface, water molecules become more rigid, likely templated by the presence of the hydrophilic oxygen-derived functional groups on the graphene oxide. We speculate that this may be related to the fast proton-conducting character of graphene oxide by slowing the hydrogen-bond dynamics of water molecules and facilitating the formation of an ice-like backbone at the interface.

## 4.5 Conclusions

In this chapter, we have studied the energetics, structure and dynamics of water on graphene and graphene oxide, using density functional theory and Car-Parrinello molecular dynamics.

We find that the adsorption energy of a water molecule is greatly enhanced on regions of graphene oxide that are densely functionalized with epoxy and/or hydroxyl groups, compared to the very weak adsorption on graphene.

In practice, graphene oxide consists of patches of densely functionalized regions, separated by bare graphene regions. We have confirmed that the densely functionalized regions are hydrophilic, whereas the bare graphene regions are hydrophobic. On the former, a water cluster prefers to wet the surface, assuming a planar, two-dimensional morphology, whereas on the latter, it prefers to clump up into a three-dimensional morphology.

When water is deposited on graphene oxide, it initially wets the hydrophilic functionalized regions, and subsequently these regions are connected by the formation of water bridges that cross hydrophobic regions of the graphene oxide substrate. As the coverage of water increases, there is a layering of the water molecules, and the difference in the structure of the water over the hydrophobic and hydrophilic domains becomes less and less marked.

As the coverage of water is increased, both the average coordination of water molecules and the mean number of hydrogen bonds connecting water molecules increases. This is interesting because these are factors that will impact proton conductivity. Further, as the coverage of water is increased, the planar diffusion coefficient is increased and dipole relaxation time is decreased. This suggests that increasing layering of water molecules on graphene oxide helps in-plane diffusion. This also suggests that near the interface, water molecules become more rigid and ice-like, probably due to the presence of the hydrophilic oxygen-derived functional groups on the graphene oxide. We speculate that this may be related to the fast proton-conducting character of graphene oxide by slowing the hydrogen-bond dynamics of water molecules.

We have attempted to directly study the process of proton conductivity in water on graphene oxide, however these studies are at too preliminary a stage to be included in this thesis. It would be interesting to continue this work along those lines, as well as to induce a flow in the water molecules, so as to more directly study the rheology of water molecules on graphene oxide; to the best of our knowledge, such studies have so far been carried out only using classical potentials, and it would be interesting to explore whether the incorporation of quantum mechanical effects leads to any differences in results.

## Bibliography

[1] M. B. Satterfield, P. W. Majsztrik, H. Ota, J. B. Benziger, and A. B. Bocarsly, "Mechanical properties of nafion and titania/nafion composite membranes for polymer electrolyte membrane fuel cells," *Journal of Polymer Science Part B: Polymer Physics*, vol. 44, no. 16, pp. 2327–2345, 2006.

[2] N. H. Jalani, K. Dunn, and R. Datta, "Synthesis and characterization of nafion®-$MO_2$ (M= Zr, Si, Ti) nanocomposite membranes for higher temperature pem fuel cells," *Electrochimica Acta*, vol. 51, no. 3, pp. 553–560, 2005.

[3] T. Bayer, S. Bishop, M. Nishihara, K. Sasaki, and S. M. Lyth, "Characterization of a graphene oxide membrane fuel cell," *Journal of Power Sources*, vol. 272, pp. 239–247, 2014.

[4] K. Hatakeyama, M. R. Karim, C. Ogata, H. Tateishi, A. Funatsu, T. Taniguchi, M. Koinuma, S. Hayami, and Y. Matsumoto, "Proton conductivities of graphene oxide nanosheets: single, multilayer, and modified nanosheets," *Angewandte Chemie International Edition*, vol. 53, no. 27, pp. 6997–7000, 2014.

[5] M. R. Karim, K. Hatakeyama, T. Matsui, H. Takehira, T. Taniguchi, M. Koinuma, Y. Matsumoto, T. Akutagawa, T. Nakamura, S.-i. Noro, *et al.*, "Graphene oxide

nanosheet with high proton conductivity," *Journal of the American Chemical Society*, vol. 135, no. 22, pp. 8097–8100, 2013.

[6] R. Nair, H. Wu, P. Jayaram, I. Grigorieva, and A. Geim, "Unimpeded permeation of water through helium-leak–tight graphene-based membranes," *Science*, vol. 335, no. 6067, pp. 442–444, 2012.

[7] N. Wei, X. Peng, and Z. Xu, "Understanding water permeation in graphene oxide membranes," *ACS applied materials & interfaces*, vol. 6, no. 8, pp. 5877–5883, 2014.

[8] T.-F. Yeh, J. Cihlář, C.-Y. Chang, C. Cheng, and H. Teng, "Roles of graphene oxide in photocatalytic water splitting," *Materials Today*, vol. 16, no. 3, pp. 78–84, 2013.

[9] A. Bankura and A. Chandra, "Hydroxide ion can move faster than an excess proton through one-dimensional water chains in hydrophobic narrow pores," *The Journal of Physical Chemistry B*, vol. 116, no. 32, pp. 9744–9757, 2012.

[10] A. Bankura and A. Chandra, "Proton transfer through hydrogen bonds in two-dimensional water layers: A theoretical study based on ab initio and quantum-classical simulations," *The Journal of chemical physics*, vol. 142, no. 4, p. 044701, 2015.

[11] K. Erickson, R. Erni, Z. Lee, N. Alem, W. Gannett, and A. Zettl, "Determination of the local chemical structure of graphene oxide and reduced graphene oxide," *Advanced Materials*, vol. 22, no. 40, pp. 4467–4472, 2010.

[12] D. Pacilé, J. Meyer, A. F. Rodríguez, M. Papagno, C. Gomez-Navarro, R. Sundaram, M. Burghard, K. Kern, C. Carbone, and U. Kaiser, "Electronic properties and atomic structure of graphene oxide membranes," *Carbon*, vol. 49, no. 3, pp. 966–972, 2011.

[13] L. Wang, K. Lee, Y.-Y. Sun, M. Lucking, Z. Chen, J. J. Zhao, and S. B. Zhang, "Graphene oxide as an ideal substrate for hydrogen storage," *ACS nano*, vol. 3, no. 10, pp. 2995–3000, 2009.

[14] W. Kohn and L. J. Sham, “Self-consistent equations including exchange and correlation effects,” *Physical review*, vol. 140, no. 4A, p. A1133, 1965.

[15] P. Hohenberg and W. Kohn, “Inhomogeneous electron gas,” *Physical review*, vol. 136, no. 3B, p. B864, 1964.

[16] R. Car and M. Parrinello, “Unified approach for molecular dynamics and density-functional theory,” *Physical review letters*, vol. 55, no. 22, p. 2471, 1985.

[17] M. C. Payne, M. P. Teter, D. C. Allan, T. Arias, and J. Joannopoulos, “Iterative minimization techniques for ab initio total-energy calculations: molecular dynamics and conjugate gradients,” *Reviews of modern physics*, vol. 64, no. 4, p. 1045, 1992.

[18] M. E. Tuckerman, “Ab initio molecular dynamics: basic concepts, current trends and novel applications,” *Journal of Physics: Condensed Matter*, vol. 14, no. 50, p. R1297, 2002.

[19] P. Giannozzi, S. Baroni, N. Bonini, M. Calandra, R. Car, C. Cavazzoni, D. Ceresoli, G. L. Chiarotti, M. Cococcioni, I. Dabo, *et al.*, “QUANTUM ESPRESSO: a modular and open-source software project for quantum simulations of materials,” *Journal of physics: Condensed matter*, vol. 21, no. 39, p. 395502, 2009.

[20] A. D. Becke, “Density-functional exchange-energy approximation with correct asymptotic behavior,” *Physical review A*, vol. 38, no. 6, p. 3098, 1988.

[21] B. Miehlich, A. Savin, H. Stoll, and H. Preuss, “Results obtained with the correlation energy density functionals of becke and lee, yang and parr,” *Chemical Physics Letters*, vol. 157, no. 3, pp. 200–206, 1989.

[22] Z. Cao, Y. Peng, T. Yan, S. Li, A. Li, and G. A. Voth, “Mechanism of fast proton transport along one-dimensional water chains confined in carbon nanotubes,” *Journal of the American Chemical Society*, vol. 132, no. 33, pp. 11395–11397, 2010.

[23] C. Dellago, M. M. Naor, and G. Hummer, "Proton transport through water-filled carbon nanotubes," *Physical review letters*, vol. 90, no. 10, p. 105902, 2003.

[24] A. Bankura and A. Chandra, "Hydroxide ion can move faster than an excess proton through one-dimensional water chains in hydrophobic narrow pores," *The Journal of Physical Chemistry B*, vol. 116, no. 32, pp. 9744–9757, 2012.

[25] D. Vanderbilt, "Soft self-consistent pseudopotentials in a generalized eigenvalue formalism," *Physical review B*, vol. 41, no. 11, p. 7892, 1990.

[26] C. G. Broyden, J. Dennis Jr, and J. J. Moré, "On the local and superlinear convergence of quasi-newton methods," *IMA Journal of Applied Mathematics*, vol. 12, no. 3, pp. 223–245, 1973.

[27] R. Fletcher, "A new approach to variable metric algorithms," *The computer journal*, vol. 13, no. 3, pp. 317–322, 1970.

[28] D. Goldfarb, "A family of variable-metric methods derived by variational means," *Mathematics of computation*, vol. 24, no. 109, pp. 23–26, 1970.

[29] D. F. Shanno, "Conditioning of quasi-Newton methods for function minimization," *Mathematics of computation*, vol. 24, no. 111, pp. 647–656, 1970.

[30] N. Marzari, D. Vanderbilt, A. De Vita, and M. Payne, "Thermal contraction and disordering of the Al(110) surface," *Physical review letters*, vol. 82, no. 16, p. 3296, 1999.

[31] S. Grimme, "Accurate description of van der Waals complexes by density functional theory including empirical corrections," *Journal of computational chemistry*, vol. 25, no. 12, pp. 1463–1473, 2004.

[32] S. Grimme, "Semiempirical GGA-type density functional constructed with a long-range dispersion correction," *Journal of computational chemistry*, vol. 27, no. 15, pp. 1787–1799, 2006.

[33] R. Car and M. Parrinello, "Unified approach for molecular dynamics and density-functional theory," *Physical review letters*, vol. 55, no. 22, p. 2471, 1985.

[34] J. Ma, A. Michaelides, D. Alfe, L. Schimka, G. Kresse, and E. Wang, "Adsorption and diffusion of water on graphene from first principles," *Physical Review B*, vol. 84, no. 3, p. 033402, 2011.

[35] M. P. Allen and D. J. Tildesley, *Computer simulation of liquids.* Oxford university press, 2017.

[36] I.-C. Lin, A. P. Seitsonen, I. Tavernelli, and U. Rothlisberger, "Structure and dynamics of liquid water from ab initio molecular dynamics: Comparison of BLYP, PBE, and revPBE density functionals with and without van der Waals corrections," *Journal of chemical theory and computation*, vol. 8, no. 10, pp. 3902–3910, 2012.

[37] S. Senapati and M. L. Berkowitz, "Water structure and dynamics in phosphate fluorosurfactant based reverse micelle: A computer simulation study," *The Journal of chemical physics*, vol. 118, no. 4, pp. 1937–1944, 2003.

[38] A. Debnath, B. Mukherjee, K. Ayappa, P. K. Maiti, and S.-T. Lin, "Entropy and dynamics of water in hydration layers of a bilayer," *The Journal of chemical physics*, vol. 133, no. 17, p. 174704, 2010.

## Chapter 5

# Enhanced hydrogen evolution reactivity on $Mo_2C$-$Mo_2N$ composites

## 5.1 Introduction

The growing concern regarding pollution and global warming caused by fossil fuel combustion has led to an acceleration in research towards finding alternative renewable and sustainable energy sources.[1;2] Hydrogen is a promising alternative to fossil fuels as it has the highest energy density per unit mass, and water is the only byproduct formed when hydrogen is combusted in an engine or transformed into electricity in a fuel cell. Even though hydrogen is known to be the most abundant element in the universe, it is not easily found in its free molecular form on earth and needs to be extracted from hydrocarbons or through electrolysis of water.

The electrochemical water splitting is divided into two half cell reactions: hydrogen evolution reaction (HER) and oxygen evolution reaction (OER). HER is the cathodic reaction ($2H^+ + 2e^- \rightarrow H_2$) and OER is the anodic reaction ($2H_2O \rightarrow O_2 + 4H^+ + 4e^-$). Both HER and OER require catalysts to lower the electrochemical overpotential. Overpotential is the difference in potential between applied and thermodynamic potential of a given electrochemical reaction.

The state-of-the-art HER electrocatalysts are mainly Pt-based materials,[3–5] which are however, scarce and expensive. The search remains ongoing for alternative electrocatalysts based on more abundant or non-noble-metal-based materials. Earlier authors have proposed transition metal borides,[6;7] carbides,[8–12] nitrides,[13–15] chalcogenides,[16–21] and phosphides[22–25] as replacements for the Pt cathode catalyst for HER.

It has also been shown that doped systems can change the electronic structure and surface of the catalysts, thereby improving the heterogeneous electrocatalytic activity with respect to the pristine systems. Molybdenum phosphosulphide (MoP/S),[26] cobalt phosphosulphide (CoP/S),[27] S- and N-doped $Mo_2C$,[28] show enhanced HER activity. Recent studies[29] have also reported that $Mo_2C$-$Mo_2N$ composites synthesized using soybeans show remarkable HER activity. It has been shown that of the carbides, tungsten and molybdenum carbides are the best catalysts for HER; they are also better than all the nitrides.[9] However, their poor electrochemical stability is a concern.

Cathodic hydrogen evolution in acidic aqueous media occurs in two steps.[30;31] The first step is called the “discharge step”: an electron is transferred to the proton from the cathode surface to form a hydrogen atom that is still adsorbed on the cathode surface. This is also known as the Volmer reaction.

$$H^{+} + e^{-} \longrightarrow H \tag{5.1}$$

The second step is the electrochemical desorption step. In this step two hydrogen atoms form a hydrogen molecule and desorb from the surface. This could occur via two mechanisms. The first mechanism is the Heyrovsky reaction:

$$H + H^{+} + e^{-} \longrightarrow H_2, \tag{5.2}$$

while the second proposed mechanism is the Tafel recombination reaction:

$$H + H \longrightarrow H_2. \tag{5.3}$$

The Tafel slope, which is the slope of the plot of the applied overpotential vs. the $\log_{10}$

of the measured experimental current density, is generally used as an indicator for the efficiency of HER. At large overpotential, it is easy to produce hydrogen, however, a large overpotential signifies low energy efficiency. Therefore, it is desirable to obtain high HER and OER activities at low overpotentials.

Previous authors have shown that H adsorption energy on the catalyst is an excellent indicator for HER activity.[32] A good HER catalyst should have an optimum adsorption energy for H atom adsorption, that is neither too high nor too low; this is because of the competiton between the processes of H atom adsorption and removal. This is in line with the well known Sabatier's principle.[33] A volcano curve has been shown to describe the activity for the evolution of hydrogen as a function of the metal-H bonding strength.[32;34] The HER activity has been shown to increase upon increasing H adsorption energy, reach a maximum value and then decrease upon further increasing the adsorption strength. This is because strong or weak binding of the H atoms can lead to difficulties in either removing the product or adsorbing the reactant.

For similar reasons, previous authors have shown that a good catalyst should have $\Delta G$, the free energy for adsorbing atomic hydrogen, as close to zero as possible. This is because if hydrogen forms too weak or too strong a bond to the catalyst, then either the proton-electron-transfer step or the hydrogen-release step will not be efficient, thereby lowering the catalyst efficiency.[9]

In this chapter, we have used a combination of experiments (performed by our collaborators in the group of Prof. Ashok K Ganguli) and density functional theory calculations to study the effect of utilizing composite $Mo_2C$-$Mo_2N$ nanowires as HER catalysts. We find experimentally that though pristine $Mo_2C$ and $Mo_2N$ exhibit HER activity, N-rich composite systems show higher activity. This is confirmed theoretically by the trend for the Gibbs free energy of H adsorption obtained for the various systems as obtained from our calculations.

## 5.2 Experimental background

Ojha *et al.* have recently synthesized $Mo_2C$-$Mo_2N$ composite nanowires and investigated their HER activity.[35] The composite nanowires were synthesized by a reaction between aniline and ammonium molybdate to form anilinium ammonium molybdate complex in presence of graphene and reduced g-$C_3N_4$, followed by heating to a temperature of 750° C in nitrogen atmosphere. Three different composite structures were synthesized and labelled as CN100, CN50 and CN25; they were shown to have $Mo_2C$:$Mo_2N$ ratios of 1:0.67, 1:1.22 and 1:1.42. If one considers these composite system to have formula $Mo_2C_{1-x}N_x$, CN100, CN50 and CN25 would have $x$ = 0.40, 0.55 and 0.59, respectively.

Fig. 5.1(a) shows the electron microscopy images and elemental mapping of the $Mo_2C$-$Mo_2N$ composite structures. The elemental mapping confirms the presence of C, N and Mo atoms throughout the morphology, this suggests that the structure is not phase segregated and could be approximated to a doped $Mo_2C_{1-x}N_x$ system. Fig. 5.1(b) shows the current density as a function of the applied potential obtained for pristine $Mo_2C$ and $Mo_2N$, while Fig. 5.1(c) shows the same for the doped structures, CN100, CN50 and CN25. At an overpotential of 0.4 V, pristine $Mo_2C$ and $Mo_2N$ exhibit a current density of 35 mA/cm$^2$ and 6.5 mA/cm$^2$, respectively. However, the doped structures, interestingly, show an increased current density; samples CN100, CN50 and CN25 exhibit values of 128 mA/cm$^2$, 97 mA/cm$^2$ and 76 mA/cm$^2$, respectively.

Motivated by the experimental observation, we have performed density functional theory calculations on pristine $Mo_2C$, pristine $Mo_2N$ and doped $Mo_2C_{1-x}N_x$ surfaces to study the adsorption of hydrogen, as this is a known indicator for HER activity.

## 5.3 Systems under study

Pristine $Mo_2C$ is known to exist in an orthorhombic structure[36], while pristine $Mo_2N$ is known to exist in a tetragonal structure[37]. To study the effect of doping, we have first considered the bulk systems of $Mo_2C_{1-x}N_x$, with $x$ = 0, 0.25, 0.375, 0.5, 0.625, 0.75 and

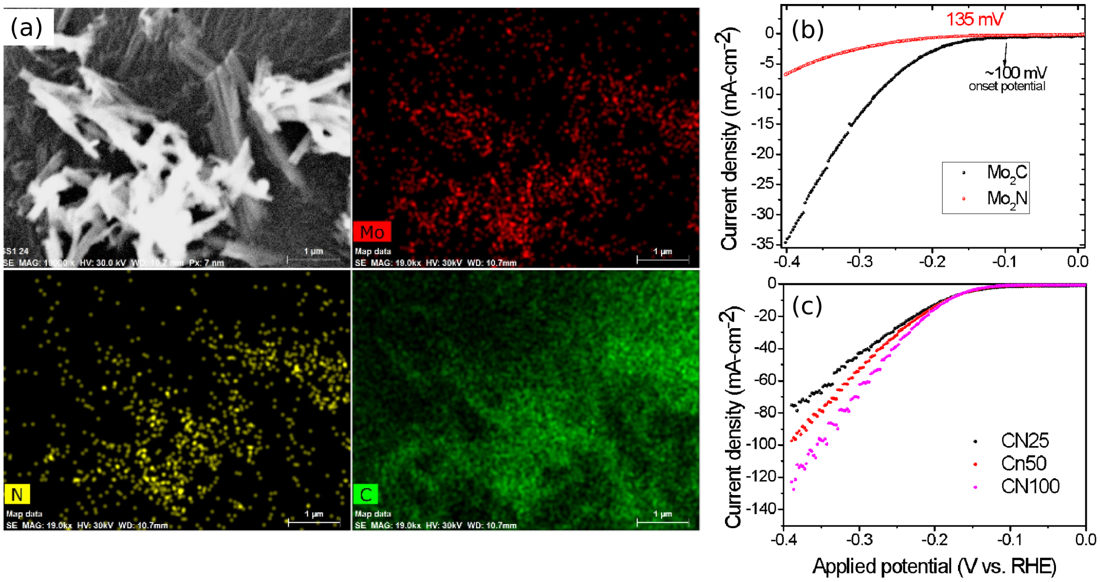

Figure 5.1: Results from experiments by Ojha *et al.*[35](a) Elemental mapping of $Mo_2C$-$Mo_2N$ composite nanowires shows the presence of Mo, C and N in the composite system (b) Current density of pure $Mo_2C$ and pure $Mo_2N$ at 0.4 V overpotential (c) Current density of doped $Mo_2C$-$Mo_2N$ compounds at 0.4 V overpotential

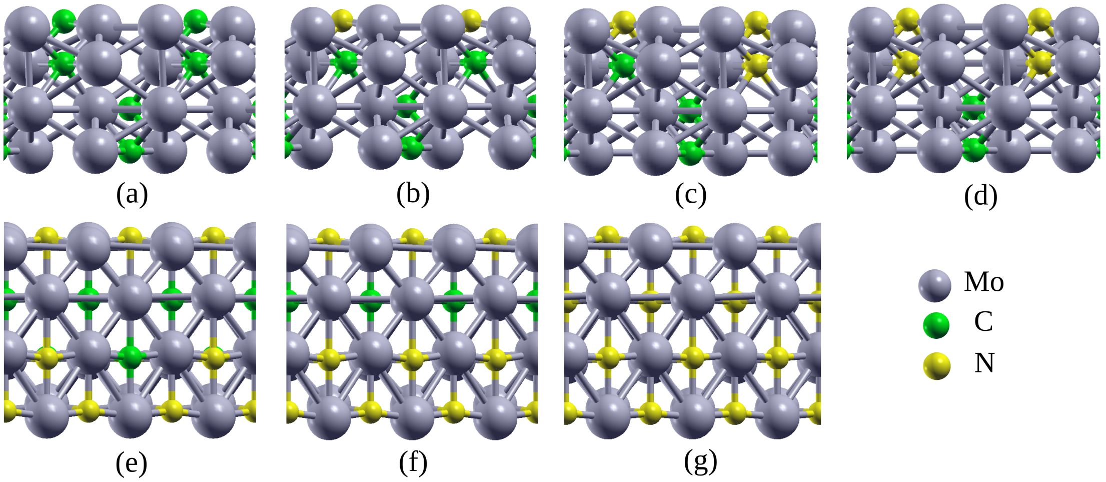

(a) (b) (c) (d)

(e) (f) (g)

Figure 5.2: Side views of surface slabs used for calculations on $Mo_2C_{1-x}N_x$ surfaces. For (a) $x = 0$, (b) $x = 0.25$, (c) $x = 0.375$ and (d) $x = 0.5$ we have considered the orthorhombic(100) surface and for (e) $x = 0.625$, (f) $x = 0.75$ and (g) $x = 1$ we have considered the tetragonal(001) surface. Note that the angle of view is slightly different in the upper and lower panels.

1, all in both orthorhombic and tetragonal structures, and determined the lowest energy structures for each value of $x$. In the doped structures, N/C atoms occupy C/N sites of the pristine $Mo_2C$ or $Mo_2N$ structures substitutionally. We find that the orthorhombic structure is favored over the tetragonal structure for $x = 0$, 0.25, 0.375 and 0.5, while the tetragonal structure is favored over the orthorhombic for $x$ = 0.625, 0.75 and 1. More details about these findings are given in the Results section further below.

We then considered possible low index surfaces for the two structures to identify the most stable surface, and find the (100) surface of orthorhombic structures and (001) surface of tetragonal structures to be most stable. The adsorption of a hydrogen atom was tested for different adsorption sites on these surfaces. For all surface calculations, we consider four atomic layers. The side views of the surface slabs used for pristine orthorhombic $Mo_2C$, pristine tetragonal $Mo_2N$ and the corresponding doped systems are shown in Fig. 5.2.

## 5.4 Computational Details

We have performed *ab initio* density functional theory (DFT),[38;39] and *ab initio* density functional perturbation theory (DFPT) calculations to study the adsorption of hydrogen atoms on $Mo_2C$, $Mo_2N$ and doped surfaces. A generalized gradient approximation of the RPBE[40] form was used to describe the exchange-correlation interactions. We have used a plane wave basis set for our calculations, with wavefunction and charge density cutoffs of 40 Ry and 400 Ry, respectively. Interactions between ionic cores and valence electrons were described using ultrasoft pseudopotentials[41]. The Brillouin zone (BZ) was sampled with a Monkhorst-Pack mesh[42] of $8 \times 8 \times 8$ for the bulk 1×1×1 orthorhombic unit cell of $Mo_2C$ and $8 \times 8 \times 4$ for the bulk 1×1×1 tetragonal unit cell of $Mo_2N$. We find that van der Waals interactions are critical to describe correctly the structural stability of $Mo_2C$ and $Mo_2N$ in their experimentally known structures. To include van der Waals interactions, we have used the DFT-D2 treatment introduced by Grimme[43].

For H adsorption, we have considered a supercell of the orthorhombic structure which is $1 \times 1 \times 2$ times the bulk primitive unit cell and a supercell of the tetragonal structure which is $2 \times 1 \times 1$ times the bulk primitive unit cell. For both orthorhombic and tetragonal structures, we have considered 0.25 ML coverage for H adsorption. For all surface calculations, 15 Å vacuum was considered in the surface normal direction to avoid interactions between periodic images. The top two layers and the adsorbed H atoms were allowed to relax while the bottom two layers were fixed at bulk spacing. Variable cell optimizations for bulk systems and structural relaxations for the surfaces were performed using the Broyden-Fletcher-Goldfarb-Shanno (BFGS) scheme until the Hellmann-Feynman forces were smaller than 0.001 Ry/Bohr. Marzari-Vanderbilt cold smearing[44] with a width of 0.001 Ry was used to aid convergence. We have also incorporated the dipole correction[45] for all surface energy calculations .

The adsorption energy of a hydrogen atom on $Mo_2C$, $Mo_2N$ and doped surfaces is calculated using the formula:

$$\Delta E_{\text{ads}} = -(E_{\text{subs+H}} - E_{\text{subs}} - \frac{1}{2}E_{\text{H}_2}), \tag{5.4}$$

where $E_{\text{subs+H}}$, $E_{\text{subs}}$ and $E_{\text{H}_2}$ are the total energies from DFT of a hydrogen atom adsorbed on the surface, the bare surface, and a hydrogen molecule in the gas phase, respectively. Note that these total energies are evaluated at the relaxed geometries of the corresponding systems. As HER activity has been shown to correlate with the Gibbs free energy of H adsorption,[5] we have computed the change in Gibbs free energy for a H atom adsorbed on $Mo_2C$, $Mo_2N$ and the doped surfaces. This is computed as

$$\Delta G = -\Delta E_{\text{ads}} + \Delta E_{\text{ZPE}} - T\Delta S_{\text{H}} \tag{5.5}$$

where $\Delta E_{\text{ads}}$ is the adsorption energy of hydrogen atom adsorbed on the substrate, $\Delta E_{\text{ZPE}}$ is the difference in zero point (vibrational) energy between the system consisting of the adsorbed H atom on the substrate and the bare substrate and the gas phase of hydrogen atom calculated from hydrogen molecule, $T$ is the temperature and $\Delta S_{\text{H}}$ is the entropy of adsorption. We exploit the fact that the vibrational entropy in the adsorbed phase is small, meaning the entropy of adsorption of 1/2 $H_2$ is $\Delta S_{\text{H}}$ = -1/2 $S^0_{H_2}$ where $S^0_{H_2}$ is the entropy of $H_2$ in the gas phase at standard conditions.

To explain the trends in the adsorption energy of a H atom on $Mo_2C_{1-x}N_x$ surfaces for different N concentrations $x$, we have used the $d$-band model suggested by Hammer and Nørskov.[46] According to this model, one can predict the reactivity of transition metal-based surfaces by looking at their $d$-band density of states, and extracting a single parameter called the $d$-band center, which is the weighted average of the $d$-band density of states. Accordingly, the $d$-band center $\epsilon_d$ is calculated from the Mo $d$-electron density of states using the equation:

$$\epsilon_d = \frac{\int_{-\infty}^{\infty} \epsilon g_d(\epsilon) d\epsilon}{\int_{-\infty}^{\infty} g_d(\epsilon) d\epsilon} \tag{5.6}$$

where $\epsilon$ is the energy and $g_d(\epsilon)$ is the $d$-band density of states at energy $\epsilon$. According to the $d$-band model, the higher in energy the $d$-band center is, the greater the reactivity. It has been shown, for example, that the higher in energy the $d$-band center is, the greater the magnitude of the adsorption energy, for a variety of adsorbates.[47]

We wish to quantify how the charge on Mo atoms changes with varying the C/N ratio. Partitioning the electronic charge density is an ambiguous procedure, with different prescriptions giving different answers. Here we have chosen to follow the procedure suggested by Bader, which makes use of the topological properties of the charge density.[48;49]

## 5.5 Results

### 5.5.1 Structure and energetics of pristine bulk $Mo_2C$ and $Mo_2N$

Pristine $Mo_2C$ and $Mo_2N$ are known to exist in several forms in nature. Among them, the most abundant forms are $\beta$-$Mo_2C$ which has an orthorhombic structure and $\beta$-$Mo_2N$ which has a tetragonal structure. X-ray diffraction patterns of the samples used in our experiments confirmed these structures for the pristine systems.

To validate our DFT calculations, we first consider bulk systems of $Mo_2C$ and $Mo_2N$

in both orthorhombic and tetragonal structures and compare energetics. Preliminary calculations were performed with and without van der Waals corrections, and we find that the inclusion of van der Waals interactions is critical to correctly stabilize the ground state structures of the pristine systems. We calculate the stability of the structures by the energy difference of the systems in both structures, $\Delta E = E_{\text{tet}} - E_{\text{ortho}}$. In the absence of any van der Waals corections, we find that $\Delta E = 0.901$ eV and 0.147 eV, respectively for pristine $Mo_2C$ and $Mo_2N$, which suggests that both systems energetically prefer to be in the orthorhombic structure. However, after incorporating van der Waals interactions in our calculations, we find $\Delta E = 0.811$ eV and $-0.042$ eV, respectively for pristine $Mo_2C$ and $Mo_2N$. This is now in agreement with what is experimentally measured for the structure of the respective pristine systems: $Mo_2C$ exists in an orthorhombic structure while $Mo_2N$ exists in a tetragonal structure. To the best of our knowledge, this is the first time that it has been shown that van der Waals interactions play a crucial role in determining the structural stability of bulk nitride structures.

Table 5.1: Lattice parameter of bulk $Mo_2C$ and $Mo_2N$

| System | Theory |  |  | Experiment[50;51] |  |  |
|---|---|---|---|---|---|---|
|  | $a$ Å | $b$ Å | $c$ Å | $a$ Å | $b$ Å | $c$ Å |
| bulk $Mo_2C$ | 6.078 | 5.250 | 4.729 | 6.037 | 5.204 | 4.732 |
| bulk $Mo_2N$ | 4.295 | 4.295 | 7.908 | 4.199 | 4.199 | 7.996 |

In Table 5.1 we compare the theoretical and experimental lattice parameters of bulk $Mo_2C$ and $Mo_2N$, and find them in good agreement.

### 5.5.2 Structure and energetics of bulk $Mo_2C_{1-x}N_x$ systems

In this section, we study how the energetics and lattice parameters change with composition for bulk $Mo_2C_{1-x}N_x$, for $x = 0$, 0.25, 0.375, 0.5, 0.625, 0.75 and 1.0. For all systems, we consider both orthorhombic and tetragonal structures, all with and without van der Waals correction. In Fig. 5.3, we show $\Delta E$ as a function of $x$. We see again (see blue symbols) that when no van der Waals interactions are included, all systems considered

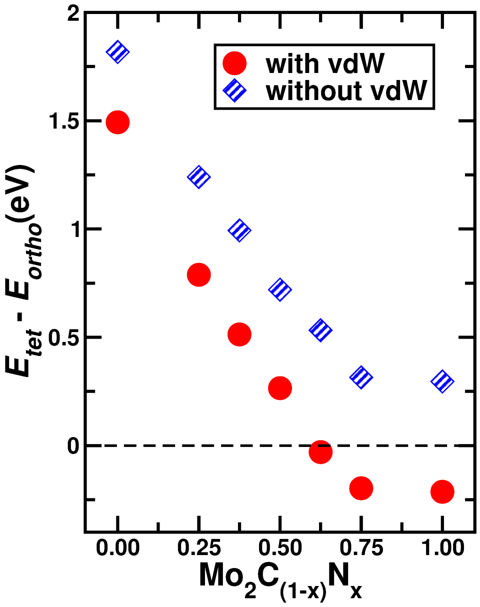

Figure 5.3: Difference in total energy between tetragonal and orthorhombic structures, for bulk $Mo_2C_{1-x}N_x$, a a function of N concentration $x$. Red circles and blue diamonds indicate results with and without van der Waals interactions incorporated, respectively. Note that a positive/negative value indicates the orthorhombic/tetragonal structure is favored.

seem to energetically prefer the orthorhombic structure. However, after the inclusion of van der Waals corrections (see red symbols), we see a shift in the behavior. The energy difference between the structures decreases steadily as the concentration of N atoms in the system increases and crosses $y = 0$ after $x > 0.5$, i.e., the orthorhombic structure is preferred for systems with $x$ = 0, 0.25, 0.375 and 0.5, whereas the tetragonal structure is preferred for systems with $x$ = 0.625, 0.75 and 1.

Next, to investigate how the incorporation of van der Waals interactions impacts the structure, we have plotted the optimized lattice parameters for all systems calculated with and without van der Waals correction. In Figs. 5.4(a)–(c) we show the lattice parameters $a$, $b$ and $c$, obtained for $Mo_2C_{1-x}N_x$, with different values of $x$, in the orthorhombic structure and in Figs. 5.4(e)–(g) we show the lattice parameters for $Mo_2C_{1-x}N_x$ for different values of $x$, in the tetragonal structure. In Figs. 5.4(d) and (h), we show the volume of a unit cell in the orthorhombic and tetragonal structures, respectively. We see that van der Waals interactions have a negligible effect on the lattice parameters in the orthorhombic

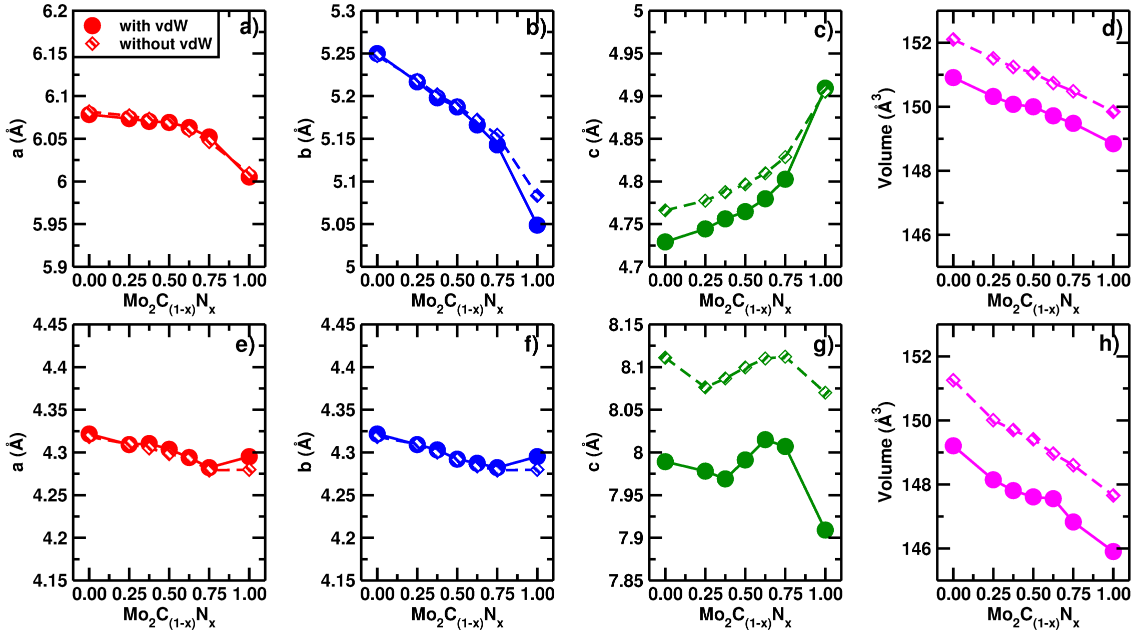

Figure 5.4: Changes in lattice parameters with N concentration $x$ in bulk $Mo_2C_{1-x}N_x$ structures. (a)-(c) Change in lattice parameters with $x$ for orthorhombic structure, (d) change in volume with $x$ for orthorhombic structure, (e)-(g) change in lattice parameters with $x$ for tetragonal structure. and (h) Change in volume with $x$ for tetragonal structure. Filled circles and open diamonds are results with and without van der Waals interactions incorporated.

structure, however, in the tetragonal structure, these interactions lead to a significant decrease in the $c$ parameter. This may explain why the energetics shift for systems with $x$ = 0.625, 0.75 and 1, to prefer the tetragonal structure over the orthorhombic structure.

### 5.5.3 Structural stability of different $Mo_2C$ and $Mo_2N$ surfaces

We now consider the low index (100), (010) and (001) surfaces for pristine $Mo_2C$ and $Mo_2N$, to compare energetics and identify the lowest energy surface. For each case, we considered six atomic layers and 15 Å vacuum along the surface normal direction. The top two and bottom two layers were allowed to relax, while the two layers in the center of the slab were fixed at bulk spacing. We note that the $Mo_2C(001)$ surface is polar in nature, and the dipole correction was included to nullify the interactions between the periodic images.

The surface energy was calculated using the formula $\sigma_t + \sigma_b = E_{surface} - n \times E_{bulk}$,

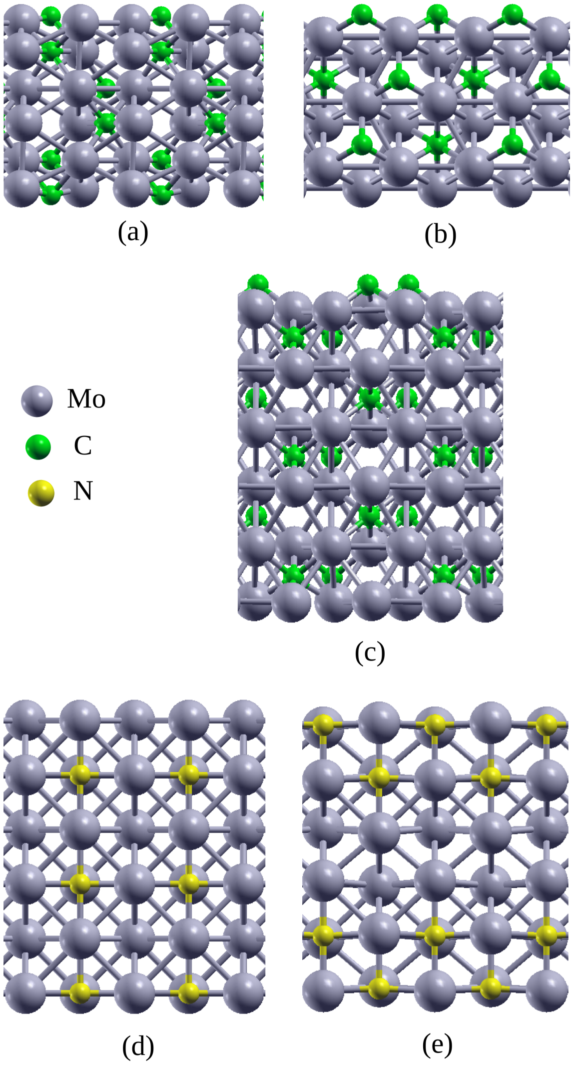

(a) (b) (c) (d) (e)

Figure 5.5: (a)-(c) Side view of (100), (010) and (001) surface slabs for $Mo_2C$ in orthorhombic structure. (d)-(e) Side view of (100) and (001) surface slabs for $Mo_2N$ in tetragonal structure.

where $E_{surface}$ and $E_{bulk}$ are the total energies of the surface and bulk structure, respectively and $n$ is the number of bulk units contained in the surface slab. Note that this is the sum of the surface energies of the top and bottom surfaces created in the slab by carving it out of the infinite bulk. For a polar surface, the surface energies of the top and bottom surfaces are different whereas for the non-polar surfaces both surfaces have same energy. Note also that even though we have considered six atomic layers in each case, there was a different number of atoms in the $1 \times 1$ surface unit cell considered for each surface. To enable easy comparison, we report here the surface energy per formula unit, where a formula unit consists of two Mo atoms and one C/N atom.

For the (100), (010) and (001) $Mo_2C$ surfaces, we calculate $\sigma_t+\sigma_b$ to be 0.766 eV/formula unit, 0.955 eV/formula unit and 1.024 eV/formula unit, respectively. Thus, we find that the $Mo_2C(100)$ surface has the lowest surface energy, and for all further calculations for $Mo_2C_{1-x}N_x$ with orthorhombic structure, we consider this surface.

For the (100) and (001) $Mo_2N$ surfaces, we calculate $\sigma_t+\sigma_b$ to be 0.489 eV/formula unit and 0.466 eV/formula unit, respectively. We see that the (001) surface is slightly lower in energy than the (100) surface. For all further calculations for $Mo_2C_{1-x}N_x$ with tetragonal structure, we consider the (001) surface.

### 5.5.4 Adsorption of H on $Mo_2C_{1-x}N_x$ surfaces

We now consider the adsorption of an atomic H on pristine $Mo_2C$, pristine $Mo_2N$ and doped $Mo_2C_{1-x}N_x$ surfaces. For $x$ = 0, 0.25, 0.375 and 0.50, the system prefers the orthorhombic structure and we consider the (100) surface, while for $x$ = 0.625, 0.75 and 1.00, the system prefers the tetragonal structure and we consider the (001) surface.

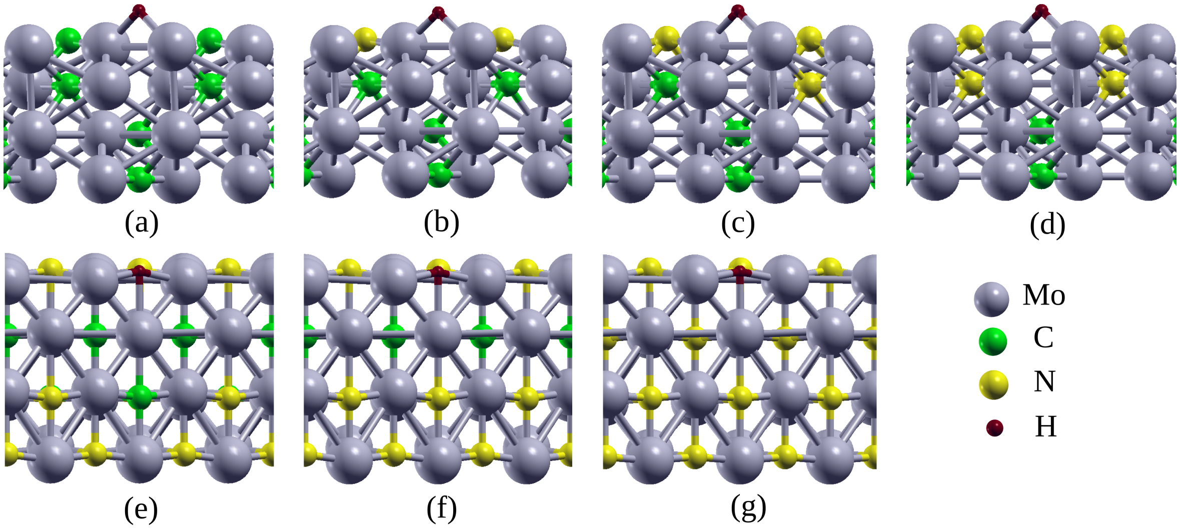

Figure 5.6: Side views of H atom adsorbed on $Mo_2C_{1-x}N_x$ surfaces. For $x$ = 0, 0.25, 0.375 and 0.5 we have considered the orthorhombic(100) surface and for $x$ = 0.625, 0.75 and 1 we have considered the tetragonal(001) surface. Note that the angle of view is different in the top and bottom rows; in all cases H atoms are adsorbed in a hollow site.

For each value of $x$, we have considered several possible dopant positions, and different adsorption sites for the adsorption of hydrogen on the surfaces. In Fig. 5.6, we show the lowest energy configurations obtained for every $x$. For all $Mo_2C_{1-x}N_x$ systems in both the orthorhombic and tetragonal structures, we find that H adsorbs on the hollow site on the surface, binding to two surface Mo atoms.

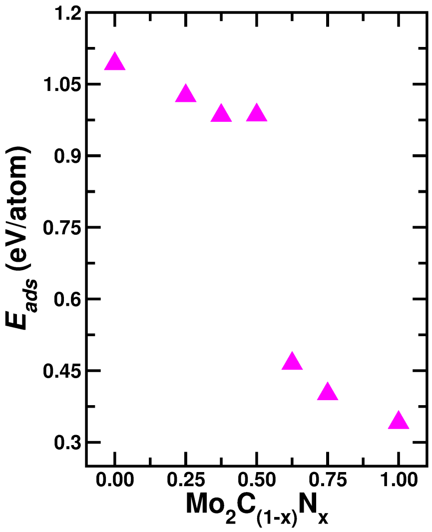

Figure 5.7: Adsorption energy of single H atom on $Mo_2C_{1-x}N_x$. With increasing N concentration, adsorption energy decreases. For $x = 0$, 0.25, 0.375 and 0.5 we have taken orthorhombic structure and for $x = 0.625$, 0.75 and 1,we have taken tetragonal structure.

In Fig. 5.7, we show the adsorption energy of H on the surface as a function of $x$. As the percentage of N in the system, $x$, increases, we find that the adsorption energy $E_{ads}$ decreases. After $x = 0.5$, we observe a significant drop in the adsorption energy due to the structural change from orthorhombic to tetragonal forms.

In order to understand the trends in adsorption energies with changing N concentration $x$ in $Mo_2C_{1-x}N_x$ systems, we first look at how the charge on Mo changes with $x$. In Fig. 5.8(a) we have plotted the average charge on the surface Mo atoms as a function of $x$. We find that the Mo atoms are positively charged, and we see that as the N concentration $x$ increases, the charge $q$(Mo) on Mo atoms also increases (becomes more positive). This is because the electronegativity of C is 2.55, whereas that of N is 3.04. Therefore, as the concentration of N atoms increases, the more electronegative N atoms withdraw more electrons from the Mo atoms, leaving them with a larger positive charge.

In a recent paper, Liu *et al.*[52] studied molybdenum carbide systems, where they varied the Mo:C ratio. They showed that that as the C concentration is increased, due to increased charge transfer from Mo to C atoms, Mo becomes increasingly positively charged, and as a result the $d$-band center moves downwards. We also observe a similar trend. In Fig. 5.8(a) we have plotted our results for the position of the $d$-band center as a function of the charge $q$(Mo) on Mo. As $x$, the percentage of N in the system increases, we see that Mo atoms become increasingly positively charged and the $d$-band center is shifted downwards.

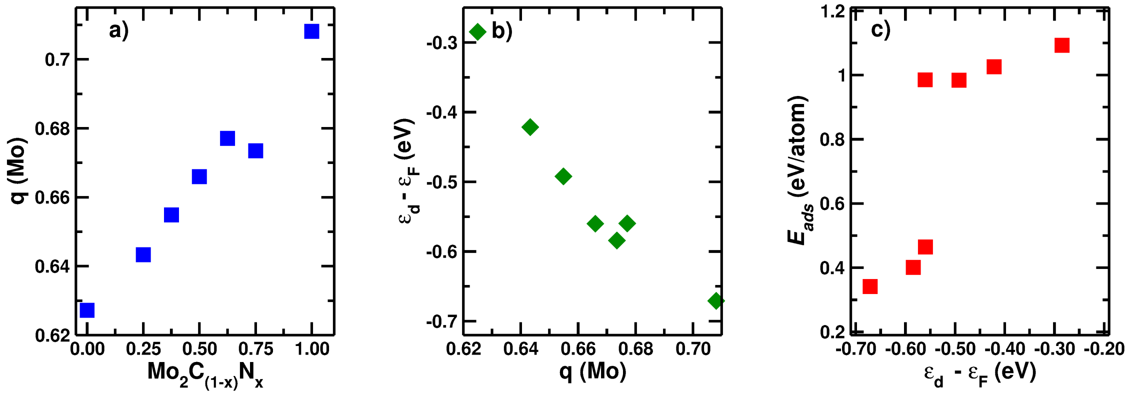

Figure 5.8: (a) Change in charge on Mo as a function of N doping concentration (b) Correlation between position of d-band center and charge on Mo (c) Correlation between adsorption energy of single H and position of d-band center for $Mo_2C_{1-x}N_x$. For $x = 0$, 0.25, 0.375 and 0.5 we have taken orthorhombic structure and for $x = 0.625$, 0.75 and 1 we have taken tetragonal structure.

Finally, in Fig. 5.8(c), we show how $\varepsilon_d$ is correlated with the adsorption energy of H atoms on the different surfaces. In accordance with the $d$-band model, we see that the higher in energy $\varepsilon_d$ is, the higher is the adsorption energy. A similar phenomenon has been observed for hydrogen adsorption on other transition-metal based substrates.[53;54]

### 5.5.5 Combining theory and experiment: Optimum value of $x$ leads to high HER activity

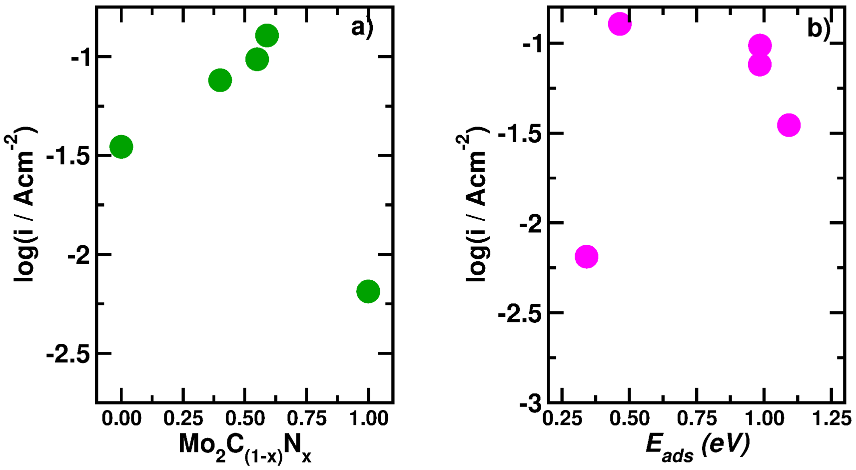

Figure 5.9: (a) experimental result for $\log_{10}$ of current density at 0.4 V overpotential as a function of different N concentrations in $Mo_2C_{1-x}N_x$ (b) experimental result for $\log_{10}$ of current density at 0.4 V overpotential vs. theoretical result for H adsorption energy for different N concentrations in $Mo_2C_{1-x}N_x$

The experimentally measured exchange current for the different systems was estimated to be at its maximum when the applied overpotential was at a value of 0.4 V. Upon comparing the measured exchange currents at an overpotential of 0.4 V, for pristine $Mo_2C$, pristine $Mo_2N$ and the doped systems, we find that the doped systems exhibited significantly higher exchange current than the pristine systems. Based on FESEM elemental mapping of the chemical composition, the three doped systems CN100, CN50 and CN25 were suggested to have $Mo_2C$:$Mo_2N$ ratios of 1:0.67, 1:1.22 and 1:1.42, respectively. If one approximates these doped structures to have chemical formula $Mo_2C_{1-x}N_x$, the experimental values of $x$ would be 0.40, 0.55 and 0.59, respectively, for the three doped systems of CN100, CN50 and CN25. To restrict our calculations to systems that have reasonably small primitive cells and are therefore computationally manageable, we compare these experimental systems with trends extracted by considering theoretical $x$ values of 0.375, 0.50 and 0.625, respectively.

In Fig. 5.9(a), we show experimental results for $\log_{10}$ of the current density at 0.4

V overpotential as a function of the theoretical N concentration $x$ in the doped system, while in Fig. 5.9(b), we show the same plotted as a function of the theoretically calculated adsorption energy for the respective pristine or doped system. The highest current density is measured for the doped system that is most rich in N, CN25.

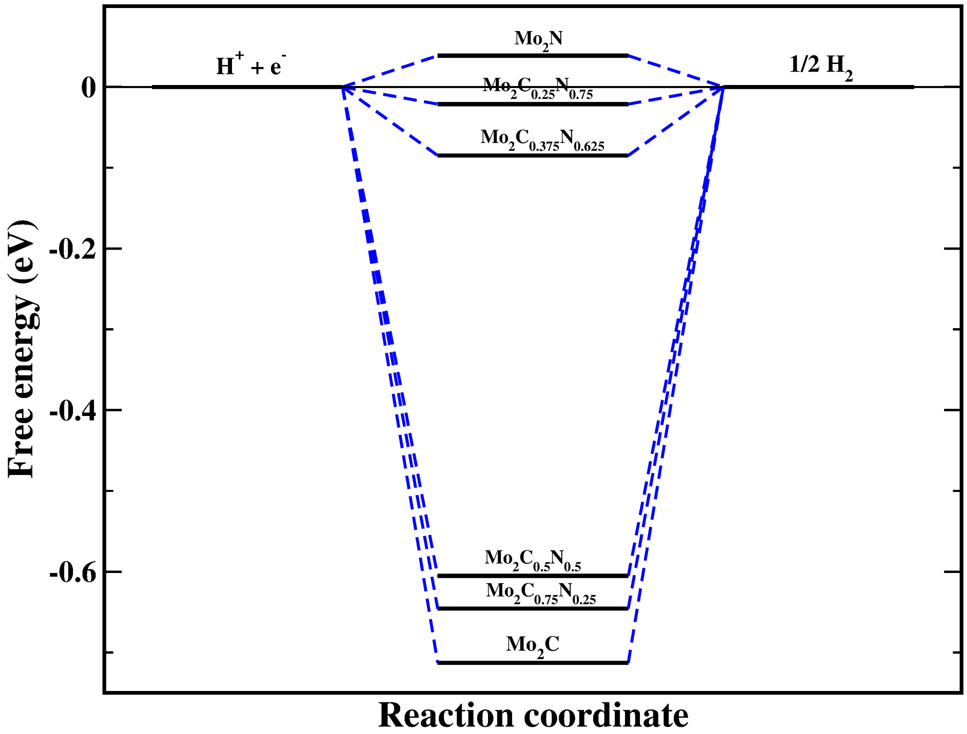

Figure 5.10: Calculated values of Gibbs free energy $\Delta G$ for hydrogen adsorption.

We now proceed to calculate $\Delta G$, the free energy of adsorption, using Eq. (5.5).[32] This has been shown to be a good indicator of systems with high HER activity. A good hydrogen evolution catalyst should have free energy ($\Delta G$) for adsorbing atomic hydrogen close to zero. This would suggest a fast proton-electron transfer step as well as fast hydrogen release process. If the value of $\Delta G$ is positive, the reaction is considered endothermic, implying that the interaction of the system with hydrogen is energetically unfavorable. HER can barely proceed because of slow proton/electron transfer. In Fig. 5.10, we show the Gibbs free energy diagram for $Mo_2C$, $Mo_2N$ and the doped structures. Pristine $Mo_2N$ has a $\Delta G$ value which is slightly positive, while all the other systems have negative values of $\Delta G$. The experimental sample CN25, which is approximated to have $x = 0.625$ has

$\Delta G = -0.021$ eV, which is negative and closest to zero among the samples studied experimentally. Our value for $\Delta G$ for $x = 0.75$ suggests that one could obtain a higher exchange current and hence higher HER activity for the doped systems if the N concentration is further increased to 75%.

## 5.6 Conclusions

In summary, we have used density functional theory incorporating van der Waals interactions to study the HER activity on molybdenum carbide, nitride and carbide-nitride mixed systems.

We first show that incorporating van der Waals interactions is essential to correctly reproduce the ground state structure of the carbide and nitride in the orthorhombic and tetragonal structures, respectively.

To estimate the HER activity of different systems, we have computed the Gibbs free energy which is a good descriptor for HER. We have shown that carbide-nitride mixed structures should show better HER activity than pure carbide and nitride structures. We have also shown that N-rich composite structures show better HER activity than C-rich composite structures. Our results match well with experimental observations.

# Bibliography

[1] J. Wallace and C. Ward, "Hydrogen as a fuel," *International Journal of Hydrogen Energy*, vol. 8, no. 4, pp. 255–268, 1983.

[2] B. Rohland, J. Nitsch, and H. Wendt, "Hydrogen and fuel cells the clean energy system," *Journal of power sources*, vol. 37, no. 1-2, pp. 271–277, 1992.

[3] M. Miles, E. Klaus, B. Gunn, J. Locker, W. Serafin, and S. Srinivasan, "The oxygen evolution reaction on platinum, iridium, ruthenium and their alloys at 80 c in acid solutions," *Electrochimica Acta*, vol. 23, no. 6, pp. 521–526, 1978.

[4] S. Trasatti, “Electronegativity, work function, and heat of adsorption of hydrogen on metals,” *Journal of the Chemical Society, Faraday Transactions 1: Physical Chemistry in Condensed Phases*, vol. 68, pp. 229–236, 1972.

[5] J. Nørskov and T. Bligaard, “a logadottir, jr kitchin, jg chen, s. pandelov, and u. stimming,” *J. Electrochem. Soc*, vol. 152, p. J23, 2005.

[6] H. Vrubel and X. Hu, “Molybdenum boride and carbide catalyze hydrogen evolution in both acidic and basic solutions,” *Angewandte Chemie International Edition*, vol. 51, no. 51, pp. 12703–12706, 2012.

[7] M. D. Scanlon, X. Bian, H. Vrubel, V. Amstutz, K. Schenk, X. Hu, B. Liu, and H. H. Girault, “Low-cost industrially available molybdenum boride and carbide as platinum–like catalysts for the hydrogen evolution reaction in biphasic liquid systems,” *Physical Chemistry Chemical Physics*, vol. 15, no. 8, pp. 2847–2857, 2013.

[8] R. Michalsky, Y.-J. Zhang, and A. A. Peterson, “Trends in the hydrogen evolution activity of metal carbide catalysts,” *ACS Catalysis*, vol. 4, no. 5, pp. 1274–1278, 2014.

[9] W.-F. Chen, J. T. Muckerman, and E. Fujita, “Recent developments in transition metal carbides and nitrides as hydrogen evolution electrocatalysts,” *Chemical communications*, vol. 49, no. 79, pp. 8896–8909, 2013.

[10] P. Xiao, Y. Yan, X. Ge, Z. Liu, J.-Y. Wang, and X. Wang, “Investigation of molybdenum carbide nano-rod as an efficient and durable electrocatalyst for hydrogen evolution in acidic and alkaline media,” *Applied Catalysis B: Environmental*, vol. 154, pp. 232–237, 2014.

[11] C. Wan, Y. N. Regmi, and B. M. Leonard, “Multiple phases of molybdenum carbide as electrocatalysts for the hydrogen evolution reaction,” *Angewandte Chemie International Edition*, vol. 53, no. 25, pp. 6407–6410, 2014.

[12] L. Liao, X. Bian, J. Xiao, B. Liu, M. D. Scanlon, and H. H. Girault, “Nanoporous molybdenum carbide wires as an active electrocatalyst towards the oxygen reduction reaction,” *Physical Chemistry Chemical Physics*, vol. 16, no. 21, pp. 10088–10094, 2014.

[13] B. Cao, G. M. Veith, J. C. Neuefeind, R. R. Adzic, and P. G. Khalifah, “Mixed close-packed cobalt molybdenum nitrides as non-noble metal electrocatalysts for the hydrogen evolution reaction,” *Journal of the American Chemical Society*, vol. 135, no. 51, pp. 19186–19192, 2013.

[14] W. Chen, K. Sasaki, C. Ma, A. Frenkel, and N. Marinkovic, “JT 125 muckerman, y. zhu, and rr adzic,” *Angew. Chem. Int. Ed*, vol. 51, pp. 6131–6135, 2012.

[15] J. Xie, S. Li, X. Zhang, J. Zhang, R. Wang, H. Zhang, B. Pan, and Y. Xie, “Atomically-thin molybdenum nitride nanosheets with exposed active surface sites for efficient hydrogen evolution,” *Chemical science*, vol. 5, no. 12, pp. 4615–4620, 2014.

[16] C. G. Morales-Guio, L.-A. Stern, and X. Hu, “Nanostructured hydrotreating catalysts for electrochemical hydrogen evolution,” *Chemical Society Reviews*, vol. 43, no. 18, pp. 6555–6569, 2014.

[17] H. Zhang, L. Lei, and X. Zhang, “One-step synthesis of cubic pyrite–type $CoSe_2$ at low temperature for efficient hydrogen evolution reaction,” *RSC Advances*, vol. 4, no. 97, pp. 54344–54348, 2014.

[18] H. Zhang, Y. Li, T. Xu, J. Wang, Z. Huo, P. Wan, and X. Sun, “Amorphous co-doped mos 2 nanosheet coated metallic $CoS_2$ nanocubes as an excellent electrocatalyst for hydrogen evolution,” *Journal of Materials Chemistry A*, vol. 3, no. 29, pp. 15020–15023, 2015.

[19] T. N. Kumar, N. Chandrasekaran, and K. L. Phani, “Structural and electronic modification of $MoS_2$ nanosheets using s-doped carbon for efficient electrocatalysis of the

hydrogen evolution reaction," *Chemical Communications*, vol. 51, no. 24, pp. 5052–5055, 2015.

[20] C. Xu, S. Peng, C. Tan, H. Ang, H. Tan, H. Zhang, and Q. Yan, "Ultrathin s-doped $MoSe_2$ nanosheets for efficient hydrogen evolution," *Journal of Materials Chemistry A*, vol. 2, no. 16, pp. 5597–5601, 2014.

[21] M. A. Lukowski, A. S. Daniel, C. R. English, F. Meng, A. Forticaux, R. J. Hamers, and S. Jin, "Highly active hydrogen evolution catalysis from metallic $WS_2$ nanosheets," *Energy & Environmental Science*, vol. 7, no. 8, pp. 2608–2613, 2014.

[22] Z. Xing, Q. Liu, A. M. Asiri, and X. Sun, "High-efficiency electrochemical hydrogen evolution catalyzed by tungsten phosphide submicroparticles," *ACS Catalysis*, vol. 5, no. 1, pp. 145–149, 2014.

[23] P. Jiang, Q. Liu, Y. Liang, J. Tian, A. M. Asiri, and X. Sun, "A cost-effective 3d hydrogen evolution cathode with high catalytic activity: Fep nanowire array as the active phase," *Angewandte Chemie International Edition*, vol. 53, no. 47, pp. 12855–12859, 2014.

[24] E. J. Popczun, J. R. McKone, C. G. Read, A. J. Biacchi, A. M. Wiltrout, N. S. Lewis, and R. E. Schaak, "Nanostructured nickel phosphide as an electrocatalyst for the hydrogen evolution reaction," *Journal of the American Chemical Society*, vol. 135, no. 25, pp. 9267–9270, 2013.

[25] J. F. Callejas, C. G. Read, E. J. Popczun, J. M. McEnaney, and R. E. Schaak, "Nanostructured $Co_2P$ electrocatalyst for the hydrogen evolution reaction and direct comparison with morphologically equivalent cop," *Chemistry of Materials*, vol. 27, no. 10, pp. 3769–3774, 2015.

[26] J. Kibsgaard, C. Tsai, K. Chan, J. D. Benck, J. K. Nørskov, F. Abild-Pedersen, and T. F.

Jaramillo, “Designing an improved transition metal phosphide catalyst for hydrogen evolution using experimental and theoretical trends,” *Energy & Environmental Science*, vol. 8, no. 10, pp. 3022–3029, 2015.

[27] M. Cabán-Acevedo, M. L. Stone, J. Schmidt, J. G. Thomas, Q. Ding, H.-C. Chang, M.-L. Tsai, J.-H. He, and S. Jin, “Efficient hydrogen evolution catalysis using ternary pyrite-type cobalt phosphosulphide,” *Nature materials*, vol. 14, no. 12, p. 1245, 2015.

[28] H. Ang, H. T. Tan, Z. M. Luo, Y. Zhang, Y. Y. Guo, G. Guo, H. Zhang, and Q. Yan, “Hydrophilic nitrogen and sulfur Co-doped molybdenum carbide nanosheets for electrochemical hydrogen evolution,” *Small*, vol. 11, no. 47, pp. 6278–6284, 2015.

[29] W.-F. Chen, S. Iyer, S. Iyer, K. Sasaki, C.-H. Wang, Y. Zhu, J. T. Muckerman, and E. Fujita, “Biomass-derived electrocatalytic composites for hydrogen evolution,” *Energy & Environmental Science*, vol. 6, no. 6, pp. 1818–1826, 2013.

[30] J. Bockris and E. Potter, “The mechanism of the cathodic hydrogen evolution reaction,” *Journal of The Electrochemical Society*, vol. 99, no. 4, pp. 169–186, 1952.

[31] V. S. Bagotsky, *Fundamentals of electrochemistry*, vol. 44. John Wiley & Sons, 2005.

[32] J. Nørskov and T. Bligaard, “a logadottir, jr kitchin, jg chen, s. pandelov, and u. stimming,” *J. Electrochem. Soc*, vol. 152, p. J23, 2005.

[33] P. Sabatier, “Hydrogénations et déshydrogénations par catalyse,” *Berichte der deutschen chemischen Gesellschaft*, vol. 44, no. 3, pp. 1984–2001, 1911.

[34] D. V. Esposito, S. T. Hunt, Y. C. Kimmel, and J. G. Chen, “A new class of electrocatalysts for hydrogen production from water electrolysis: metal monolayers supported on low-cost transition metal carbides,” *Journal of the American Chemical Society*, vol. 134, no. 6, pp. 3025–3033, 2012.

[35] K. Ojha *et al.*, *Nanostructured composites of molybdenum-based compounds*

*($Mo_2C$/$Mo_2N$/$MoS_2$/MoP) and graphene as electrocatalysts for hydrogen evolution reactions.* PhD thesis, 2016.

[36] W. Rieger and E. Parthé, "Alkaline earth silicides, germanides and stannides with CrB structure type," *Acta Crystallographica*, vol. 22, no. 6, pp. 919–922, 1967.

[37] H. Jehn and P. Ettmayer, "The molybdenum-nitrogen phase diagram," *Journal of the Less Common Metals*, vol. 58, no. 1, pp. 85–98, 1978.

[38] W. Kohn, "Density functional and density matrix method scaling linearly with the number of atoms," *Physical Review Letters*, vol. 76, no. 17, p. 3168, 1996.

[39] P. Hohenberg and W. Kohn, "Phys. rev.," *B*, vol. 136, pp. 864–871, 1964.

[40] B. Hammer, L. B. Hansen, and J. K. Nørskov, "Improved adsorption energetics within density-functional theory using revised perdew-burke-ernzerhof functionals," *Physical Review B*, vol. 59, no. 11, p. 7413, 1999.

[41] D. Vanderbilt, "Soft self-consistent pseudopotentials in a generalized eigenvalue formalism," *Physical review B*, vol. 41, no. 11, p. 7892, 1990.

[42] H. J. Monkhorst and J. D. Pack, "Special points for brillouin-zone integrations," *Physical review B*, vol. 13, no. 12, p. 5188, 1976.

[43] J. Antony and S. Grimme, "Density functional theory including dispersion corrections for intermolecular interactions in a large benchmark set of biologically relevant molecules," *Physical Chemistry Chemical Physics*, vol. 8, no. 45, pp. 5287–5293, 2006.

[44] N. Marzari, D. Vanderbilt, A. De Vita, and M. Payne, "Thermal contraction and disordering of the al (110) surface," *Physical review letters*, vol. 82, no. 16, p. 3296, 1999.

[45] L. Bengtsson, "Dipole correction for surface supercell calculations," *Physical Review B*, vol. 59, no. 19, p. 12301, 1999.

[46] B. Hammer and J. K. Nørskov, "Theoretical surface science and catalysis–calculations and concepts," in *Advances in catalysis*, vol. 45, pp. 71–129, Elsevier, 2000.

[47] V. Stamenkovic, B. S. Mun, K. J. Mayrhofer, P. N. Ross, N. M. Markovic, J. Rossmeisl, J. Greeley, and J. K. Nørskov, "Changing the activity of electrocatalysts for oxygen reduction by tuning the surface electronic structure," *Angewandte Chemie International Edition*, vol. 45, no. 18, pp. 2897–2901, 2006.

[48] R. F. Bader, "Atoms in molecules," *Accounts of Chemical Research*, vol. 18, no. 1, pp. 9–15, 1985.

[49] W. Tang, E. Sanville, and G. Henkelman, "A grid-based bader analysis algorithm without lattice bias," *Journal of Physics: Condensed Matter*, vol. 21, no. 8, p. 084204, 2009.

[50] S. Gražulis, D. Chateigner, R. T. Downs, A. Yokochi, M. Quirós, L. Lutterotti, E. Manakova, J. Butkus, P. Moeck, and A. Le Bail, "Crystallography open database–an open-access collection of crystal structures," *Journal of applied crystallography*, vol. 42, no. 4, pp. 726–729, 2009.

[51] K. Inumaru, K. Baba, and S. Yamanaka, "Synthesis and characterization of superconducting $\beta$-$Mo_2N$ crystalline phase on a si substrate: An application of pulsed laser deposition to nitride chemistry," *Chemistry of materials*, vol. 17, no. 24, pp. 5935–5940, 2005.

[52] P. Liu, J. A. Rodriguez, and J. T. Muckerman, "Desulfurization of $SO_2$ and thiophene on surfaces and nanoparticles of molybdenum carbide: Unexpected ligand and steric effects," *The Journal of Physical Chemistry B*, vol. 108, no. 40, pp. 15662–15670, 2004.

[53] L. A. Kibler, A. M. El-Aziz, R. Hoyer, and D. M. Kolb, "Tuning reaction rates by lateral strain in a palladium monolayer," *Angewandte Chemie International Edition*, vol. 44, no. 14, pp. 2080–2084, 2005.

[54] A. Vojvodic, A. J. Medford, F. Studt, F. Abild-Pedersen, T. S. Khan, T. Bligaard, and J. Nørskov, "Exploring the limits: a low-pressure, low-temperature haber–bosch process," *Chemical Physics Letters*, vol. 598, pp. 108–112, 2014.

# Chapter 6

# Anomalous change in band gap in Sn-doped $CsPbBr_3$ nanocrystals

## 6.1 Introduction

Quantum dots (QD) have attracted a great deal of attention in recent times,[1–5] as they show outstanding optoelectronic properties, including tunable band-gap, high photoluminescence quantum efficiency, narrow emission wavelength and high charge-carrier mobility. The wavelength of emission can be controlled by varying the size[6;7] and chemical constituents[5] of the quantum dots. Possible applications of such quantum dots include solar cells,[8;9] lasers,[10;11] and light emitting diodes (LED).[12;13] Most quantum dots can be classified into three types: (i) Cd-based QD (e.g., CdSe, CdTe), (ii) Cd-free QD (e.g., InP, $CuInS_2$), and (iii) perovskite QD (e.g., $CsPbBr_3$, $CH_3NH_3PbBr_3$).

Traditional semiconductor quantum dots such as CdSe,[14] and InP[15] have surface defects and trap states. These decrease their performance in optoelectronic devices. Perovskite quantum dots show better performance as the defects usually do not correspond to mid-gap states: instead, defect states arise either in the valence band or in the conduction band.[16;17] Moreover, these defects states are delocalized in nature, unlike the case of localized trap states of traditional semiconductor nanocrystals. Perovskite materials have strong absorption coefficients and small exciton binding energies. Because of this, they can be used as photovoltaic materials with power conversion efficiencies of up to 20%.[18;19] Perovskite QD are suitable for applications in light emitting diodes, because of high color purity emission spectra and low-cost solution processes.[20;21]

The perovskite structure has chemical composition of $ABX_3$ where A and B are usually metal cations and X is an anion, e.g., oxide or halide. In this thesis, we restrict ourselves to halide perovskites, where X is a halide anion. We note that depending on the nature of A, the material can be an inorganic perovskite (e.g., $CsPbBr_3$) or an inorganic-organic hybrid perovskite (e.g., $CH_3NH_3PbBr_3$). The $ABX_3$ motifs form a three-dimensional network where the B atoms are surrounded surrounded by six X anions, forming a $BX_6$ octahedral network. Each A unit is located at the center of eight such octahedra. The probability of forming the perovskite structure is determined by the Goldschmidt's tolerance factor ($t$) and the octahedral factor($\mu$).[22–24] These quantities are given by $t = (r_A + r_X)/\sqrt{2}(r_B + r_X)$ and $\mu = r_B/r_X$, where $r_A$, $r_B$ and $r_X$ are the ionic radii of A, B and X respectively (this formula can be generalized to the case where A is an organic moiety).[5]

It has been found empirically that for cubic perovskites, the structure is stable if $0.80 < t < 0.90$ and $0.40 < \mu < 0.90$.[23–26] So this implies that if the B atom is large (e.g. Pb), then X can only be a halide such as Br or Cl, while A can only be an inorganic cation such as Cs or small organic molecules with less than two or three C-C or C-N bonds.[5]

All inorganic lead halide perovskites (e.g., $CsPbX_3$) have great potential for application in LEDs.[20;21] There are multiple methods available for the synthesis of perovskite quantum dots and stabilizing them at room temperature. The most popular methods are the hot-injection method,[27;28] room-temperature method,[29–31] microfluidic reaction system method[32] and micelle method.[33] The band gap of perovskite quantum dots can be tuned by varying the particle size,[34] and by substitution of the cation[35] and/or anion[36] by changing the composition during the synthesis. Band gap tuning by partial halide substitution for both inorganic and organic perovskites has proved to be successful. The band gap of $CsPbX_3$ can be tuned over the whole visible range.[37;38] From X-ray diffraction (XRD) and microscopy studies it has been observed that the initial crystal structure is retained after anion exchange.[39;40]Exchange reaction is possible between all halides except $Cl^-$ and $I^-$. This exception is due to the large difference in ionic radii between Cl and I (1.81 Å and 2.20 Å respectively), resulting in a large lattice mismatch in the parent perovskite phases.

In real life applications, the toxicity of $Pb^{2+}$ in inorganic lead halide perovskites ($CsPbX_3$) makes them undesirable. So $Pb^{2+}$ is often sought to be replaced by other suitable cations. The most common substituted cations include Sn, Bi, Mn, Cd and Zn. For halide substitution the tunability in band gap is in the whole visible range of the electromagnetic spectrum.[37;38] For cation exchange the tunability in band gap is within a much smaller wavelength range. Lead-free $CsSnX_3$ has been synthesized using the hot-injection method[27]. However, the material was highly unstable and required storage in an inert atmosphere.

## 6.2 Experimental background

In recent experiments,[28] it has been shown that partially lead free perovskite quantum dots can be synthesized and stabilized at ambient conditions. In the experiments, Pb was partially replaced by divalent cations such as $Sn^{2+}$, $Cd^{2+}$ and $Zn^{2+}$. The structures were reported to be stable at room temperature. All the cation exchanges resulted in a blue shift in photoluminescence. This is opposite to what has previously been observed for cation doping in bulk $CsPb_{1-x}X_3$.[41–43] Our experimental collaborators in the group of Prof. Ranjani Viswanatha have recently synthesized $CsPb_{1-x}Sn_xBr_yI_{3-y}$ nanocrystals. A stoichiometric mixture of $PbI_2$ and $SnBr_2$ was used to synthesize $CsPb_{1-x}Sn_xBr_yI_{3-y}$ nanocrystals. XRD and Transmission Electron Microscopy (TEM) images confirm the structure as cubic. The nanocrystals are stable in ambient conditions. It has been observed that as the Sn-doping concentration increases, there is a blue shift in photoluminescence.

Motivated by the above experimental observations, we have performed density functional theory (DFT) calculations on Sn-doped $CsPbBr_3$. We want to not only theoretically confirm the experimental results on the blue shift, but also understand the reason behind this unusual band gap change upon Sn-doping on perovskite nanocrystals, which is opposite to what has been observed for bulk materials.

## 6.3 Computational Details

Our calculations have been performed using *ab initio* density functional theory (DFT),[44;45] as implemented in the Quantum ESPRESSO package.[46] To describe the exchange–correlation interactions a generalized gradient approximation of the PBE form is used.[47] Electronic wavefunctions are expanded using a plane wave basis set, with cutoffs of 40 Ry and 400 Ry for the wavefunctions and charge density, respectively. The Brillouin zone is sampled with a Monkhorst-Pack[48] mesh of 8×8×8 k-points for the primitive cell of $CsPbBr_3$. The interactions between the ionic cores and valence electrons are described using ultrasoft pseudopotentials.[49] As spin-orbit effects are expected to be significant due to the presence of Pb atoms, they have been incorporated using fully relativistic pseudopotentials.[50] Structural optimizations are performed using the Broyden-Fletcher-Goldfarb-Shanno (BFGS) scheme, until the Hellmann-Feynman forces on all the atoms being relaxed are less than 0.001 Ry/bohr. It has been found that van der Waals interactions play an important role in correctly predicting the structure of perovskites.[51] It is well known that London dispersion interactions are not incorporated in ‘conventional’ DFT. In order to have an accurate yet computationally affordable treatment of London dispersion interactions we have made use of the “DFT-D2” treatment introduced by Grimme.[52]. DFT calculations have been used to parametrize a Wannier-based tight binding model.[53] Here, we have used the projection method[53] to construct atom-centered Wannier functions using which it is possible to calculate the positions of the atomic levels and gain insight into interatomic interactions.

## 6.4 Results

### 6.4.1 Lattice parameter and band-gap of cubic $CsPbBr_3$

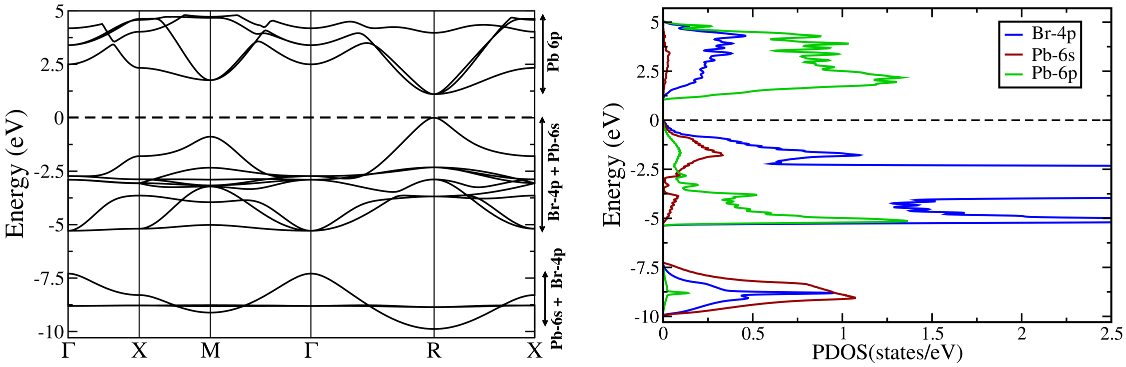

(a) (b)

Figure 6.1: Results from DFT for (a) electronic band structure along high-symmetry directions of the Brillouin zone, and (b) projected density of states (PDOS) of bulk $CsPbBr_3$ in the cubic structure. The figure on the right shows the PDOS, with the DOS projected onto Br-4p (blue), Pb-6s (maroon) and Pb-6p (green) orbitals. In both figures, the dashed line shows the position of the Fermi level.

Previous experimental results[28] as well as X-ray diffraction (XRD) and TEM results from our experimental collaborators show that Sn-doped $CsPbBr_3$ perovskite nanocrystals are highly crystalline and retain the cubic structure of the undoped parent counterparts. We have therefore performed our theoretical calculations on the cubic structure of $CsPbBr_3$ and study Sn doping of this structure. We find the lattice constant of $CsPbBr_3$ to be 5.64 Å. This value is in fairly good agreement with our experimental value of 5.85 Å for the $CsPbBr_3$ nanocrystal and an earlier experimental value of 5.874 Å [54] for bulk $CsPbBr_3$. The calculated band gap of $CsPbBr_3$ is 1.79 eV. This can be compared with a previous DFT value of 1.7 eV,[54] an earlier experimental value of 2.36 eV [55] for bulk $CsPbBr_3$

and our experimental result of 2.42 eV for the $CsPbBr_3$ nanocrystal. We note that the underestimation of the band gap is a well known shortcoming of standard DFT calculations. The band structure and projected density of states (PDOS) of $CsPbBr_3$ (without the incorporation of spin-orbit interactions) are shown in Fig. 6.1(a) and Fig. 6.1(b) respectively. We find that the valence band and the band below this arise mainly from antibonding and bonding, respectively, between Br 4p and Pb 6s orbitals. The conduction band has primarily Pb 6p character, though it also has some Br 4p character, as can be seen from the PDOS plotted in Fig. 6.1(b). The band gap is direct at the R point.

### 6.4.2 Band-gap change with lattice parameter of cubic $CsPbBr_3$

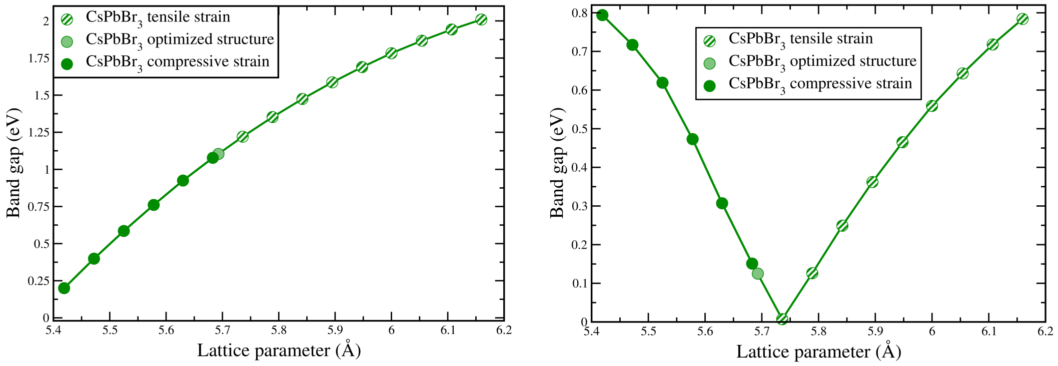

(a) (b)

Figure 6.2: Change in band gap with lattice parameter of cubic $CsPbBr_3$ (a) without SOC and (b) with SOC. Note that without SOC, the change is monotonic, whereas with SOC, it is non-monotonic due to the presence of a band inversion. Note the position of the point in (b) that indicates the equilibrium lattice constant for $CsPbBr_3$.

Next we want to investigate how the band gap changes with lattice parameter for cubic $CsPbBr_3$. In order to do this, we subject cubic $CsPbBr_3$ to both tensile and compressive strain, and see how the electronic structure changes, in the absence as well as presence of spin-orbit interactions. The band gap change with lattice constant without and with the inclusion of spin-orbit coupling is shown in Figs. 6.2(a) and 6.2(b), respectively. We see that without the inclusion of spin-orbit coupling, the band-gap decreases with decreasing lattice constant [see Fig. 6.2(a)]. However, when spin-orbit coupling (SOC) is included, with decreasing lattice parameter the band-gap of cubic $CsPbBr_3$ first decreases and then increases, as shown in Fig. 6.2(b). We will investigate the reason for this non-monotonic band gap change with lattice parameter (in the presence of SOC) in the next section.

### 6.4.3 Movement of valence and conduction band with lattice parameter

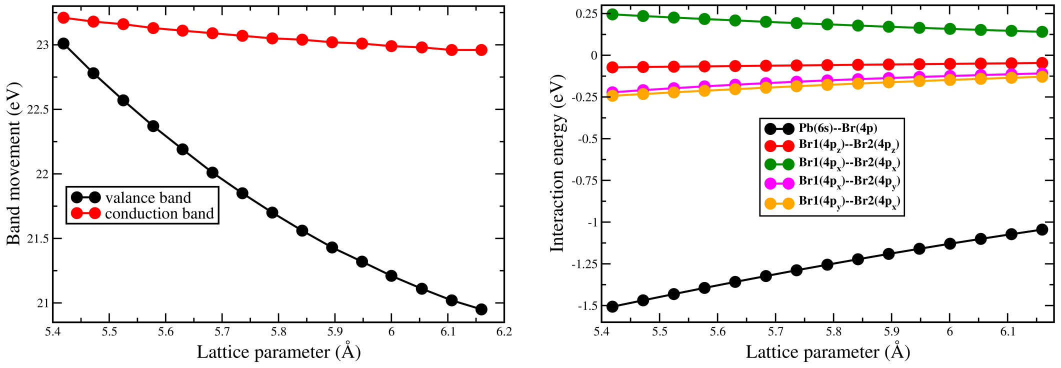

(a) (b)

Figure 6.3: (a) Movement of valence band and conduction band with lattice parameter (b) Change in different orbital contributions with lattice parameter.All positions are measured with respect to a deep-lying core level that does not shift with lattice parameter.

To understand how the band gap changes with lattice constant, we can view this as a two-step process. We first examine how the positions of the band edges change with strain, in the absence of SOC, and we then examine how these levels split upon incorporation of SOC.

We will first see how the valence band and conduction band edges move with changing lattice parameter for cubic $CsPbBr_3$, in the absence of SOC. In Fig. 6.3(a) we show the movement of valence band and conduction band edges with decreasing lattice parameter for cubic $CsPbBr_3$. Upon changing the lattice parameter, the movement of the valence band maximum is much greater than that of the the conduction band minimum. Note that in this figure, the movement of both edges is measured with respect to the position of the deep-lying Cs 5s core-level, which does not shift with lattice constant. For further analysis, we first recall from Fig. 6.1 that the valence band has antibonding character, arising from Br 4p and Pb 6s orbitals, and the conduction band arises from Pb 6p orbitals.

We have used DFT to obtain the parameters for a Wannier-based tight binding model to calculate the interaction strength between different orbitals.[56] We have considered the Br 4p, Pb 6s and Cs 5s states to carry out the Wannier projections. In Fig. 6.3(b) the change in the strength of different orbital interactions with lattice parameter is shown. We see that the most prominent change that occurs is in the interaction between Br 4p and Pb 6s orbitals. This explains the results of Fig. 6.3(a). As the valence band consists of anti-bonding character of Br 4p and Pb 6s, the movement of the valence band maximum with strain is significant. On the other hand, the conduction band consists of 'non bonding' Pb 6p orbitals. So there is almost no change in the conduction band minimum with lattice parameter.

This movement of the valence band and conduction band edges with lattice parameter explains Fig. 6.3(a). As the position of the conduction band remains almost unchanged, and the valence band moves up in energy upon decreasing the lattice parameter, there is a monotonic decrease in band gap.

### 6.4.4 Why the SOC band-gap changes non-monotonically with lattice parameter

We wish to understand why, upon the inclusion of spin orbit coupling, the band gap changes non-monotonically with lattice parameter. To do this, we will first look at what happens to the orbital levels (at equilibrium lattice constant) upon inclusion of spin-orbit coupling.

From Fig. 6.1(b) we can say that the valence band is primarily contributed to by Br 4p states and the conduction band is primarily contributed to by Pb 6p states when there is no spin-orbit coupling. In Fig. 6.4 we have plotted the projected band-structure of $CsPbBr_3$ at equilibrium lattice constant when spin-orbit coupling is included. In this picture, the color of the bands indicates the orbital nature of the state at that point. A yellow color indicates a fully Pb 6p nature and a blue color indicates a fully Br 4p nature, with intermediate colors indicating hybridization between the two. (Note that in this

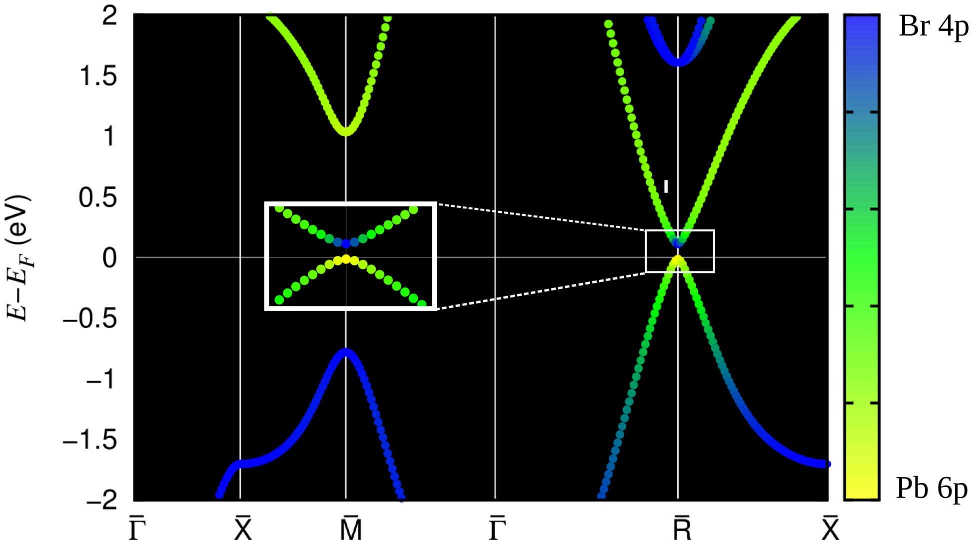

Figure 6.4: Projected band-structure of bulk $CsPbBr_3$ at optimized lattice constant. The color of each point indicates the orbital character of the band at that wave-vector. A blue color indicates fully Br 4p character, yellow color indicates fully Pb 6p character, and the intermediate colors denote appropriate amount of partial contributions from Br 4p and Pb 6p .

figure, for simplicity we have ignored the partially Pb 6s character of the valence band). We see that, in keeping with our discussion above, the valence band is primarily blue (Br 4p), while the conduction band is mostly of Pb 6p character. However, we can see that at the R point, there is a band inversion: the orbital character gets inverted, as can be seen by the blue color of the conduction band minimum at R, and the yellow color of the valence band maximum at R; this is made even more clear in the inset to the figure.

We will now attempt to show why the introduction of a band inversion upon including SOC also results in a reversal in trends in band gap changes. The two left halves of Figs. 6.5(a) and (b) show the situation in the absence of SOC, for two different lattice constants. The blue dashed lines show the position of the valence band maximum (VBM) and the green solid lines show the position of the conduction band minimum (CBM), at two different lattice constants. The positions of the band edges have been obtained from the DFT results for the band structure in the absence of SOC. By comparing the results at two lattice constants, we see that (in the absence of SOC) there is a decrease in band gap (red shift) on decreasing the lattice constant. The two right halves of Figs. 6.5(a) and

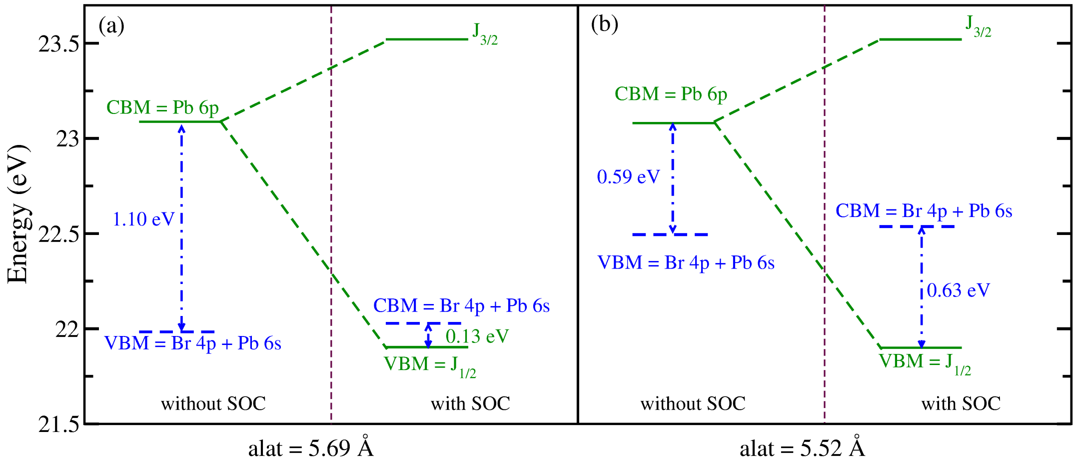

Figure 6.5: Movement of valence and conduction band edges with lattice parameter. Results at (a) $a = 5.69$ Å and (b) 5.52 Å. In each case, the left and right panels show the results without with SOC, respectively. The blue and green colors indicate bands that have primarily Pb 6p and Br 4p character, respectively.

(b) show what happens when SOC is included. The positions of the dashed blue levels remain essentially unchanged. However, the solid green level, which has Pb 6p nature, now splits. This splitting is indicated by the positions of the $J_{3/2}$ and $J_{1/2}$ lines in the two right panels. The amount of splitting is essentially independent of lattice constant. This splitting is large enough that the lower green level ($J_{1/2}$) now falls below the blue level, i.e., there is a band inversion, so that now the the VBM is 'green' and the CBM is 'blue'. Now let us compare the results at the two lattice constants. Since in the absence of SOC, the green level was closer to the blue level at the smaller lattice constant, it also follows that the green level is much below the blue level upon including SOC for the smaller lattice constant than for the larger lattice constant. In other words, upon including SOC, when we decrease the lattice constant, the band gap increases, i.e., there is a blue shift. Thus, for the range of lattice constants where there is a band inversion induced by SOC, the red shift becomes flipped to a blue shift.

### 6.4.5 Sn-doping of $CsPbBr_3$

Next we consider Sn-doping of $CsPbBr_3$ in the cubic structure. We note that experimentally it has been observed that the doping concentration of Sn cannot be more than 10% – 20% for perovskite nanocrystals.[28] However, so as to obtain clear trends at relatively low computational cost, for our theoretical calculations we have considered Sn doping for dopant concentrations up to 50%. We consider a 2×2×2 unit cell of cubic $CsPbBr_3$. Using this unit cell, we can consider Sn dopant concentrations of 0%, 12.5%, 25%, 37.5% and 50%. Note that the lattice constant is optimized for each dopant concentration; this is a crucial point.

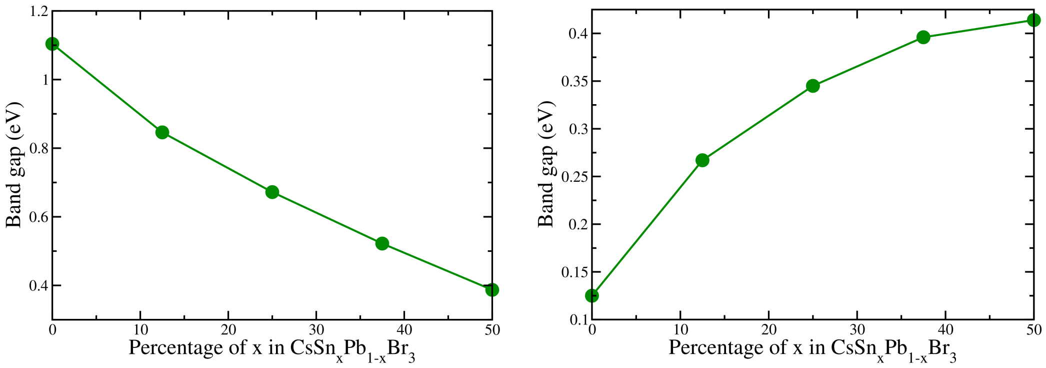

(a) (b)

Figure 6.6: Change in band gap of Cubic $CsPbBr_3$ with Sn doping (a) without SOC and (b) with SOC

In Fig. 6.6(a) we have shown the band gap change with increasing Sn doping concentration without spin-orbit interaction and in Fig. 6.6(b) we have shown the band gap change with increasing Sn doping concentration with spin-orbit interaction. We see a completely opposite trend in the band gap change without and with spin-orbit interaction. With increasing Sn doping concentration, the band gap decreases when spin-orbit interaction is not included, whereas the band gap increases with Sn doping concentration when the spin-orbit interaction is included. Note that the latter trend matches with the experimental observation.

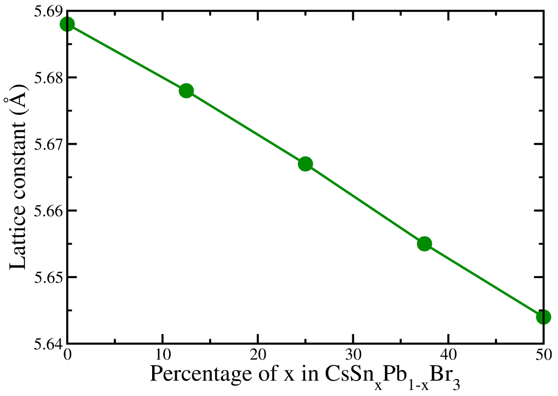

Figure 6.7: Change in lattice constant with Sn doping

To investigate why the band-gap changes differently without and with spin-orbit interaction, we first consider the change in lattice parameter with increasing Sn doping concentration. From Fig. 6.7 we see that the lattice parameter decreases as we increase the concentration of Sn. This is because the atomic radius of Sn is smaller than that of Pb.

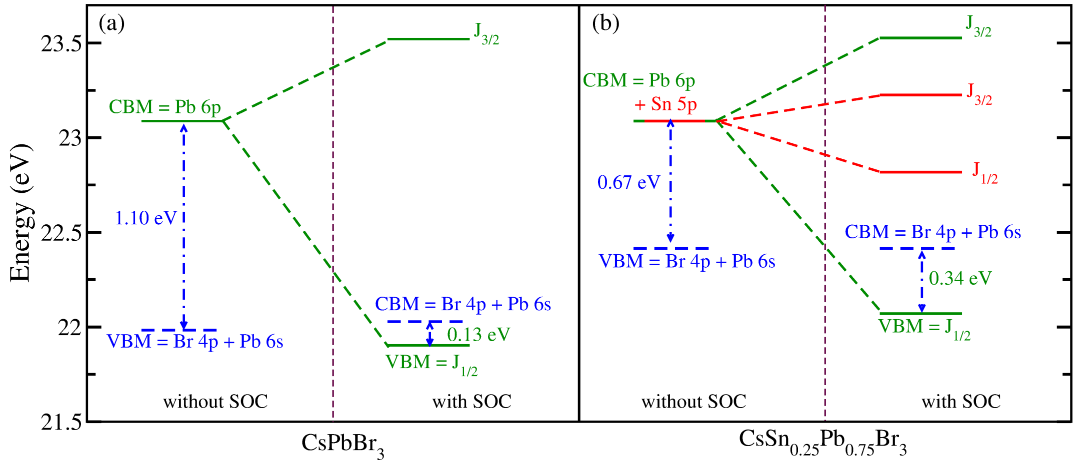

Figure 6.8: Position of atomic levels for (a) CsPbBr$_3$ and (b)CsSn$_0$.25Pb$_0$.75Br$_3$. Green, blue and red colors indicate predominantly Pb 6p, Br 4p and Sn 5p character, respectively. In each case, the left and right panels show results without and with SOC, respectively.

Fig. 6.8 is similar to Fig. 6.5, except that panel (a) shows the situation for undoped CsPbBr$_3$ and panel (b) shows the result for the case of 25% Sn-doping; note that the Sn-doping also results in a decrease in lattice constant. We see that the situation is similar to what we had discussed above. The important thing to note is that the spin-orbit splitting for Sn is much smaller than for Pb, as expected. Thus again, we have to consider only the role played by the splitting of the Pb 6p states, which constitute the CBM in the absence of SOC, and get band-inverted to constitute the VBM upon inclusion of SOC. The arguments are the same as above, resulting in a blue shift upon Sn-doping. The crucial point to note here is that the main effect of Sn-doping is to result in a decrease in lattice constant, which results in a decrease in the non-SOC band gap, which gets band-inverted to an increase in the SOC band gap.

## 6.5 Conclusions

In summary, we have used density functional theory incorporating spin-orbit interactions to study the effect of Sn doping on cubic $CsPbBr_3$. We have studied the cubic structure since this is experimentally determined to be the ground state structure in nanocrystals.

We first show from an analysis of the band-structure and PDOS of cubic $CsPbBr_3$, that the VBM mainly comes from Br 4p and Pb 6s states, whereas the CBM mainly comes from Pb 6p states. Next, we have shown that with decreasing lattice parameter, the band-gap changes (decreases) monotonically without spin-orbit interaction and non-monotonically (decreases first and then increases) with inclusion of spin-orbit interaction. We have shown that this non-monotonicity results from the fact that there is a range of lattice constants for which there is a band inversion upon including spin-orbit interactions, which in turn results in the red shift (on decreasing lattice constant) being flipped to a blue shift for this range of lattice constants. Finally we have used similar arguments to explain the reason behind the increase in band-gap upon Sn doping. We have shown that the effect of Sn doping is primarily in changing the lattice parameter of the perovskite structure, which leads to the band-gap change.

# Bibliography

[1] Y. Shang and Z. Ning, “Colloidal quantum-dots surface and device structure engineering for high-performance light-emitting diodes,” *National Science Review*, vol. 4, no. 2, pp. 170–183, 2017.

[2] L. Brus, “Electronic wave functions in semiconductor clusters: experiment and theory,” *The Journal of Physical Chemistry*, vol. 90, no. 12, pp. 2555–2560, 1986.

[3] A. P. Alivisatos, “Semiconductor clusters, nanocrystals, and quantum dots,” *Science*, vol. 271, no. 5251, pp. 933–937, 1996.

[4] Y. Shirasaki, G. J. Supran, M. G. Bawendi, and V. Bulović, “Emergence of colloidal quantum-dot light-emitting technologies,” *Nature Photonics*, vol. 7, no. 1, p. 13, 2013.

[5] L. Protesescu, S. Yakunin, M. I. Bodnarchuk, F. Krieg, R. Caputo, C. H. Hendon, R. X. Yang, A. Walsh, and M. V. Kovalenko, “Nanocrystals of cesium lead halide perovskites ($CsPbX_3$, (X= Cl, Br, and I): novel optoelectronic materials showing bright emission with wide color gamut,” *Nano Letters*, vol. 15, no. 6, pp. 3692–3696, 2015.

[6] S. Aharon and L. Etgar, “Two dimensional organometal halide perovskite nanorods with tunable optical properties,” *Nano Letters*, vol. 16, no. 5, pp. 3230–3235, 2016.

[7] C. Murray, D. J. Norris, and M. G. Bawendi, “Synthesis and characterization of nearly monodisperse CdE (E= sulfur, selenium, tellurium) semiconductor nanocrystallites,” *Journal of the American Chemical Society*, vol. 115, no. 19, pp. 8706–8715, 1993.

[8] G. H. Carey, A. L. Abdelhady, Z. Ning, S. M. Thon, O. M. Bakr, and E. H. Sargent, “Colloidal quantum dot solar cells,” *Chemical Reviews*, vol. 115, no. 23, pp. 12732–12763, 2015.

[9] Z. Ning, H. Dong, Q. Zhang, O. Voznyy, and E. H. Sargent, “Solar cells based on inks of n-type colloidal quantum dots,” *ACS Nano*, vol. 8, no. 10, pp. 10321–10327, 2014.

[10] S. Hoogland, V. Sukhovatkin, I. Howard, S. Cauchi, L. Levina, and E. Sargent, "A solution-processed 1.53 $\mu$m quantum dot laser with temperature-invariant emission wavelength," *Optics Express*, vol. 14, no. 8, pp. 3273–3281, 2006.

[11] Y. Wang, X. Li, X. Zhao, L. Xiao, H. Zeng, and H. Sun, "Nonlinear absorption and low-threshold multiphoton pumped stimulated emission from all-inorganic perovskite nanocrystals," *Nano Letters*, vol. 16, no. 1, pp. 448–453, 2015.

[12] H. Cho, S.-H. Jeong, M.-H. Park, Y.-H. Kim, C. Wolf, C.-L. Lee, J. H. Heo, A. Sadhanala, N. Myoung, S. Yoo, *et al.*, "Overcoming the electroluminescence efficiency limitations of perovskite light-emitting diodes," *Science*, vol. 350, no. 6265, pp. 1222–1225, 2015.

[13] J. Caruge, J. Halpert, V. Wood, V. Bulović, and M. Bawendi, "Colloidal quantum-dot light-emitting diodes with metal-oxide charge transport layers," *Nature Photonics*, vol. 2, no. 4, p. 247, 2008.

[14] W. Nan, Y. Niu, H. Qin, F. Cui, Y. Yang, R. Lai, W. Lin, and X. Peng, "Crystal structure control of zinc-blende CdSe/CdS core/shell nanocrystals: synthesis and structure-dependent optical properties," *Journal of the American Chemical Society*, vol. 134, no. 48, pp. 19685–19693, 2012.

[15] H. C. Wang, H. Zhang, H. Y. Chen, H. C. Yeh, M. R. Tseng, R. J. Chung, S. Chen, and R. S. Liu, "Cadmium-free InP/ZnSeS/ZnS heterostructure-based quantum dot light-emitting diodes with a ZnMgO electron transport layer and a brightness of over 10 000 cd m$^-$2," *Small*, vol. 13, no. 13, p. 1603962, 2017.

[16] D. N. Dirin, L. Protesescu, D. Trummer, I. V. Kochetygov, S. Yakunin, F. Krumeich, N. P. Stadie, and M. V. Kovalenko, "Harnessing defect-tolerance at the nanoscale: highly luminescent lead halide perovskite nanocrystals in mesoporous silica matrixes," *Nano Letters*, vol. 16, no. 9, pp. 5866–5874, 2016.

[17] Q. A. Akkerman, D. Meggiolaro, Z. Dang, F. De Angelis, and L. Manna, "Fluorescent alloy $\mathrm{CsPb}_x\,\mathrm{Mn}_{1-x}\,\mathrm{I}_3$ perovskite nanocrystals with high structural and optical stability," *ACS Energy Letters*, vol. 2, no. 9, pp. 2183–2186, 2017.

[18] G. E. Eperon, T. Leijtens, K. A. Bush, R. Prasanna, T. Green, J. T.-W. Wang, D. P. McMeekin, G. Volonakis, R. L. Milot, R. May, *et al.*, "Perovskite-perovskite tandem photovoltaics with optimized band gaps," *Science*, vol. 354, no. 6314, pp. 861–865, 2016.

[19] N. N. Lal, Y. Dkhissi, W. Li, Q. Hou, Y.-B. Cheng, and U. Bach, "Perovskite tandem solar cells," *Advanced Energy Materials*, vol. 7, no. 18, p. 1602761, 2017.

[20] J. S. Steckel, J. Ho, C. Hamilton, J. Xi, C. Breen, W. Liu, P. Allen, and S. Coe-Sullivan, "Quantum dots: The ultimate down-conversion material for lcd displays," *Journal of the Society for Information Display*, vol. 23, no. 7, pp. 294–305, 2015.

[21] S. Coe-Sullivan, W. Liu, P. Allen, and J. S. Steckel, "Quantum dots for led downconversion in display applications," *ECS Journal of Solid State Science and Technology*, vol. 2, no. 2, pp. R3026–R3030, 2013.

[22] V. M. Goldschmidt, "Die gesetze der krystallochemie," *Naturwissenschaften*, vol. 14, no. 21, pp. 477–485, 1926.

[23] C. Li, X. Lu, W. Ding, L. Feng, Y. Gao, and Z. Guo, "Formability of $\mathrm{ABX}_3$ (X= F, Cl, Br, I) halide perovskites," *Acta Crystallographica Section B: Structural Science*, vol. 64, no. 6, pp. 702–707, 2008.

[24] M. A. Green, A. Ho-Baillie, and H. J. Snaith, "The emergence of perovskite solar cells," *Nature Photonics*, vol. 8, no. 7, p. 506, 2014.

[25] G. Kieslich, S. Sun, and A. K. Cheetham, "Solid-state principles applied to organic–inorganic perovskites: new tricks for an old dog," *Chemical Science*, vol. 5, no. 12, pp. 4712–4715, 2014.

[26] M. Era, S. Morimoto, T. Tsutsui, and S. Saito, "Organic-inorganic heterostructure electroluminescent device using a layered perovskite semiconductor (c6h5c2h4nh3) 2pbi4," *Applied physics letters*, vol. 65, no. 6, pp. 676–678, 1994.

[27] T. C. Jellicoe, J. M. Richter, H. F. Glass, M. Tabachnyk, R. Brady, S. E. Dutton, A. Rao, R. H. Friend, D. Credgington, N. C. Greenham, *et al.*, "Synthesis and optical properties of lead-free cesium tin halide perovskite nanocrystals," *Journal of the American Chemical Society*, vol. 138, no. 9, pp. 2941–2944, 2016.

[28] W. Van der Stam, J. J. Geuchies, T. Altantzis, K. H. Van Den Bos, J. D. Meeldijk, S. Van Aert, S. Bals, D. Vanmaekelbergh, and C. de Mello Donega, "Highly emissive divalent-ion-doped colloidal $CsPb_{1--x}M_xBr_3$ perovskite nanocrystals through cation exchange," *Journal of the American Chemical Society*, vol. 139, no. 11, pp. 4087–4097, 2017.

[29] F. Zhang, H. Zhong, C. Chen, X.-g. Wu, X. Hu, H. Huang, J. Han, B. Zou, and Y. Dong, "Brightly luminescent and color-tunable colloidal $CH_3NH_3PbX_3$ (X= Br, I, Cl) quantum dots: potential alternatives for display technology," *ACS nano*, vol. 9, no. 4, pp. 4533–4542, 2015.

[30] X. Li, Y. Wu, S. Zhang, B. Cai, Y. Gu, J. Song, and H. Zeng, "$CsPbX_3$ quantum dots for lighting and displays: room-temperature synthesis, photoluminescence superiorities, underlying origins and white light-emitting diodes," *Advanced Functional Materials*, vol. 26, no. 15, pp. 2435–2445, 2016.

[31] S. Sun, D. Yuan, Y. Xu, A. Wang, and Z. Deng, "Ligand-mediated synthesis of shape-controlled cesium lead halide perovskite nanocrystals via reprecipitation process at room temperature," *ACS Nano*, vol. 10, no. 3, pp. 3648–3657, 2016.

[32] I. Lignos, S. Stavrakis, G. Nedelcu, L. Protesescu, A. J. deMello, and M. V. Kovalenko,

"Synthesis of cesium lead halide perovskite nanocrystals in a droplet-based microfluidic platform: fast parametric space mapping," *Nano Letters*, vol. 16, no. 3, pp. 1869–1877, 2016.

[33] S. T. McBeath, D. P. Wilkinson, and N. Graham, "Application of boron-doped diamond electrodes for the anodic oxidation of pesticide micropollutants in a water treatment process: A critical review," *Environmental Science: Water Research & Technology*, 2019.

[34] X. Dai, Y. Deng, X. Peng, and Y. Jin, "Quantum-dot light-emitting diodes for large-area displays: towards the dawn of commercialization," *Advanced Materials*, vol. 29, no. 14, p. 1607022, 2017.

[35] Z. Yuan, Y. Shu, Y. Xin, and B. Ma, "Highly luminescent nanoscale quasi-2d layered lead bromide perovskites with tunable emissions," *Chemical Communications*, vol. 52, no. 20, pp. 3887–3890, 2016.

[36] N. Kitazawa, Y. Watanabe, and Y. Nakamura, "Optical properties of ch 3 nh 3 pbx 3 (x= halogen) and their mixed-halide crystals," *Journal of Materials Science*, vol. 37, no. 17, pp. 3585–3587, 2002.

[37] E. R. Dohner, E. T. Hoke, and H. I. Karunadasa, "Self-assembly of broadband white-light emitters," *Journal of the American Chemical Society*, vol. 136, no. 5, pp. 1718–1721, 2014.

[38] E. R. Dohner, A. Jaffe, L. R. Bradshaw, and H. I. Karunadasa, "Intrinsic white-light emission from layered hybrid perovskites," *Journal of the American Chemical Society*, vol. 136, no. 38, pp. 13154–13157, 2014.

[39] Q. A. Akkerman, V. DfiInnocenzo, S. Accornero, A. Scarpellini, A. Petrozza, M. Prato, and L. Manna, "Tuning the optical properties of cesium lead halide perovskite nanocrystals by anion exchange reactions," *Journal of the American Chemical Society*, vol. 137, no. 32, pp. 10276–10281, 2015.

[40] G. Nedelcu, L. Protesescu, S. Yakunin, M. I. Bodnarchuk, M. J. Grotevent, and M. V. Kovalenko, “Fast anion-exchange in highly luminescent nanocrystals of cesium lead halide perovskites ($CsPbX_3$, X= Cl, Br, I),” *Nano Letters*, vol. 15, no. 8, pp. 5635–5640, 2015.

[41] H.-J. Feng, T. R. Paudel, E. Y. Tsymbal, and X. C. Zeng, “Tunable optical properties and charge separation in $CH_3NH_3Sn_xPb_{1-x}I_3/TiO_2$-based planar perovskites cells,” *Journal of the American Chemical Society*, vol. 137, no. 25, pp. 8227–8236, 2015.

[42] D. Zhao, Y. Yu, C. Wang, W. Liao, N. Shrestha, C. R. Grice, A. J. Cimaroli, L. Guan, R. J. Ellingson, K. Zhu, *et al.*, “Low-bandgap mixed tin-lead iodide perovskite absorbers with long carrier lifetimes for all-perovskite tandem solar cells,” *Nature Energy*, vol. 2, no. 4, p. 17018, 2017.

[43] Y. Ogomi, A. Morita, S. Tsukamoto, T. Saitho, N. Fujikawa, Q. Shen, T. Toyoda, K. Yoshino, S. S. Pandey, T. Ma, *et al.*, “$CH_3NH_3Sn_xPb_{1-x}I_3$ perovskite solar cells covering up to 1060 nm,” *The Journal of Physical Chemistry Letters*, vol. 5, no. 6, pp. 1004–1011, 2014.

[44] W. Kohn and L. Sham, “Self-consistent equations including exchange and correlation effects,” *Physical Review A*, vol. 140, p. 113, 1965.

[45] P. Hohenberg and W. Kohn, “Inhomogeneous electron gas,” *Physical Review B*, vol. 136, p. 864, 1964.

[46] P. Giannozzi, S. Baroni, N. Bonini, M. Calandra, R. Car, C. Cavazzoni, D. Ceresoli, G. L. Chiarotti, M. Cococcioni, I. Dabo, *et al.*, “Quantum espresso: a modular and open-source software project for quantum simulations of materials,” *Journal of Physics: Condensed matter*, vol. 21, no. 39, p. 395502, 2009.

[47] J. P. Perdew, K. Burke, and M. Ernzerhof, “Generalized gradient approximation made simple,” *Physical Review Letters*, vol. 77, no. 18, p. 3865, 1996.

[48] H. J. Monkhorst and J. D. Pack, "Special points for brillouin-zone integrations," *Physical Review B*, vol. 13, no. 12, p. 5188, 1976.

[49] D. Vanderbilt, "Soft self-consistent pseudopotentials in a generalized eigenvalue formalism," *Physical Review B*, vol. 41, no. 11, p. 7892, 1990.

[50] A. Dal Corso and A. M. Conte, "Spin-orbit coupling with ultrasoft pseudopotentials: Application to Au and Pt," *Physical Review B*, vol. 71, no. 11, p. 115106, 2005.

[51] D. N. Dirin, L. Protesescu, D. Trummer, I. V. Kochetygov, S. Yakunin, F. Krumeich, N. P. Stadie, and M. V. Kovalenko, "Harnessing defect-tolerance at the nanoscale: highly luminescent lead halide perovskite nanocrystals in mesoporous silica matrixes," *Nano Letters*, vol. 16, no. 9, pp. 5866–5874, 2016.

[52] S. Grimme, "Semiempirical gga-type density functional constructed with a long-range dispersion correction," *Journal of Computational Chemistry*, vol. 27, no. 15, pp. 1787–1799, 2006.

[53] Q. Wu, S. Zhang, H.-F. Song, M. Troyer, and A. A. Soluyanov, "Wanniertools: An open-source software package for novel topological materials," *Computer Physics Communications*, vol. 224, pp. 405–416, 2018.

[54] C. Grote, B. Ehrlich, and R. F. Berger, "Tuning the near-gap electronic structure of tin-halide and lead-halide perovskites via changes in atomic layering," *Physical Review B*, vol. 90, no. 20, p. 205202, 2014.

[55] K. Gesi, K. Ozawa, and S. Hirotsu, "Effect of hydrostatic pressure on the structural phase transitions in $CsPbCl_3$ and $CsPbBr_3$," *Journal of the Physical Society of Japan*, vol. 38, no. 2, pp. 463–466, 1975.

[56] Q. Wu, S. Zhang, H.-F. Song, M. Troyer, and A. A. Soluyanov, "Wanniertools: An open-source software package for novel topological materials," *Computer Physics Communications*, vol. 224, pp. 405–416, 2018.

Chapter 7

# Insights from DFT into delayed emission in Mn-doped perovskite nanocrystals

## 7.1 Introduction

Light emitting devices (LEDs) are characterized by their high energy efficiency, color quality and low energetic costs of manufacturing. An important goal is to reduce energy losses. These losses mostly arise from non-radiative recombination process. These include Auger recombination[1] and processes due to surface defects.[2;3] In these processes, charge carriers recombine, releasing phonons instead of photons. The goal is to reduce energy losses through non-radiative recombination and increase radiative recombination where the charge carriers recombine releasing photons. The ratio of the radiative recombination rate to the non-radiative recombination rate is known as the quantum yield. So, in other words, to reduce energy losses in light emitting devices, higher quantum yield is desirable. Inorganic perovskite nanocrystals show several fold improvement in the quantum yield[4;5] as compared to other systems.

A slow supply of excited state electrons to radiative excited states of the host systems could significantly increase the quantum yield. This involves quick extraction of the photo-excited electrons into long-lived impurity levels, slow back-transfer through finite vibrational coupling of the impurity levels with the host, followed by radiative recombination of the electrons.

Though the importance of spin in opto-electronics is well known, it was generally considered a loss pathway until harvesting of the spin selective losses was achieved in organic molecules by the thermally assisted delayed fluorescence (TADF), after it was first introduced by Adaichi *et al.*[6] Despite extensive use of TADF in organic molecules since then, similar work has not been attempted in inorganic systems. This could be due to the additional challenge of introducing a spin selective loss-pathway that is faster than other non-radiative losses, while in organic molecules the spin selective losses form the major component of the loss pathway.

Deliberate rerouting of the photo-excited electrons to the spin-forbidden state would require a fast electron transfer to the impurity levels followed by slow rerouting of these electrons back to the host for band-edge recombination. Mn doping in nanocrystals is known for its fast extraction of the photo-excited electrons[7–9] to a spin-forbidden state, leading to a long emission lifetime. If we can now deliberately detrap the electrons from Mn and return to the radiative excited state of the host within the fluorescence lifetime of Mn, our aim of Vibrationally Assisted Delayed Fluorosence (VADF) would be achieved. This targeted internal hopping of electrons, as well as the internal electron storeroom, is not only of fundamental importance towards our understanding of Mn emission but also offers a powerful strategy to increase the efficiency of optoelectronic devices by reducing non-radiative decay losses.

## 7.2 Experimental Results

Our experimental collaborators in the group of Prof. Ranjani Viswanatha have recently synthesized Mn-doped $CsPbBr_{3-x}Cl_x$ nanocrystals for different concentrations of Cl. This results in delayed excitonic fluorescence and increased photoluminescence quantum yield (PLQY).

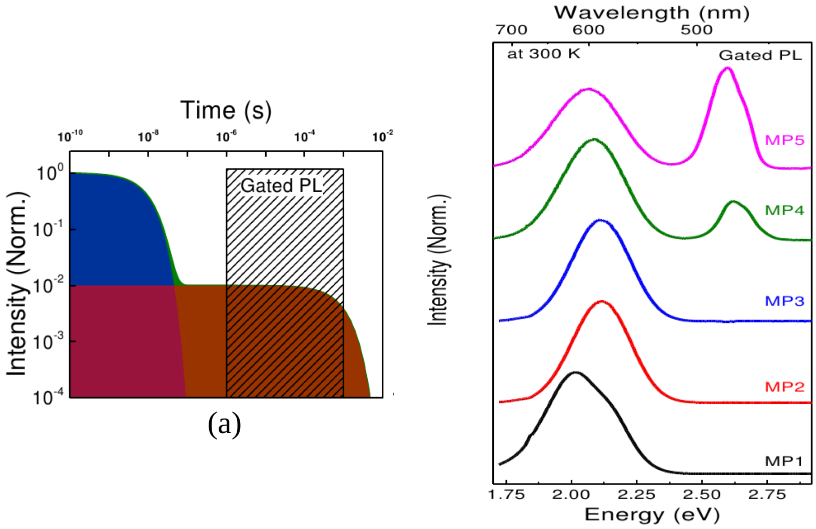

(a)

(b)

Figure 7.1: Experimental results (from our collaborators in the group of Prof. Ranjani Viswanatha) (a) Schematic diagram of gated PL (b) Room temperature gated PL emission for different Mn doped $CsPbBr_{3-3x}Cl_x$ nanocrystal samples denoted by MP1 to MP5

Fig. 7.1(a) shows the schematic diagram of gated photoluminescence (PL). The timescale of gated PL is mentioned in the diagram where the excitonic luminescence is obtained after a delay of 150 microsecond. Fig. 7.1(b) shows the gated emission spectra for different Mn-doped $CsPbBr_{3-3x}Cl_x$ nanocrystals samples denoted by MP1 to MP5. The Br concentrations of MP1, MP2, MP3, MP4 and MP5 are 0%, 20%, 40%, 60% and 80% respectively. Fig. 7.1(b) shows that irrespective of band gap, all the samples show Mn emission in gated PL. Apart from that, from Fig. 7.1(b) we can see that for Br-rich samples like MP5, there is substantial excitonic emission along with the Mn emission. This is due to the electron detrapping from $Mn^{2+}$ to the host conduction band. The undoped counterpart of the MP5 sample shows a PLQY of 30%. However with inclusion of Mn, the PLQY is more than 50%.

Motivated by the above experimental observation, we have performed *ab initio* density functional theory (DFT),[10;11] and *ab initio* density functional perturbation theory (DFPT) calculations to understand the mechanism of delayed emission in Mn-doped perovskite halide nanocrystals, as well as to understand the reason behind the electron detrapping from $Mn^{2+}$ to the host conduction band.

## 7.3 Systems under study

X-ray diffraction (XRD) and transmission electron microscopy (TEM) results show that the Mn-doped perovskite nanocrystals are highly crystalline and retain the cubic structure of parent undoped counterpart. Also optical emission spectroscopy ICP-OES shows experimentally that the doping concentration of Mn in the Mn-doped halide perovskites is less than 5%.

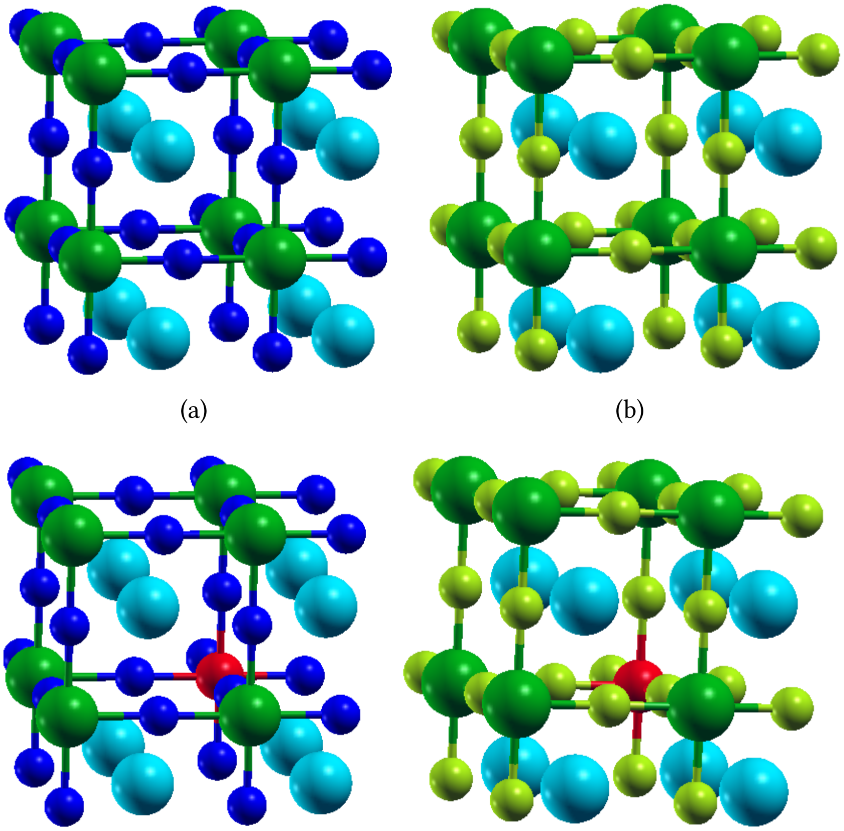
(a) (b)

(c) (d)

Figure 7.2: Structure of cubic (a) $CsPbBr_3$ (b) $CsPbCl_3$ (c) Mn-doped $CsPbBr_3$ (d) Mn-doped $CsPbCl_3$. Doping concentration of Mn is 12.5% in (c) and (d) Color scheme for atomic spheres: Cs (sky blue), Pb (green) Br (blue) Cl (light green).

To understand the electronic structure of the pure halides, we have performed theoretical calculations for cubic $CsPbBr_3$ and $CsPbCl_3$. The primitive unit cells for $CsPbBr_3$ (see Fig. 7.2(a)) and $CsPbCl_3$ (see Fig. 7.2(b)) consist of 1 Cs, 1 Pb and 3 Br/Cl atoms. For the Mn doping we have considered 2×2×2 supercells of $CsPbBr_3$ and $CsPbCl_3$, in which we replace one of the Pb atoms by Mn (see Fig. 7.2(c) and Fig. 7.2(d)). This corresponds to a 12.5% doping concentration. Although experimentally the doping concentrations is less than 5%, due to the computational limitation of having to work with a reasonably small supercell, we have considered 12.5% doping concentration in our calculations.

## 7.4 Computational Details

Our calculations have been performed using *ab initio* density functional theory (DFT),[10;11] as implemented in the Quantum ESPRESSO package.[12] To describe the exchange-correlation interactions a generalized gradient approximation of the PBE form was used.[13] Electronic wavefunctions were expanded using a plane wave basis set, with cutoffs of 40 Ry and 400 Ry for the wavefunctions and charge density, respectively. The interactions between the ionic cores and valence electrons were described using ultrasoft pseudopotentials.[14] Structural optimizations were performed using the Broyden-Fletcher-Goldfarb-Shanno (BFGS) scheme until the Hellmann-Feynman forces on all the atoms being relaxed were less than 0.001 Ry/bohr.[15–18] The Brillouin zone was sampled with a Monkhorst-Pack[19] mesh of 8×8×8 k-points for the primitive unit cell of $CsPbBr_3$ and $CsPbCl_3$; scaled appropriately for supercells. Phonon calculations have been performed using density functional perturbation theory (DFPT).[20] Spin-orbit effects have been incorporated using fully relativistic pseudopotentials.[21]

## 7.5 Results and Discussion

### 7.5.1 Lattice parameter and electronic structure of $CsPbBr_3$ and $CsPbCl_3$

We find the lattice constant of $CsPbBr_3$ to be 6.01 Å, which is in excellent agreement with a previous theoretical value of 6.00 Å [22]. It is however somewhat larger than our experimental value of 5.85 Å for the $CsPbBr_3$ nanocrystal and an earlier experimental value of 5.874 Å [23] for bulk $CsPbBr_3$. The calculated lattice constant of $CsPbCl_3$ is 5.74 Å, which

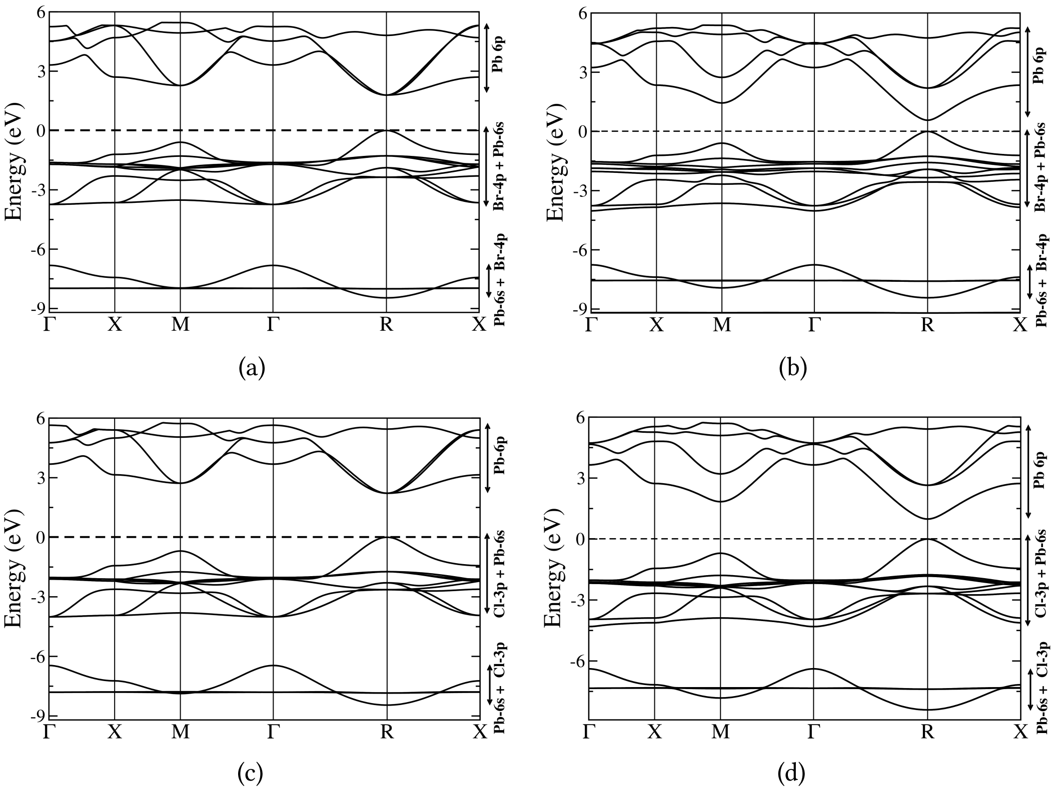

(a)

(b)

(c)

(d)

Figure 7.3: DFT results for electronic band structure of the undoped halide perovskites. $CsPbBr_3$ (a) without and (b) with spin-orbit coupling. The conduction band has Pb 6p character and the valence band arises from Br 4p and Pb 6s orbitals. Band structure of $CsPbCl_3$ (c) without and (d) with spin-orbit coupling. The conduction band has Pb 6p character and the valence band arises from Cl 3p and Pb 6s orbitals.

is in excellent agreement with a previous theoretical value of of 5.73 Å [22]. It is however somewhat larger than our experimental value of 5.62 Å for the $CsPbCl_3$ nanocrystal and an earlier experimental value of 5.61 Å [23] for bulk $CsPbCl_3$. The discrepancy is presumably due to the use of the GGA in our calculations, which is known to underbind.

The band structure of $CsPbBr_3$ without spin-orbit coupling is shown in Fig. 7.3(a). The valence band and the band below this arise mainly from antibonding and bonding, respectively, between Br 4p and Pb 6s orbitals. The conduction band has primarily Pb 6p character. The calculated band gap of $CsPbBr_3$ is 1.79 eV. This can be compared with a previous DFT value of 1.79 eV, [22] an earlier experimental value of 2.36 eV [24] for bulk $CsPbBr_3$ and our experimental result of 2.42 eV for the $CsPbBr_3$ nanocrystal. We note that the underestimation of the band gap is a well-known shortcoming of standard DFT calculations. The band structure of $CsPbBr_3$ with spin-orbit coupling is shown in Fig. 7.3(b). As the valence band arises from Br 4p and Pb 6s states, it is not significantly affected by spin-orbit coupling. However, the conduction band arises from Pb 6p states; Pb 6p orbitals have a significant spin-orbit effect, splitting into $J_{3/2}$ and $J_{1/2}$ levels, and the conduction band edge is thus shifted. As a result the band gap is lessened to 0.567 eV (at GGA level, which is again an underestimation).

The band structure of $CsPbCl_3$ without spin-orbit coupling is shown in Fig. 7.3(c). Similar to $CsPbBr_3$, for $CsPbCl_3$ the valence band and the band below this arise mainly from antibonding and bonding, respectively, between Cl 3p and Pb 6s orbitals and the conduction band has primarily Pb 6p character. The calculated band gap (without spin-orbit coupling) of $CsPbCl_3$ is 2.22 eV. This can be compared with a previous DFT value of 2.21 eV [22], an earlier experimental value of 2.36 eV [24] for bulk $CsPbCl_3$ and our experimental result of 3.0 eV for the $CsPbCl_3$ nanocrystal. The band structure of $CsPbBr_3$ with spin-orbit coupling is shown in Fig. 7.3(d). With the inclusion of spin-orbit coupling, the band gap becomes 0.985 eV

In both $CsPbBr_3$ and $CsPbCl_3$, the band gap is direct at the R point.

### 7.5.2 Electronic structure of Mn-doped $CsPbBr_3$

Next, we have considered the effects of Mn doping in cubic $CsPbBr_3$. Experimentally, the concentration of Mn is less than 5%. Due to computational limitations, theoretically we have however considered one Mn atom substituted in a 2×2×2 unit cell of $CsPbBr_3$, which corresponds to a 12.5% doping concentration. Upon Mn doping, the band gap change is very small, when compared to the undoped material, in agreement with experimental results.

The non-relativistic projected band structure of Mn-doped $CsPbBr_3$ is shown in Fig. 7.4. The bands are colored according to their orbital character, based upon a projection onto atomic wavefunctions. Red, green and blue colors represent Mn 3d, Pb 6p and Br 4p like

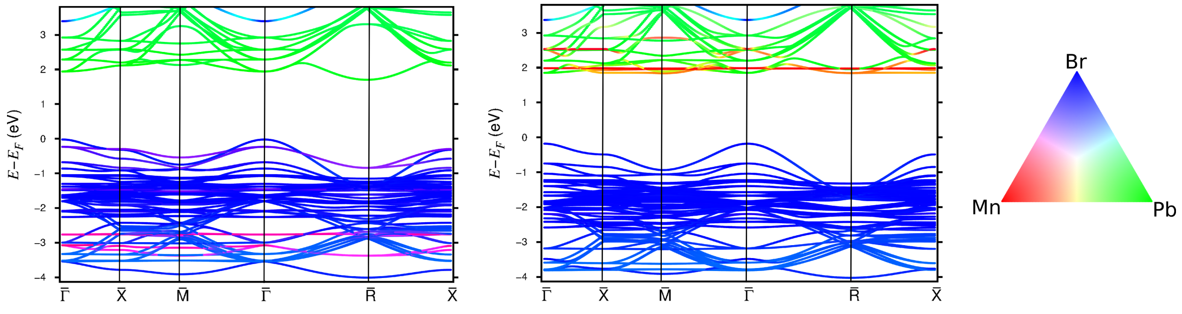

(a) (b)

Figure 7.4: Projected band structure of (a) spin up and (b) spin down states of 12.5% Mn-doped $CsPbBr_3$. The contributions from Mn 3d, Pb 6p and Br 4p are represented by red, green and blue colors respectively. The intermediate colors shown by the color triangle denotes the amount of overlap between the orbitals. Note that Mn hybridizes with the valence band in the spin up states and with the conduction band in the spin down states.

character, respectively, with intermediate colors indicating the degree of hybridization between these three states. For Mn-doped $CsPbBr_3$, in the spin up states Mn hybridizes with the valence band, whereas for the spin down states, Mn hybridizes with only the conduction bands, i.e., with Pb.

### 7.5.3 Shift in the position of Mn level in the conduction band upon inclusion of spin-orbit coupling

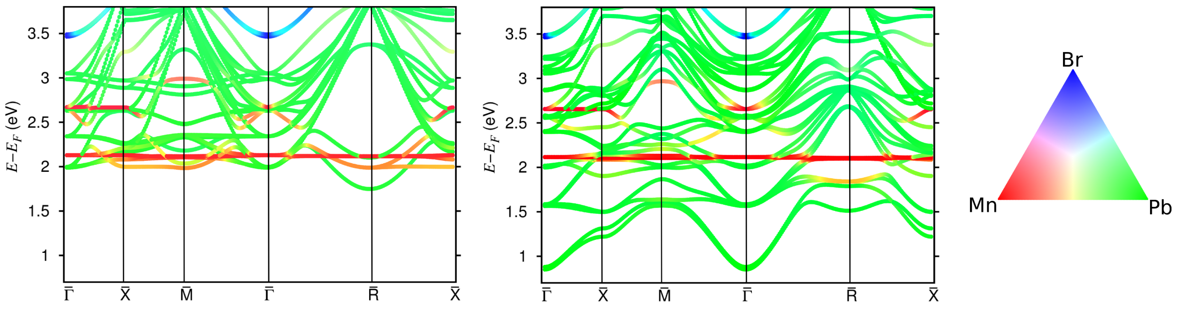

(a) (b)

Figure 7.5: Projected band structure of the conduction band for Mn doped $CsPbBr_3$ showing the contributions from Mn 3d, Pb 6p and Br 4p orbitals (a) without and (b) with spin-orbit coupling. The contributions from Mn 3d, Pb 6p and Br 4p are represented by red, green and blue colors respectively. The intermediate colors shown by the color triangle denotes the amount of overlap between the orbitals

The orbital-projected conduction bands of Mn-doped $CsPbBr_3$ without and with spin-orbit interactions are shown in Fig. 7.5(a) and Fig. 7.5(b), respectively. A similar color code is used as in Fig. 7.4. From these results, it is evident that in the absence of SOC, the Mn levels lie at the edge of the conduction band. However, in the presence of SOC, because of strong relativistic effects in the heavy Pb atoms, the bottom of the conduction band is now pulled considerably lower in energy, and as a result the Mn levels end up being buried deep within the conduction band. We note also that there are signatures of significant electronic coupling (hybridization) between Mn 3d and Pb 6p states, especially in the vicinity of the R point in the Brillouin zone. Below we will also see that there is vibrational coupling between Mn and host atoms (Pb/Br) and electron-phonon coupling between Mn atoms and host electrons (Pb/Br), thus providing, in addition, a phonon-assisted pathway for electrons in the Mn 3d states to reach the conduction band minimum. This targeted internal hopping of electrons, as well as the internal electron storeroom, is not only of fundamental importance towards our understanding of Mn emission but could become an important part of energy-based applications by reducing non-radiative decay losses.

### 7.5.4 Comparison of vibrational coupling between Mn-doped $CsPbBr_3$ and Mn doped $CsPbCl_3$

To understand the mechanism of electron detrapping from $Mn^{2+}$ to the host conduction band, we first look at the vibrational coupling between Mn atoms and the host atoms, i.e., Pb and Br in Mn-doped $CsPbBr_3$ and Pb and Cl in Mn-doped $CsPbCl_3$. The transfer of electrons is favorable if there is a significant amount of vibrational coupling between Mn atoms and host atoms. Further, for these modes if we see a significant amount of electron-phonon coupling, this can support the existence of electron detrapping from $Mn^{2+}$ states to the host conduction band through phonon-assisted pathways.

Accordingly, we have calculated the projected phonon dispersion using density functional perturbation theory (DFPT). The projected phonon dispersion plots for (a) Mn-doped $CsPbBr_3$ and (b) Mn-doped $CsPbCl_3$ are shown in Fig. 7.6(a) and Fig. 7.6(b). The phonon

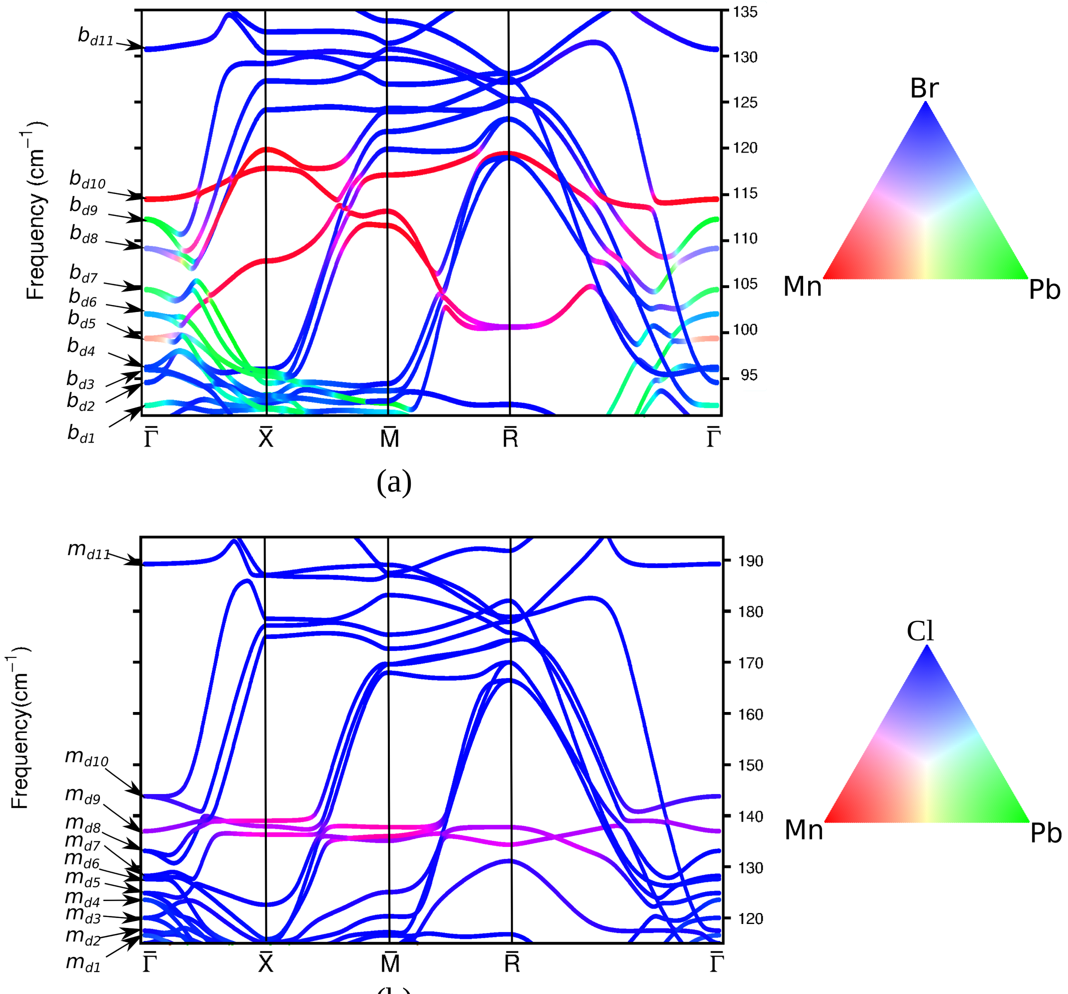

(a)

(b)

Figure 7.6: Projected phonon spectrum, as calculated from DFPT, for (a) Mn-doped $CsPbBr_3$ and (b) Mn-doped $CsPbCl_3$. The branches are colored according to their weights on the different atoms in the unit cell, as shown in the RGB color triangle.

branches are colored according to their weights on Mn (red), Pb (green) and Br/Cl (blue), with intermediate colors indicating the extent of vibrational coupling between atoms of different species.

In Fig. 7.6(a), we can see that there is a significant amount of vibrational coupling between Mn-Pb and Mn-Br for Mn-doped $CsPbBr_3$. We will focus on the vibrational coupling at the zone center, since the coupling is maximum here. The phonon modes at $\Gamma$ for Mn-doped $CsPbBr_3$ are labeled by $b_{d1} - b_{d11}$. The $b_{d10}$ mode is found to be a purely Mn mode, whereas for modes $b_{d5}$, $b_{d6}$ and $b_{d8}$, there is a significant amount of vibrational coupling between Mn and Pb/Br.

In Fig. 7.6(b), we can see that vibrational coupling between Mn-Pb and Mn-Cl for Mn-doped $CsPbCl_3$ is significantly less than for Mn-doped $CsPbBr_3$. The phonon modes at Γ for Mn-doped $CsPbCl_3$ are labeled by $m_{d1}-m_{d11}$. The equivalent of the $b_{d10}$ mode of Mn-doped $CsPbBr_3$ (see Fig. 7.6(b)) is the $m_{d9}$ mode of Mn-doped $CsPbCl_3$ (see Fig. 7.6(a)). However, for $b_{d10}$ the mode consists of pure Mn whereas for $m_{d9}$ there is coupling between Mn and Cl. For $m_{d10}$ modes also there is coupling between Mn and Cl. All other modes at the Γ point are mainly from Cl.

So, the vibrational coupling between Mn and host atoms (i.e., Pb and Br) in Mn-doped $CsPbBr_3$ is significantly larger than that between Mn and host atoms (i.e., Pb and Cl) in Mn-doped $CsPbCl_3$. In the next section we will see how the vibrational coupling will affect the electron-phonon coupling for Mn doped $CsPbBr_3$ for a mode where there is a significant amount of vibrational coupling between Mn and the host.

### 7.5.5 Electron-phonon coupling in Mn-doped $CsPbBr_3$

In the previous section, we have seen that for Mn-doped $CsPbBr_3$, there is a significant amount of vibrational coupling between Mn, Pb and Br for modes $b_{d5}$, $b_{d6}$, $b_{d7}$ and $b_{d8}$, whereas for Mn-doped $CsPbCl_3$, the analogous coupling is negligible. Electron detrapping from Mn states to the host conduction band can be realized by electron-phonon coupling. In order to investigate the electron-phonon coupling, we can examine how the electronic properties of the system change when the crystal vibrates in one of these modes.

In Fig. 7.7(a) and Fig. 7.7(b) we have shown the eigenvectors corresponding to the two degenerate modes $b_{d5}(1)$ and $b_{d5}(2)$ for Mn-doped $CsPbBr_3$. Using the frozen phonon method, we have plotted the electronic band structure for the equilibrium structure and a structure where the atoms are displaced according to $u^{\nu} = \sqrt{\sum_I \frac{1}{M_I} \mathbf{X}_I^{\nu 2}}$ with a maximum displacement of 0.06 Å for Mn-doped $CsPbBr_3$ in Fig. 7.7(c) and Fig. 7.7(d). From the figure we can see that there is an appreciable shift in the electronic eigenvalues (compare the solid green curves with the dashed red curves), indicating that there is significant

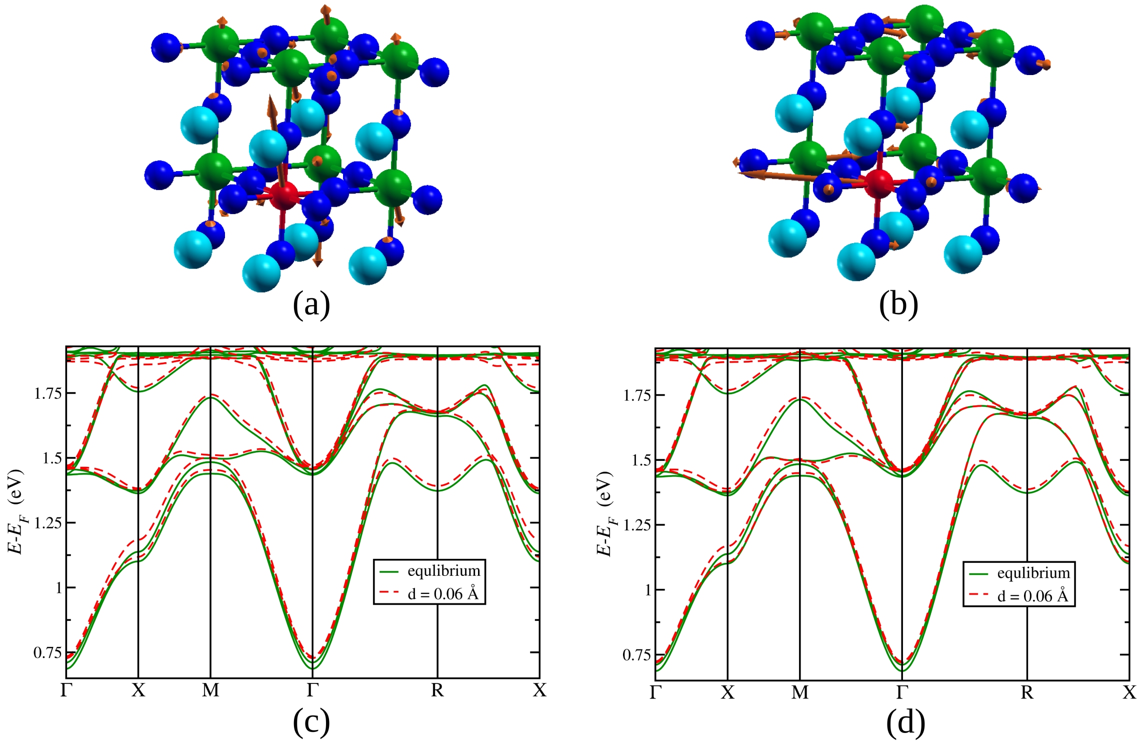

Figure 7.7: (a),(b) Eigenvectors corresponding to the two degenerate phonon modes $b_{d5}(1)$ and $b_{d5}(2)$ of Mn-doped $CsPbBr_3$. (c),(d) The presence of electron-phonon coupling is evidenced from the shift in the electronic bands under atomic displacement corresponding to the two modes Mn-doped $CsPbBr_3$. Green solid lines: equilibrium band structure. Red dotted lines: band structure of the structure after distorted along the mode vector with an atomic displacement of 0.06 ÅĊolor scheme for atomic spheres: Cs (sky blue), Pb (green) Br (blue) Mn (red).

electron-phonon coupling for these modes. The coupling seems to be especially strong for electrons in the vicinity of the X point in the Brillouin zone.

Further work needs to be done to quantify the strength of the electron-phonon coupling; work in this direction is ongoing.

## 7.6 Conclusions

In this chapter, we have used density functional theory and density functional perturbation theory to investigate the reason for delayed photoluminescence and increased quantum yield in Mn doped perovskite nanocrystals.

We first show how the band gap of cubic $CsPbBr_3$ and cubic $CsPbCl_3$ get modified upon incorporation of Mn. First, without incorporating spin-orbit coupling, we have found that spin up and spin down Nb states hybridize with the valence and conduction bands, respectively, of the host. We have also found that upon the incorporation of spin-orbit coupling, the Mn levels get buried deep inside the conduction band.

Upon calculating the phonon spectrum of Mn-doped $CsPbBr_3$ and $CsPbCl_3$, we find that while there is a significant amount of vibrational coupling between Mn and host atoms (Pb/Br) in Mn-doped $CsPbBr_3$ for some modes, the same is not true for Mn-doped $CsPbCl_3$. We also have found indications of a strong electron-phonon coupling in Mn-doped $CsPbBr_3$.

We believe that our results show pathways for detrapping electrons from Mn states to the host conduction states, resulting in delayed photoluminescence.

# Bibliography

[1] A. Chernenko, P. Dorozhkin, V. Kulakovskii, A. Brichkin, S. Ivanov, and A. Toropov, "Auger recombination of excitons in semimagnetic quantum dot structure in a magnetic field," *Physical Review B*, vol. 72, no. 4, p. 045302, 2005.

[2] M. M. Krause, J. Mooney, and P. Kambhampati, "Chemical and thermodynamic control of the surface of semiconductor nanocrystals for designer white light emitters," *ACS nano*, vol. 7, no. 7, pp. 5922–5929, 2013.

[3] V. Pinchetti, A. Anand, Q. A. Akkerman, D. Sciacca, M. Lorenzon, F. Meinardi, M. Fanciulli, L. Manna, and S. Brovelli, "Trap-mediated two-step sensitization of manganese dopants in perovskite nanocrystals," *ACS Energy Letters*, vol. 4, no. 1, pp. 85–93, 2018.

[4] J. Li, L. Xu, T. Wang, J. Song, J. Chen, J. Xue, Y. Dong, B. Cai, Q. Shan, B. Han, *et al.*, "50-Fold EQE improvement up to 6.27% of solution-processed all-inorganic

perovskite $CsPbBr_3$ QLEDs via surface ligand density control," *Advanced Materials*, vol. 29, no. 5, p. 1603885, 2017.

[5] Z.-K. Tan, R. S. Moghaddam, M. L. Lai, P. Docampo, R. Higler, F. Deschler, M. Price, A. Sadhanala, L. M. Pazos, D. Credgington, *et al.*, "Bright light-emitting diodes based on organometal halide perovskite," *Nature nanotechnology*, vol. 9, no. 9, p. 687, 2014.

[6] H. Uoyama, K. Goushi, K. Shizu, H. Nomura, and C. Adachi, "Highly efficient organic light-emitting diodes from delayed fluorescence," *Nature*, vol. 492, no. 7428, p. 234, 2012.

[7] K. Gahlot, A. Camellini, G. Sirigu, G. Cerullo, M. Zavelani-Rossi, A. Singh, U. V. Waghmare, and R. Viswanatha, "Transient species mediating energy transfer to spin-forbidden Mn d states in II–VI semiconductor quantum dots," *ACS Energy Letters*, vol. 4, no. 3, pp. 729–735, 2019.

[8] H.-Y. Chen, S. Maiti, and D. H. Son, "Doping location-dependent energy transfer dynamics in Mn-doped CdS/ZnS nanocrystals," *Acs Nano*, vol. 6, no. 1, pp. 583–591, 2012.

[9] D. Parobek, B. J. Roman, Y. Dong, H. Jin, E. Lee, M. Sheldon, and D. H. Son, "Exciton-to-dopant energy transfer in mn-doped cesium lead halide perovskite nanocrystals," *Nano letters*, vol. 16, no. 12, pp. 7376–7380, 2016.

[10] W. Kohn and L. J. Sham, "Self-consistent equations including exchange and correlation effects," *Physical review*, vol. 140, no. 4A, p. A1133, 1965.

[11] P. Hohenberg and W. Kohn, "Inhomogeneous electron gas," *Physical review*, vol. 136, no. 3B, p. B864, 1964.

[12] P. Giannozzi, S. Baroni, N. Bonini, M. Calandra, R. Car, C. Cavazzoni, D. Ceresoli, G. L. Chiarotti, M. Cococcioni, I. Dabo, *et al.*, "Quantum espresso: a modular and

open-source software project for quantum simulations of materials," *Journal of physics: Condensed matter*, vol. 21, no. 39, p. 395502, 2009.

[13] J. P. Perdew, S. Kurth, A. Zupan, and P. Blaha, "Accurate density functional with correct formal properties: A step beyond the generalized gradient approximation," *Physical review letters*, vol. 82, no. 12, p. 2544, 1999.

[14] D. Vanderbilt, "Soft self-consistent pseudopotentials in a generalized eigenvalue formalism," *Physical review B*, vol. 41, no. 11, p. 7892, 1990.

[15] C. G. Broyden, J. Dennis Jr, and J. J. Moré, "On the local and superlinear convergence of quasi-newton methods," *IMA Journal of Applied Mathematics*, vol. 12, no. 3, pp. 223–245, 1973.

[16] R. Fletcher, "A new approach to variable metric algorithms," *The computer journal*, vol. 13, no. 3, pp. 317–322, 1970.

[17] D. Goldfarb, "A family of variable-metric methods derived by variational means," *Mathematics of computation*, vol. 24, no. 109, pp. 23–26, 1970.

[18] D. F. Shanno, "Conditioning of quasi-newton methods for function minimization," *Mathematics of computation*, vol. 24, no. 111, pp. 647–656, 1970.

[19] H. J. Monkhorst and J. D. Pack, "Special points for brillouin-zone integrations," *Physical review B*, vol. 13, no. 12, p. 5188, 1976.

[20] S. Baroni, S. De Gironcoli, A. Dal Corso, and P. Giannozzi, "Phonons and related crystal properties from density-functional perturbation theory," *Reviews of Modern Physics*, vol. 73, no. 2, p. 515, 2001.

[21] G. Theurich and N. A. Hill, "Self-consistent treatment of spin-orbit coupling in solids using relativistic fully separable ab initio pseudopotentials," *Physical Review B*, vol. 64, no. 2, p. 073106, 2001.

[22] C. Grote, B. Ehrlich, and R. F. Berger, “Tuning the near-gap electronic structure of tin-halide and lead-halide perovskites via changes in atomic layering,” *Physical Review B*, vol. 90, no. 20, p. 205202, 2014.

[23] G. S. Rohrer, *Structure and bonding in crystalline materials.* Cambridge University Press, 2001.

[24] K. Gesi, K. Ozawa, and S. Hirotsu, “Effect of hydrostatic pressure on the structural phase transitions in $CsPbCl_3$ and $CsPbBr_3$,” *Journal of the Physical Society of Japan*, vol. 38, no. 2, pp. 463–466, 1975.

Chapter 8

# Conclusions and Outlook

In this chapter, I summarize the main results obtained in this thesis, and also mention any open questions or possible directions for future work.

All the work in this thesis was performed using density functional theory (DFT), in some cases supplemented with density functional perturbation theory (DFPT) and *ab initio* molecular dynamics (AIMD). In most cases, van der Waals interactions were incorporated using the DFT-D2 scheme.

In Chapter 3, we studied the adsorption of the polar methanol molecule on various mixed C-BN systems: striped systems with either armchair or zigzag interfaces between graphene and h-BN domains, an intermixed BCN structure, and a triangular graphene island embedded within a BN matrix. We also compared this with methanol adsorption on the pristine graphene and h-BN substrates.

Before studying adsorption of methanol, we first studied the stability of different substrate configurations. We found that structures containing phase segregated domains of graphene and BN are energetically preferred over intermixed structures. Though striped domains are the most favored, structures with triangular graphene islands embedded in a BN matrix are only slightly less favored, and thus are likely to be found in experiment.

Most interestingly, we find that the adsorption energy of methanol increases significantly on systems containing zigzag interfaces between graphene and BN. This is because lines of charge form at these interfaces, due to the polar discontinuity at such interfaces.

The adsorption energy is greatest at vertices of triangular islands, where two zigzag C-B interfaces meet. If it is possible to deliberately engineer nanostructures that have this configuration, this should significantly increase the binding of methanol on these substrates, which can have interesting applications for thermal energy storage.

From a theoretical point of view, it is not yet completely clear how to treat the graphene-BN interface. Though the theory of polar discontinuities is well-developed, this is true only for the case of a polar discontinuity between two insulators. Graphene is a peculiar case in that it is a semi-metal, with zero band gap but zero density of states at the Fermi level. It is not clear whether the formulae and formalism developed for insulators is applicable for this case, and greater clarity is desirable in this context.

In Chapter 4, we studied the energetics, structure and dynamics of water on graphene and graphene oxide, using density functional theory and Car-Parrinello molecular dynamics.

We found that the strength of binding of water molecules is greatly enhanced on densely functionalized regions of graphene oxide, which are hydrophilic, in contrast to the hydrophobic regions of bare graphene.

When water is deposited on graphene oxide, it initially wets the hydrophilic functionalized regions, and subsequently these regions are connected by the formation of water bridges that cross hydrophobic regions of the graphene oxide substrate. As the coverage of water increases, there is a layering of the water molecules, and the difference in the structure of the water over the hydrophobic and hydrophilic domains becomes less and less marked.

As the coverage of water is increased, both the average coordination of water molecules and the mean number of hydrogen bonds connecting water molecules increases. Also, the diffusion constant of water molecules increases, and the hydrogen bond relaxation time decreases. All of this is interesting because these are factors that will impact proton conductivity.

We have attempted to directly study the process of proton conductivity in water on graphene oxide, however these studies are at too preliminary a stage to be included in this thesis. It would be interesting to continue this work along those lines, as well as to induce a flow in the water molecules, so as to more directly study the rheology of water molecules on graphene oxide; to the best of our knowledge, such studies have so far been carried out only using classical potentials, and it would be interesting to explore whether the incorporation of quantum mechanical effects leads to any differences in results.

In Chapter 5, we studied hydrogen adsorption on molybdenum carbide, nitride and carbide-nitride composite systems, with a view to studying the HER activity of these systems.

We obtained the somewhat unexpected result that incorporating van der Waals interactions is essential to correctly reproduce the ground state structures of bulk $Mo_2C$ and $Mo_2N$.

By computing the Gibbs free energy, which is believed to be a good descriptor for HER activity, we found that carbide-nitride composite structures should show better HER activity than pure carbide and nitride structures, in agreement with experiment. We have also shown that N-rich composite structures show better HER activity than C rich composite structures.

Other approaches to studying HER activity include calculating reaction barriers, volcano plots, etc. This study has been somewhat limited by the fact that experimental results are yet awaited at zero overpotential. We are hopeful that these results will confirm our other findings.

In Chapter 6, we showed that three factors are crucial to explain why nanocrystals of $CsPbBr_3$ show a blue shift in their emission spectra on Sn doping, whereas the bulk crystals show a red shift. One is that the nanocrystals have a cubic structure. Another is that for the cubic structure, spin-orbit interactions (arising from the Pb states) result in a band inversion if the lattice constant is reduced, as a result of which there is a non-monotonic change of band gap with lattice constant, with red shift in a certain range of lattice constants and a blue shift in another range of lattice constants, on reducing lattice constant. The third factor is that substitutional doping by Sn reduces the lattice constant to a region of the band gap vs. lattice constant curve where, as a result of the band inversion, one obtains a blue shift in the band gap upon reducing the lattice constant by Sn doping. What remains to be done in this context is to study other ranges of Sn doping; at present we are limited, by computational constraints, to study rather large values of Sn doping concentration. It would also be interesting to confirm theoretically that the nanocrystals assume a different structure from the bulk crystals, and hence behave differently from the bulk on Sn-doping; at present, we have made use of the experimentally determined fact that the nanocrystals have the cubic structure, and have not verified it ourselves.

In Chapter 7, we have used density functional theory and density functional perturbation theory to explain the reason for delayed photoluminescence and increased quantum yield in Mn-doped perovskite nanocrystals.

One important result is that we have found that, upon incorporation of spin-orbit coupling, the Mn level gets buried deep inside the conduction band instead of being at the band edge. We have also found that there is a significant amount of vibrational coupling between Mn and host atoms (Pb/Br) in Mn-doped $CsPbBr_3$ for some modes whereas for Mn-doped $CsPbCl_3$ the amount of coupling is negligible. We have also found that there is significant electron-phonon coupling between Mn and the host. These results imply that one can detrap from Mn states to the host conduction states resulting in a delayed photoluminescence. What would be interesting in this context is to study the excited states using some method like time dependent density functional theory. It would also be interesting to get a more accurate computation of the band gap by, e.g., using hybrid functionals. Finally, we would like to quantify the electron-phonon coupling, e.g., using the linear response method, rather than merely get a rough idea of the existence of electron-phonon coupling using the frozen-phonon technique as done at present.

In conclusion, we have studied a wide range of topics in this thesis. In some cases, we have settled puzzles that arose from experimental data, or provided theoretical support to interesting and important experimental observations. In some other cases, our work can be viewed as first attempts to tackle a problem, which may not yet have provided definitive answers, but rather raise intriguing possibilities for future experiments and calculations.